Ab Initio Thermodynamics of Phase-Separating and Cation-Disordered Cathodes for Li-ion Batteries

by
Aziz Abdellahi

B.Ing. Engineering, Ecole Polytechnique (2007)

M. Sc. A. Nuclear Engineering, Ecole Polytechnique de Montreal (2009)

Submitted to the Department of Materials Science and Engineering
in partial fulfillment of the requirements for the degree of

Doctor of Philosophy
in Materials Science and Engineering

at the

MASSACHUSETTS INSTITUTE OF TECHNOLOGY

February 2016

Signature of author ..... Signature redacted
Department of Materials Science and Engineering
November 30, 2015

Certified by ..... Signature redacted .....
Gerbrand Ceder
R. P. Simmons Professor of Materials Science and Engineering
Thesis Supervisor

Accepted by ..... Signature redacted .....
Donald R. Sadoway
Chair, Departmental Committee on Graduate Students

Ab-initio Thermodynamics of Phase-Separating and Cation-Disordered Cathodes for Li-ion batteries

by
Aziz Abdellahi

Submitted to the Department of Materials Science and Engineering
On January 15th 2015, in partial fulfillment of the requirements for the degree of
Doctor of Philosophy in Materials Science and Engineering

Abstract

In order to accelerate the electrification of the automotive fleet, the energy density and power density limitations of commercial Li-ion battery cathodes (layered $LiMO_2$) must be overcome. In this thesis, we use *ab initio* methods to gain critical insights on two important classes of alternative Li-ion battery cathodes, namely high-capacity Li-excess cation-disordered rocksalts and high-rate $LiFePO_4$.

In the first part of this thesis (Chapters 3 and 4), we provide the first voltage-based design rules for high-capacity cation-disordered rocksalts. We demonstrate that, depending on the transition metal species, cation disorder can increase or decrease the average voltage of lithium transition metal oxides, and hence increase or decrease the total energy density of these compounds. In particular, the disordered $Ni^{3+/4+}$ voltage is found to be high (~4.4V), value at which it is likely to be preceded by oxygen activity. We further investigate the effect of cation-disorder on the voltage slope of lithium transition metal oxides, which controls the total capacity accessible below the stability limit of the electrolyte. We demonstrate that cation-disorder increases the voltage slope by increasing the Li site energy distribution and by enabling Li occupation of high-voltage tetrahedral sites. We further demonstrate that the voltage slope increase upon disorder is smaller for high-voltage transition metals, and that short-range ordering and Li-excess contribute in reducing the inaccessible capacity at high voltage upon disorder.

In the second part of this thesis (Chapter 5), we resolve the apparent paradox between the high Li diffusivity in phase-separating $LiFePO_4$ and the persistence of thermodynamically unstable solid-solution states during (dis)charge at low to moderate C-rates. We demonstrate that, even under rate conditions such that relaxation to a two-phase state is kinetically possible, the thermodynamically favorable state in a single particle is not a sharp interface but rather a diffuse interface with an *intermediate solid-solution region* that occupies a significant fraction of the particle volume. Our results not only explain the persistence of solid-solution regions at low to moderate C-rates in nano-$LiFePO_4$, but also explain the observations of stable intermediate solid-solution states at an *ac* interface in particles quenched from a solid solution.

Thesis Supervisor: Gerbrand Ceder
Title: R. P. Simmons Professor of Materials Science and Engineering

Acknowledgements

I would like to acknowledge my advisor, Professor Gerbrand Ceder, for the guidance throughout this doctoral process. Through my interactions with Professor Ceder, I learned to become a professional scientist, to efficiently approach a complex problem with a balance of rigor and practical results. I would like to thank him for the variety of projects that I was assigned to during my PhD tenure. This allowed me to gain a broader view of the field of Li-ion batteries and electrochemistry. I intend to leverage this experience efficiently during my scientific career.

I would like to thank my thesis committee members (Prof Jeffrey Grossman and Prof Michael Demkowicz) for their valuable comments during my PhD. Their guidance was key in strengthening the content of this thesis.

I would like to thank the entire Ceder group, past and present members, for a great research atmosphere (byalphabetical order of first name: Alexander Urban, Alexandra Toumar, Anubhav Jain, Bernardo Orvananos, Bo Xu, Bryn Waldwick, Byoungwoo Kang, Charles Moore, Daniil Kitchaev, Di Wu, Dong Hwa Seo, Edmanuel Torres, Hailong Chen, Geoffroy Hautier, Denis Kramer, Hong Zhu, Ian Matts, Jae Chul Kim, Jinhyuk Lee, Lei Liu, Lei Wang, Lusann Yang, Maria Chan, Nancy Twu, Pieremanuele Canepa, Plousia Vassilaras, Predrac Lazic, Qing Hao, Rahul Malik, Reece Daniel, Rickard Armiento, Robert Doe, Rui Wang, Ruoshi Sun, Sai Gautam Gopalakrishnan, Sai Jayaraman, Sangtae Kim, Ziqin Rong, Shengshuan Zhu, ShinYoung Kang, Shyue Ping Ong, Stephen Dacek, Tim Mueller, Vincent Chevrier, Wenhao Sun, Wenxuan Huang, William Richards, Xiaofei Sun, Xiaohua Ma, Xin Li, Yabi Wu, Yan (Eric) Wang, Yifei Mo, Yuechuan Lei, Yun Liu). It was a pleasure to work alongside you during

these six years, and I learned tremendously from all of you. The Ceder alumni community is a strong network, and I hope to maintain strong relationships with you in the years to come.

I would like to specifically thank two members of the Ceder group without whom the completion of this thesis would not have been possible. Rahul Malik became my mentor from my first day in the Ceder group and, under his guidance, I learned to frame scientific questions, to keep a big picture in a scientific project and to efficiently communicate and present scientific ideas. Rahul has been, throughout my PhD, a great colleague, a good personal friend and a fellow Canadian hockey enthusiast. I would also like to extend my most sincere gratitude to Alex Urban, with whom I directly collaborated on Li-excess related projects. His scientific rigor and unparalleled understanding of Density Functional Theory and electronic structure calculations proved invaluable throughout this thesis.

I thank the Li-excess subgroup (Jinhyuk Lee, Alex Urban, Nancy Twu, Donghwa Seo, Shinyoung Kang, Rahul Malik, Rui Wang, Xin Li, Ian Matts, Stephen Dacek) for a great team spirit and collaborative atmosphere. Special thanks to Jinhyuk for allowing me to shadow him in the lab and to learn a bit of his experimental craft, as well as for numerous late night conversations in the office.

I thank my officemates in 13-5041 (Geoffroy Hautier, Charles Moore, Xiaohua Ma, Alex Toumar, Bryn Waldwick, Stephen Dacek, Daniil Kitchaev, Bernardo Orvananos, Yuechuan Lei) for a great office atmosphere, support and pleasant conversations.

I thank my collaborators at the University of Michigan (Bernardo Orvananos, Hui-Chia Yu, Prof Katsuyo Thornton) and at the Hitit University in Turkey (Prof Oncu Akyildiz) for invaluable contributions on continuum elasticity calculations for $LiFePO_4$ and for taking me in

as a collaborator on studies of $LiFePO_4$ at the electrode level.

I thank the NECCES-EFRC (NorthEast Center for Chemical Energy Storage, a Department ofEnergy Energy Research Frontier Center) for funding and for a great collaborative atmosphere to perform research on $LiFePO_4$ (NECCES-I) as well as layered transition metal oxides (NECCES-II). Collaborations with experimentalists and other computational scientists was an invaluable experience that allowed me to work in a larger context. I especially thank the management team and Principle Investigators of the EFRC for this great opportunity (Prof Stanley Witthingham, Prof Clare Grey, Prof Shirley Meng, Prof Jordi Cabana, Prof Glenn Amatucci, Prof Katsuyo Thornton, Prof Yet Ming Chiang).

I want thank the many organizations, inside and outside of MIT, who contributed to my rich extracurricular life during my tenure at MIT. I thank the MIT Energy Club, both members and management teams, for a great three-year involvement in the activities of the Club. As Energy 101 Chair, Co-Director of the Events Committee and Lectures co-chair, I learned tremendously on energy technology, energy economics, sustainability and climate change. I extend my gratitude to all Energy Club members with whom I worked during those years, and I strongly encourage MIT students to partake in the activities of the Club.

I thank my Taekwondo clubs in Boston and Montreal, specifically coaching staff and athletes, which allowed me to pursue high-level Taekwondo competitions during my PhD. I especially thank the Genesis Academy of Traditional Taekwondo, the MIT Sport Taekwondo Club, the CW Taekwondo club and Eclispe TaeKwondo Laval (Laval, Canada). Thanks to these amazing coaches and athletes, I was able to represent my home country of Canada in three World Championships during my tenure at MIT. I am especially proud of my performance at the

World Cup 2014 in Jamaica, in which I earned a silver medal. Special thanks to my head coaches Sydley Gardner, George Panagiotakopoulos, Daniel Chuang, Fabio Takahashi, Mike Harb, Marie-Claude Messier, Richard Nguyen, Nicolas Tran and Philippe Parent for taking my Taekwondo craft to another level.

I would like to thank my parents for encouraging me throughout this doctoral process. You have always been a source of inspiration for me, and I am very grateful for the opportunities I have had throughout my life thanks to your unconditional love and support. I would also like to send a big hug to my little sister and brother, whom I love more than they could possibly imagine.

I would like to conclude these acknowledgements by thanking my better half, Meghan Allen, for her support and encouragement during this doctoral process. I could not have done it without you.

Table of Contents

List of Figures **11**

Introduction **18**

1.1 Motivation 18

1.2 Overview of Li-ion batteries 19

1.3 Layered lithium transition metal oxides 22

1.4 Li-excess cation-disordered rocksalts 24

1.5 Surface cation disorder in layered oxides 29

1.6 High power $LiFePO_4$ olivine 31

1.7 Overview of the thesis 36

Chapter 2: First Principles Methods **38**

2.1 Density Functional Theory 38

2.2 Cluster Expansions 43

2.3 Statistical Mechanics via Monte Carlo 48

2.4 Special Quasi-Random Structures (SQS) 51

2.5 Thermodynamics of phase-separating systems 53

Chapter 3: The effect of cation disorder on the average Li intercalation voltage of transition metal oxides **62**

3.1 Introduction 62

3.2 Methodology 64

3.3 Results 68

3.4 Discussion 74

3.5 Conclusion 80

Chapter 4: The effect of cation disorder on the voltage profile of Li transition metal oxides 81

4.1 Introduction 81

4.2 Model 83

4.3 Results 93

4.3.1 Octahedral Li occupancy 93

4.3.2 Tetrahedral Li occupancy 98

4.3.3 Effect of short-range order 99

4.3.4 Effect of Li-excess on tetrahedral capacity 101

4.4 Summary and Discussion 106

4.5 Conclusion 106

4.6 Appendix 110

4.6.1 Pair term approximation for ΔE_{site} 110

4.6.2 Determining ΔV^{tet} from the spinel structure 112

Chapter 5: Thermodynamic Stability of Intermediate Solid Solution States in $LiFePO_4$ nano-particles 115

5.1 Introduction 115

5.2 Methodology 118

5.3 Results 123

5.4 Discussion 136

5.5 Conclusion 141

Conclusions 142

References 145

List of Figures

Figure 1-1 Schematic of a Li-ion battery operating (a) during discharge and (b) during charge 19

Figure 1-2 First cycle voltage profile of $LiCoO_2$ at a rate of 0.1C (charge discharge in 10 hours) 21

Figure 1-3 Ordered and disordered structures on the $LiMO_2$ rocksalt lattice **(a)** In the layered st ructure, Li and M occupy alternate (111) layers of the FCC cation sublattice **(b)** In a fully catio n disordered rocksalt, cations randomly occupy sites of the FCC cation sublattice **(c)** In both or dered and disordered compounds, Li and M are octahedrally coordinated by oxygen. 23

Figure 1-4 Different levels of cation disorder in $LiMO_2$ compounds **(a)** Fully ordered (e.g. laye red) $LiMO_2$ compound (the layers being the (111) planes of the FCC cation sublattice) **(b)** Parti ally disordered compound **(c)** Fully disordered rocksalt. The view is shown along the (111) pla nes of the FCC cation sublattice. 25

Figure 1-5 Li diffusion in transition metal oxides **(a)** Li migration between octahedral sites oc curs via an activated tetrahedral site. In stoichiometric layered $LiMO_2$, all activated tetrahedral sites have one face sharing transition metal neighbor (1 TM diffusion channel). In cation disord ered rocksalts or in Li excess compounds, some activated tetrahedral sites have no transition m etal neighbors (0 TM channel) **(b)** Activation barriers for 1 TM and 0 TM channels. Only the 0 TM is active upon disorder **(c)** Percolation treshold for the 0 TM diffusion channel as a functio n of the level of disorder and the Li excess level **(d)** Amount of Li available along the percolati on 0 TM pathway, as a function of the degree of disorder and the Li-excess level..... 26

Figure 1-6 (a) Cation disorder creates a spread of local environment around Li sites **(b)** Cation disorder is expected to increase the voltage slope of Li transition metal oxides (blue and red arr ows) as well as to modify their average Li intercalation voltage (blue and red dots) 29

Figure 1-7 Formation of disordered surface layers triggered by oxygen loss (illustrated for $Li_{1.2}M_{0.8}O_2$ compound). 30

Figure 1-8 (a) Crystal structure of $LiFePO_4$ **(b)** Li diffusion is dominated by 1D diffusion alon g the crystallographic b direction (010)[33] 32

Figure 1-9 (a) High rate performance of $LiFePO_4$ **(b)** Particle nanosizing is required to reach h igh performances (~50-100 nm) 33

Figure 1-10 After initiating lithiation via a non equilibrium solid solution, $LiFePO_4$ particles a re expected to rapidly phase separate **(a)** Lithiation initiates via the non equilibrium solid soluti on pathway **(b)** Past the spinodal point, states of uniform concentration are unstable with respe ct to small fluctuations in concentration **(c)** The expected final state consists in a two phase coe xistence within the particle 35

Figure 2-1 (a) Bulk free energy in an Li_xFePO_4 single particle **(b)** Multi particle equilibrium, where some particles are fully lithiated and others are fully delithiated[70] 54

Figure 2-2 Equilibrium state in a partially lithiated single Li_xFePO_4 particle. The particle cont ains an $FePO_4$ region, an $LiFePO_4$ region and potentially an intermediate solid solution region (ISSR) with volume fraction y_{ISSR}. 55

Figure 3-1: **(a)** Cation arrangement in ordered (left; the layered structure is shown as an exam ple) and disordered (right) structures. The layers displayed in the figure are the (111) planes of

the FCC cation sublattice. **(b)** The voltage of the disordered structure is larger than the voltage of the ordered structure if the disordering energy is larger in the delithiated limit than in the lith

iated limit $\left(\underline{E}^{dis}_{MO_2} - \underline{E}^{ord}_{MO_2}\right) > \left(\underline{E}^{dis}_{LiMO_2} - \underline{E}^{ord}_{LiMO_2}\right)$

(i). Conversely, the voltage of the disordered structure is smaller than the voltage of the ordere d structure if the disordering energy is smaller in the delithiated limit than in the lithiated limit

$\left(\underline{E}^{dis}_{MO_2} - \underline{E}^{ord}_{MO_2}\right) < \left(\underline{E}^{dis}_{LiMO_2} - \underline{E}^{ord}_{LiMO_2}\right)$**(ii)**. 65

Figure 3-2: **(a)** Disordering energy (with respect to the $LiMO_2$ ground state structure) for diffe rent transition metals, in the $LiMO_2$ and MO_2 limits. **(b)** Voltage difference between disordered $LiMO_2$ and the $LiMO_2$ ordered ground state **(c)** Absolute average voltage for fully disordered a nd ground-state $LiMO_2$ structures..... 71

Figure 3-3: Free energy landscape and ensuing voltage relations for compounds that disorder i n situ during **(a)** Lithiation **(b)** Delithiation..... 77

Figure 4-1: Different levels of cation disorder in $LiMO_2$ compounds **(a)** Fully ordered (e.g. lay ered) $LiMO_2$ compound (the layers being the (111) planes of the FCC cation sublattice) **(b)** Par tially disordered compound **(c)** Fully disordered rocksalt. 84

Figure 4-2: Factors that contribute to the voltage slope increase upon cation disorder in lithiu m transition metal oxides **(a)** In ordered (e.g. layered) compounds, the effective Li Va interacti on (J^{Li-Va}) controls how stable states of intermediate concentrations are relative to the $LiMO_2$ and MO_2 end members (i), which in turn controls the voltage slope (ii) **(b)** In disordered compo unds: (i) The statistical distribution of local environments around Li sites results in a statistical distribution of ΔE_{site} and (ii) Both J^{Li-Va} and $\sigma_{\Delta E_{site}}$ (the standard deviation of

ΔE_{site}) contribute to the voltage slope. **(c)** High voltage tetrahedral sites can be occupied by Li when all face sharing octahedral sites are vacant (i) This can occur in disordered $LiMO_2$ comp ounds via delithiation of "0 TM" tetrahedral sites, but not in the (stoichiometric) layered structu re, as each tetrahedral site has at least one transition metal neighbor. (ii) Tetrahedral Li occupan cy leads to a voltage increase at the end of charge, and a corresponding lowering of the voltage everywhere else to conserve the average voltage. 86

Figure 4-3: **(a)** Illustration of the voltage profile of fully disordered (i) $LiTiO_2$ and (ii) $LiNiO_2$ when Li insertion is restricted to octahedral sites. The black curves show the site energy contrib ution to the voltage slope, while the red curve shows the combined effect of ΔE_{site} and J^{Li-Va} **(b)** Additional high voltage contribution resulting from tetrahedral site occupancy in disordere d $LiMO_2$ (ΔV^{tet} in **Figure 4-2**(c)), as determined from the spinel structure. 94

Figure 4-4: Voltage slope and voltage range of fully disordered $LiMO_2$. **(a)** Voltage slope contr ibution from ΔE_{site}, $J^{Li\ Va}$ and tetrahedral Li for each compound **(b)** Site energy contribution to t he votlage slope as a function of the average voltage of the disordered structure. High voltage c ompounds have a lower (site energy induced) voltage slope than low voltage compounds, as ev idenced by the dashed trend line **(c)** Octahedral voltage slope increase upon full disorder of an i nitially layered $LiMO_2$ compound. The voltage slope increase is smaller for high voltage comp ounds, due to the smaller effect of the site energy induced slope. **(d)** Voltage range of fully diso rdered $LiMO_2$. The red bar represents the voltage range associated with octahedral Li insertion, while the blue bar highlights the additional high voltage contribution associated with insertion of Li in tetrahedral sites. The dashed line represents the 4.5V line, which represents a lower bo und for the electrolyte stability limit. 95

Figure 4-5: Effect of short-range order on the voltage profile of disordered $LiMO_2$ **(a)** Order-disorder transition at high temperature leads to a disordered but not fully random $LiMO_2$ struct ure **(b) (c)** Voltage profiles of $LiTiO_2$ and $LiMnO_2$ equilibrated at temperatures larger than the order disorder-transition temperature **(d)** Capacities above 4.5V for fully disordered and short-range ordered high voltage $Li(Fe,Ti)O_2$ compounds **(e)** Comparison of tetrahedral Li capacity i n fully disordered and short-range ordered $LiMO_2$ compounds. 101

Figure 4-6: Effect Li excess on the octahedral and tetrahedral Li capacity in layered and fully d isordered $Li_{1+y}M_{1-y}O_2$ **(a)** Tetrahedral environments in fully disordered and layered $LiMO_2$ **(b)** Breakdown of the octahedral, tetrahedral and total Li capacity in fully disordered $Li_{1+y}M_{1-y}O_2$ **(c)** Octahedral Li capacity as a function Li-excess for layered and fully disordered $Li_{1+y}M_{1-y}O_2$ **(d)** Octahedral capacity lost upon full disorder in $Li_{1+y}M_{1-y}O_2$..... 102

Figure 4-7: Accuracy of the pair term approximation for fully disordered $LiMO_2$. The black c olumns constitute the site energy induced slope using higher order interactions, while the red c olumns show the corresponding predictions by only considering pair terms. 112

Figure 4-8: Estimating the voltage increase resulting from tetrahedral Li occupancy (ΔV^{tet} in **Figure 4-2**(c)) using the spinel structure. **(a)** Delithiation of the spinel $LiMO_2$ structure along t he tetrahedral and octahedral pathways (Li is green, M is gray and O is red) **(b)** Energy hull of spinel $LixMO_2$ along the tetrahedral and octahedral pathways (x_{Li}=0, 0.5, 1) **(c)** The difference in the high voltage step of the octahedral and tetrahedral pathways, labeled ΔV^{tet} in the plot, is used to estimate the scale of the voltage increase at the end of charge in disordere d structures resulting from tetrahedral Li occupancy (ΔV^{tet} in **Figure 4-2**(c)) 113

Figure 5-1: **(a)** Particle initiating lithiation through a non equilibrium solid solution pathway a nd subsequently relaxing to a two phase state. **(b)** The final state after spinodal decomposition consists in a $LiFePO_4$ region, a $FePO_4$ region, and potentially and intermediate solid solution re gion (ISSR), with a volume fraction y_{ISSR} 119

Figure 5-2: Low energy orderings in the non equilibrium solid solution pathway in Li_xFePO_4, as determined by Density Functional Theory. **(a)** The non equilibrium solid solution pathway in Li_xFePO_4 is governed by the energetics of *ac* orderings (alternately lithiated/delithiated *ac* pla nes in proportion to the Li concentration) and is accessible at low overpotentials (~25mV). **(b)** In comparison, previously reported *bc* staging configurations can only be accessed at high over potentials (~215mV). 124

Figure 5-3: Comparing the free energy of a homogeneous solid solution with respect to the fre e energy of phase separation to a sharp *bc* or *ac* interface at different Li concentrations. Since t he effect of chemical interfacial energy is small for typical ~100 nm particles (0.5 meV/f.u. for a *bc* interface and 0.03 meV/f.u. for an *ac* interface), only the contribution of coherency strain energy to the energy penalty of phase-separation is considered. 127

Figure 5-4: Orientation of the most likely interface after spinodal decomposition. **(a) (c)** Spino dal decomposition from a homogeneous solid solution dominated by *ac* orderings through 1D Li diffusion along the *b* direction preferentially leads to the formation of an *ac* interface. **(d)** Sp inodal decomposition from a homogeneous solid solution state to a *bc* interface is unlikely, as i t requires an initial increase in the local bulk free energy (through the breaking of local *ac* orde rings), as well as significant diffusion in the *a* and *c* directions (several order of magnitudes lo wer than in the *b* direction). 129

Figure 5-5: : Illustration of the quenching experiment by Chen et al. 130

Figure 5-6: : Comparing the local free energy distribution of a homogeneous solid solution stat e and of a sharp *ac* interface In both cases, the Li concentration is set to $x_{Li} = 0.5$ at the particle level. **(a)** Contour plot of the coherency strain energy density profile resulting from a sharp *ac* i nterface **(b)** The local coherency strain energy density at different positions in the particle is co mpared with the non equilibrium solid solution free energy (line scan along the *b* direction, at 8 0% of the distance between the particle center and the external *bc* surface)..... 131

Figure 5-7: Thermodynamic stability of intermediate solid solution states after spinodal decom position to an *ac* interface. The energy penalty for a sharp interface and for a diffuse ISSR inter face (averaged over the entire particle) are compared, as a function of the volume fraction of th e ISSR (y_{ISSR}), for **(a)** a cubic particle and **(b)** an *ac* platelet particle (aspect ratios $L_b/L_a = L_b/L_c = 0.5$). 133

Figure 5-8: Qualitative map of the lithiation mechanism in $LiFeO_4$ single particles as a functio n of particle size and applied overpotential. Note that this map applies to the particles that are a ctively transforming in the electrode. 140

Introduction

1.1 Motivation

The automotive sector accounts for a large fraction of worldwide CO_2 emissions. In 2005, 15% of the world's CO_2 emissions were accounted for by the transportation sector.[1] As a result, national fuel consumption standards all over the world have become increasingly stringent. In the United States, CAFE standards ensure that the automotive fleet will have to meet, by 2025, an average mileage per gallon level of 50 mpg (or 4.1 liters per 100 km).[2] The partial or full electrification of the vehicle fleet is an important strategy towards achieving these fuel efficiency standards, and the recent years have seen a growth in the production of micro-hybrid, hybrid, plug-in hybrid and full electric vehicles.

To this day, Li-ion batteries remain the leading battery technology for electric automotive transport. In order to be competitive with traditional internal combustion engines, Li-ion batteries must achieve high energy density, high power density, high safety and low cost.

The energy density and power density of the positive electrode (cathode) are important performance-limiting factors in Li-ion batteries today. While commercial anodes (graphitic LiC_6) achieve high reversible capacities (i.e. charge per mass ration) of 372 mAh/g,[3,4] traditional layered transition metal oxide cathodes can only reversibly cycle between 170-180 mAh/g.[5-8] Furthermore, power densities in this class of materials is limited to several units of C

(where nC corresponds to (dis)charge in C / n hours), which make these compounds not suitable for high rate applications (such as regenerative breaking in micro-hybrid vehicles). Improving the energy and power density of the active cathode materials is therefore an important research vector in the field of Li-ion batteries today.

1.2 Overview of Li-ion batteries

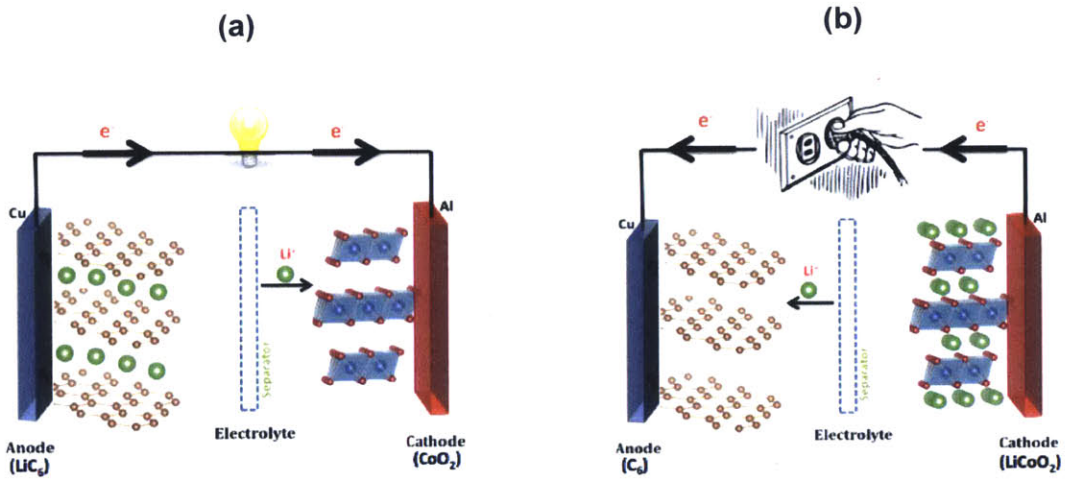

Figure 1-1 Schematic of a Li-ion battery operating (a) during discharge and (b) during charge[9]

Li-ion batteries function upon the principle of reversible (de)intercalation of Li in crystalline host structures (**Figure 1-1**). During discharge (**Figure 1-1**(a)), Li is transferred from the anode (where its sits at a high chemical potential), to the cathode (where its sits at a low chemical potential). During this process, Li^+ ions migrate between the two electrodes through the electrolyte, while electrons flow through the external circuit and produce useful work. During

charge (**Figure 1-1**(b)), an external potential difference is applied to the cell to transfer Li from the cathode (low chemical potential state) to the anode (high chemical potential state), which effectively reverses the process.

The open circuit voltage of a Li-ion battery, ΔV^{oc}, represents the maximum amount of energy deliverable during discharge per unit charge transferred. It is equal to the free energy change in the battery resulting from the exchange of Li from the anode to the cathode and can only be accessed in the limit of zero rates (during which Li exchange between the electrodes is a reversible process). The open circuit voltage is a function of the state of charge of the battery and is given by the difference in Li chemical potential between the anode and the cathode at each state of charge :

$$\Delta V^{oc}(x) = \frac{\mu_{Li}^{anode}(x) - \mu_{Li}^{cathode}(x)}{F} \qquad (1)$$

Where x is the state of charge in the battery, μ_{Li}^{anode} is the Li chemical potential in the anode (J/mol), $\mu_{Li}^{cathode}$ is the Li chemical potential in the cathode (J/mol) and F is Faraday's constant (96,5000 C/mol). An example of a voltage profile for a Li-ion battery cell containing a $LiCoO_2$ cathode and a metallic Li anode is illustrated in **Figure 1-2**. During discharge, the voltage decreases with the amount of charge transferred (this is a consequence of free energy minimization in the cell) while during charge, the voltage increases with the amount of charge transferred. The average open circuit voltage is defined as the average voltage value over the equilibrium charge/discharge profile. The average open circuit voltage is an important quantity, as it is one of the factor controlling the total energy density of the battery. (In this thesis, the

terms "average voltage" and "open circuit voltage" will be used interchangeably).

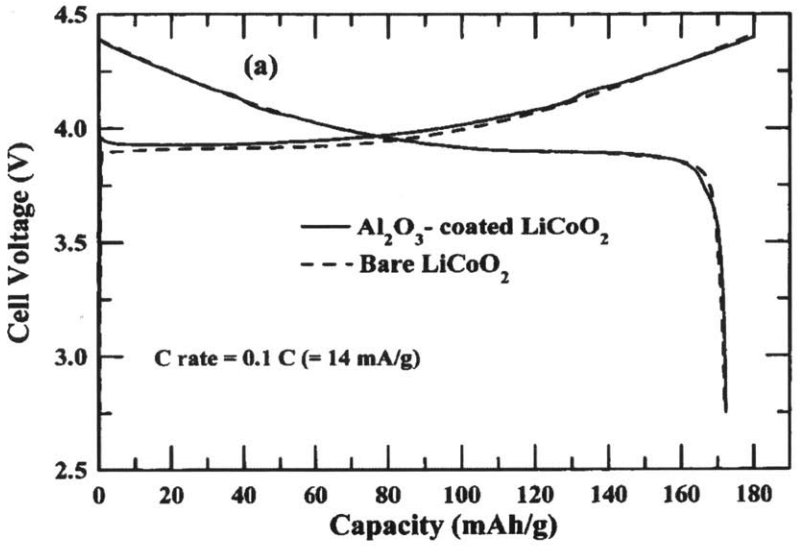

Figure 1-2 First cycle voltage profile of $LiCoO_2$ at a rate of 0.1C (charge-discharge in 10 hours)[5]

The energy density (Wh/l) of a Li-ion battery cell is the maximum amount of work that can be delivered, per unit volume of the cell. It can be decomposed into the product of three terms: the average open circuit voltage $\overline{\Delta V^{oc}}$ (V), the charge capacity C (Ah/g) and the volumetric density ρ (g/l) of the cell.

$$Energy\ Density = \overline{\Delta V^{oc}} \bullet C \bullet \rho \qquad (2)$$

The power density (W/l) is equal to the maximal amount of work deliverable per unit time. It is controlled by several processes in the battery, such as Li^+ conductivity in the electrolyte,

electronic conductivity in the active electrode materials and electronically conducting carbon network, charge transfer resistance at the cathode/electrolyte and anode/electrolyte interfaces and Li diffusivity in the electrode materials.

The ideal cathode materials must exhibit high energy and high power density. In addition, cathode materials must display good cyclability (capacity retention over thousands of charge/discharge cycles), high safety (retention of oxygen even at high temperatures) and low cost. To this day, no single cathode material simultaneously meets all these requirements, rendering the research field of Li-ion battery cathode both challenging and active.

1.3 Layered lithium transition metal oxides

Layered lithium transition metal oxides ($LiMO_2$) represent the current commercial standard for high-energy density cathodes in Li-ion batteries. Examples of successfully commercialized layered oxides include $LiCoO_2$ (LCO),[5] $LiNi_{0.8}Co_{0.15}Al_{0.05}$ (NCA),[6] and $LiNi_xMn_yCo_{1-x-y}O_2$ (NMC).[7] The layered structure corresponds to a particular cation ordering on the FCC $LiMO_2$ rocksalt lattice (**Figure 1-3**). The rocksalt $LiMO_2$ framework consists in two interpenetrating cation (Li and M) and anionic (O) FCC sublattices. Li and transition metals are octahedrally coordinated by oxygen (**Figure 1-3**(c)). In the layered structure, Li and transition metals alternately occupy the (111) planes of the FCC cation sublattice

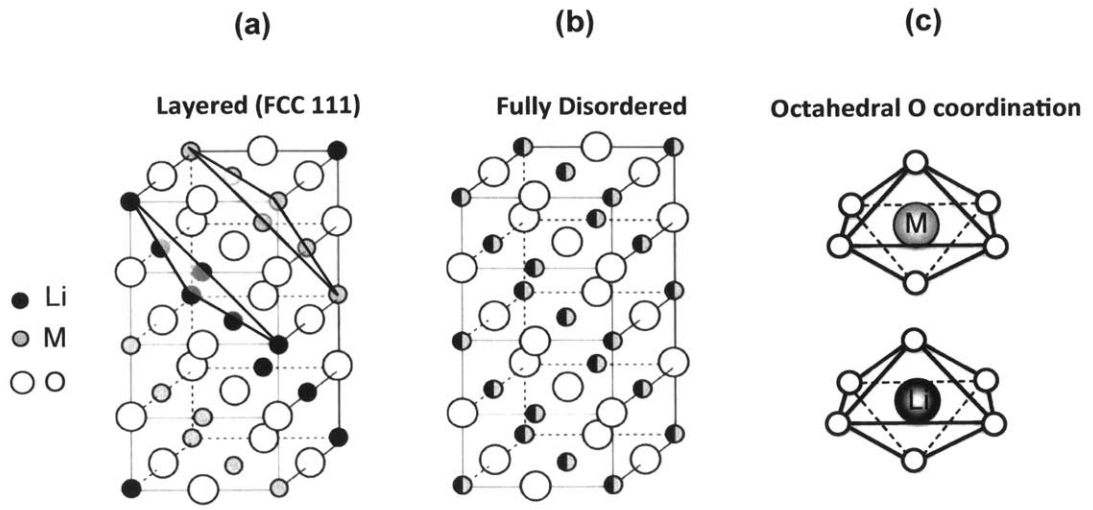

Figure 1-3 [10]Ordered and disordered structures on the $LiMO_2$ rocksalt lattice **(a)** In the layered structure, Li and M occupy alternate (111) layers of the FCC cation sublattice **(b)** In a fully cation-disordered rocksalt, cations randomly occupy sites of the FCC cation sublattice **(c)** In both ordered and disordered compounds, Li and M are octahedrally coordinated by oxygen.

Layered transition metal oxides however have several limitations. Reversible extraction of lithium from the pristine $LiMO_2$ limited is currently limited to ~0.6-0.7 Li, out of the one formula unit of Li that the pristine material contains. As a result, practical accessible capacities are on the order of 170-190mAh/g,[5-8] with respect to theoretical capacities of ~280 mAh/g. These limitations are partially caused by phase changes upon delithiation (which lead to mechanical degradation),[11] decrease in Li diffusivity upon deep delithiation due to interlayer shrinking[12] and instability of transition metal oxides with respect to oxygen evolution in the charged limit.[3,13] Furthermore, power densities in this class of materials is limited to several units of C (where nC corresponds to (dis)charge in C / n hours), which make these compounds not ideal for high rate applications.

The bulk of the Li-ion battery research cathode today aims at improving the performance of traditional layered transition metal oxides, through improvement in energy density and/or power density. In this thesis, we develop critical insights on two important classes of materials that respectively aim at improving the energy density and power density of layered oxides, namely high-capacity Li-excess cation-disordered rocksalts and high-rate $LiFePO_4$ olivine.

1.4 Li-excess cation-disordered rocksalts

(Full or partial) cation disorder is caused by (full or partial) cation mixing between the Li sublattice and the transition metal sublattice in an initially ordered structure (**Figure 1-4**). Depending on the degree of cation-mixing, a structure can be fully ordered (no cation-mixing between the Li and transition metal sublattice), partially disordered (partial cation-mixing between the Li and transition metal sublattice) or fully disordered (full cation-mixing between the Li and transition metal sublattice). In the limit of full disorder, occupancy of Li and transition metal sites are random and the structure is defined as a fully cation-disordered rocksalt (**Figure 1-3**(c) and **Figure 1-4**(c)). In the remainder of this thesis, the terms "cation-disordered" and "disordered" will be used interchangeably.

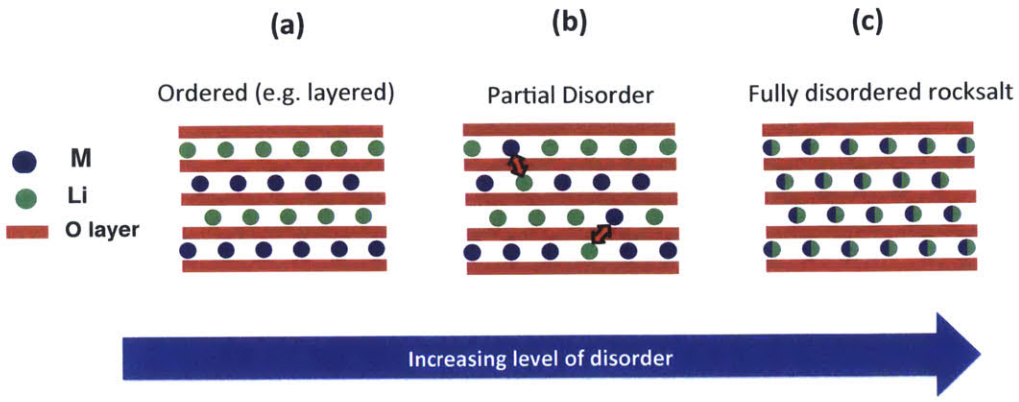

Figure 1-4 Different levels of cation disorder in $LiMO_2$ compounds **(a)** Fully ordered (e.g. layered) $LiMO_2$ compound (the layers being the (111) planes of the FCC cation sublattice) **(b)** Partially disordered compound **(c)** Fully disordered rocksalt. The view is shown along the (111) planes of the FCC cation sublattice.

Cation disorder has traditionally been avoided in stoichiometric layered transition metal oxides ("stoichiometric" refers to the absence of Li-excess or deficiency, i.e. $y=0$ in $Li_{1+y}M_{1-y}O_2$), as it leads to significant decrease in electrochemical performance in this family of compounds. This is caused by the decrease in Li diffusivity upon cation-mixing.[8] Li diffusion in the layered structure occurs via the divacancy mechanism.[12] In its activated state, Li is tetrahedrally coordinated by oxygen (terahedral site) and experiences electrostatic repulsion with the transition metal occupying one of the face-sharing octahedral sites. This diffusion pathway is called the "1-TM channel" (**Figure 1-5**(a)). Cation-mixing leads to a shrinking of the Li layer, as the ionic radius of $M^{3+/4+}$ is smaller than the ionic radius of Li^+. As a result, the height of the activated tetrahedron decreases, and Li^+ experiences a larger electrostatic repulsion with the high-valent transition metal. This leads to an increase in the activation barrier for Li migration (**Figure 1-5**(b), "1-TM" lines illustrated for face-sharing Mo^{4+} and Cr^{3+}). In stoichiometric

lithium transition metal oxides, cation disorder significantly decreases Li diffusivity, and therefore leads to a degradation of cycling performance. One such example is $LiCrO_2$, which has been shown not to cycle beyond the first charge due to the a formation of cation-disordered phase.[14] Conversely, decreasing the level of cation-mixing in stoichiometric lithium transition metal oxides can lead to significant increases in performance, such as is the case for $LiNi_{0.5}Mn_{0.5}O_2$.[8]

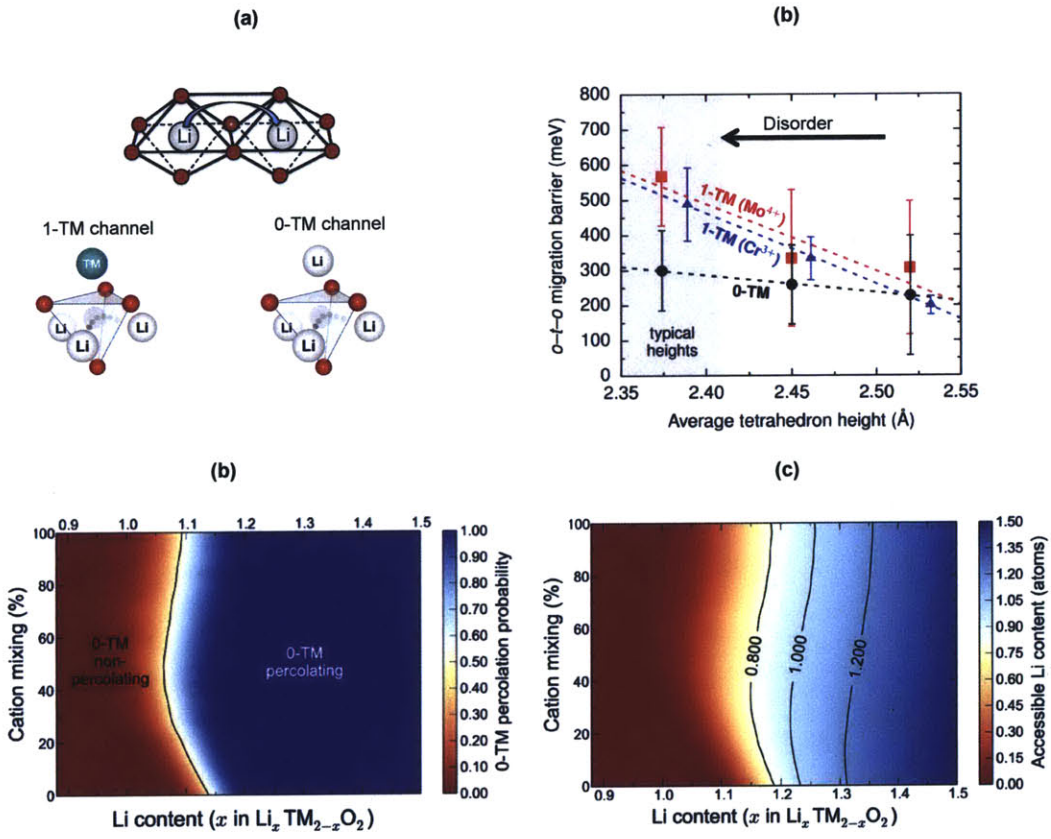

Figure 1-5 [15] Li diffusion in transition metal oxides **(a)** Li migration between octahedral sites occurs via an activated tetrahedral site. In stoichiometric layered $LiMO_2$, all activated tetrahedral sites have one face-sharing transition metal neighbor (1-TM diffusion channel). In cation-disordered rocksalts or in Li-excess compounds, some activated tetrahedral sites have no transition metal neighbors (0-TM channel) **(b)** Activation barriers for 1-TM and 0-TM channels. Only the 0-TM is active upon disorder **(c)** Percolation treshold for the 0-TM

diffusion channel as a function of the level of disorder and the Li-excess level **(d)** Amount of Li available along the percolation 0-TM pathway, as a function of the degree of disorder and the Li-excess level.

While partial or full cation disorder is detrimental to the performance of *stoichiometric* lithium transition metal oxides, it was recently shown that Li-excess can unlock fast diffusion pathways in cation-disordered rocksalts ($y > 0$ in $Li_{1+y}M_{1-y}O_2$). This recent discovery has opened the new and emerging field of high-capacity cation-disordered Li-excess cathode materials for Li-ion batteries. **Figure 1-5** shows how macroscopic diffusion can be achieved in cation-disordered rocksalts in the presence of Li-excess. In a cation-disordered rocksalt, the migrating Li^+ ions can sit in a variety of local environments. One of these environments is the "0-TM" environment, in which none of the face-sharing sites contain no high-valent transition metals. Li^+ ions sitting in 0-TM tetrahedral sites experience only a small electrostatic repulsion with other Li^+ ions. As a result, the activation barrier of this pathway is low and largely insensitive to the tetrahedron height (**Figure 1-5**(b)). In stoichiometric $LiMO_2$, the number of 0-TM tetrahedral sites is however not sufficient to create a percolating, macroscopic diffusion pathway in a cation-disordered rocksalt. This explains why stoichiometric $LiMO_2$ experience significant performance degradation upon cation-mixing, as the 1-TM channel is the only active diffusion pathway in these compounds. The introduction of Li-excess however, increases the probability for a given tetrahedral site to be a 0-TM site. Percolation theory shows that a sufficient amount of Li-excess can lead to percolation of the 0-TM pathway (**Figure 1-5**(c)). The percolation treshold depends on the degree of cation disorder in the structure. For fully disordered rocksalts, the introduction of 25% Li-excess (i.e. $Li_{1.25}M_{0.75}O_2$) leads to percolation of 1 formula unit of Li in the 0-TM diffusion pathway (**Figure 1-5**(d)).

High reversible capacity in Li-excess cation-disordered rocksalt based on 0-TM percolation theory has been experimentally demonstrated for $Li_{1.211}Mo_{0.467}Cr_{0.3}O_2$,[15] which was shown to reversibly cycle one formula unit of Li (~280mAh/g) at C/20 rates. Such high capacities are not accessible in stoichiometric Li transition metal oxides, as Li diffusivity significantly degrades at high delithiation levels (high activation barrier of the 1-TM pathway due to the shrinking of the Li layer upon delithation, as in **Figure 1-5**(b)). In the recent years, the emerging field of Li-excess cation-disordered has grown, with the synthesis of several high-capacity materials such as Li_2VO_3 ,[16] $Li_{1.2}Ni_{1/3}Ti_{1/3}Mo_{2/15}O_2$ [17] , $Li_{1.3}Nb_x(Mn,Fe,Co,Ni)_{2-1.3-x}O_2$ [18,19] and $Li_{1+x}Ti_{2x}Fe_{1-3x}O_2$.[20]

Despite being a promising avenue for high-capacity cathodes, important knowledge gaps prevent rational design of high-capacity Li-excess cation-disordered rocksalts. One such knowledge gap is the impact of cation disorder on the voltage profile of lithium transition metal oxides. Cation disorder can indeed both affect the average (open circuit) intercalation Li voltage of transition metal oxides, which controls the total energy density, and the (open circuit) voltage slope, which controls the accessible capacity below the stability limit of the electrolyte (currently 4.5V-4.7V for organic electrolytes). To this day, little work has been done on understanding the effect of cation disorder on the voltage profile of litium transition metal oxides. The only work on this topic was provided by Saubanere et al.[21] Using a simplified voltage model based on chemically intuitive quantities, Saubanere et al argued that the average voltage of cation-disordered rocksalts must be higher than their ordered homologues. In the

general Li-ion battery research community, it is also believed that cation disorder should increase the voltage slope of lithium transition metal oxides, by creating a range of local environments for Li sites, and hence a larger range of Li chemical potentials in the structure (**Figure 1-6**(a)-(b)).[15]

In Chapters 3 and 4 of this thesis, we use first principles methods to understand and quantify the effect of cation disorder on the voltage profile of lithium transition metal oxides .

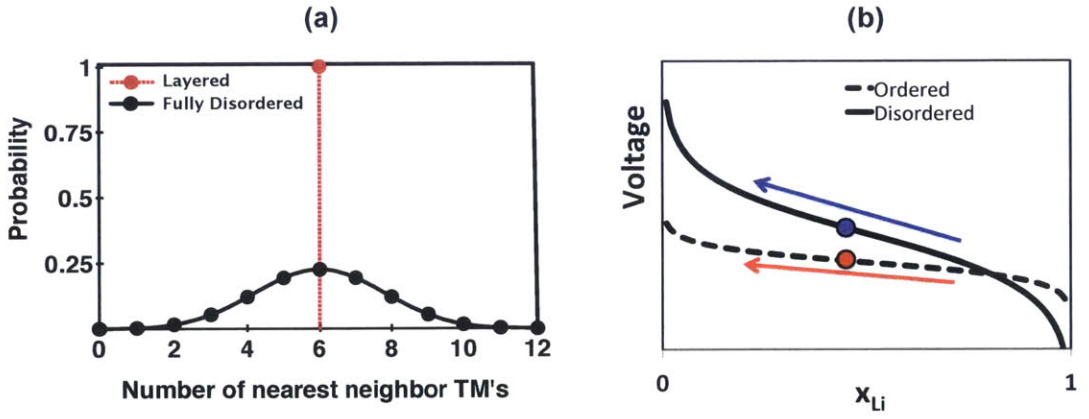

Figure 1-6 (a) Cation disorder creates a spread of local environment around Li sites **(b)** Cation disorder is expected to increase the voltage slope of Li transition metal oxides (blue and red arrows) as well as to modify their average Li intercalation voltage (blue and red dots)

1.5 Surface cation disorder in layered oxides

In addition to being relevant to the field of disordered Li-excess rocksalts, cation disorder is also becoming an increasingly important phenomenon in the field of layered Li transition metal oxides. Several layered cathode materials, such as $LiNi_{0.8}Co_{0.15}Al_{0.05}O_2$ [22] and Li-excess $Li_{1+y}Ni_wMn_zCo_{1-y-z}O_2$,[23] form (partially or fully) disordered surface phases upon deep

delithiation. This process is believed to be triggered by oxygen evolution at the particle surface [24,25] (delithiated lithium transition metal oxides are thermodynamically unstable with respect to oxygen evolution[3,13]), followed by back-diffusion of transition metals (**Figure 1-7**) . This densification process leads to the formation of partially or fully disordered surface phases with a decreased Li-M ratio.[17,26-28] The thickness of these surface layers can be as high as 10-20 nm. [23,27-29]11

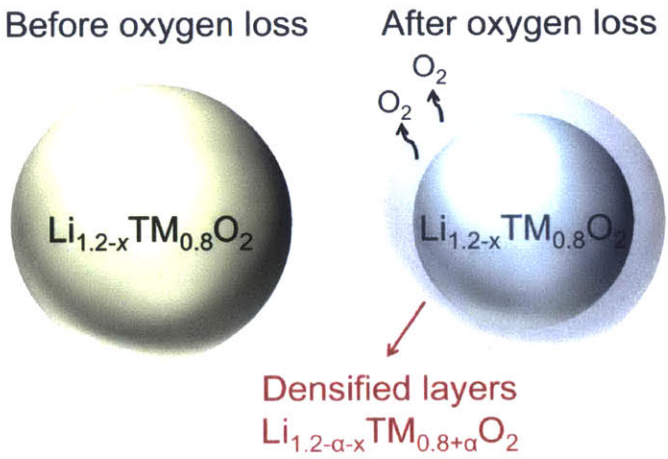

Figure 1-7 [17] Formation of disordered surface layers triggered by oxygen loss (illustrated for $Li_{1.2}M_{0.8}O_2$ compound).

Cation disorder in these densified phases is expected to lead to poor Li transport. In order for Li diffusion to be facile in a partially or fully disordered phase, a sufficient level of Li-excess must be present, so that the facile 0-TM pathway can percolate through the structure. In layered $LiMO_2$, the Li content at the surface following densification is certain to be below the percolation treshold, as the pristine material does not contain Li-excess. In the case of layered Li-excess compounds, the Li-level resulting from densification may or may not sit below the percolation treshold. It is however certain that a decrease in the Li/M ratio at the surface will

lead to a decrease in the amount of Li sites accessible via the 0-TM percolation pathway, and hence a decrease in Li transport.

The measured voltage in a core-shell particle with poor Li surface transport can be strongly affected by the voltage profile of the surface region. Poor surface Li transport in a core-shell particle indeed leads to a situation where the surface and the bulk of the particle are not at thermodynamic equilibrium with each other (when the particle is cycled at finite rates). As a result, the measured voltage at the electrode scale can be strongly affected by the voltage profile of the particle surface, where Li insertion/extraction occurs. Understanding the effect of cation disorder on the voltage profile of transition metal oxides is therefore critical to understand the voltage evolution of layered lithium transition metal oxides subject to surface disorder.

1.6 High power $LiFePO_4$ olivine

$LiFePO_4$ is an important commercial cathode for high-rate applications and vastly out-performs layered $LiMO_2$ oxides in this sector. Furthermore, $LiFePO_4$ is an intrinsically safe cathode material, with a high O_2 evolution temperature.[30] The low voltage of the $Fe^{2+/3+}$ redox (3.4 V vs. Li/Li^+)[31] , however, leads to a lower energy density then layered transition metal oxides (~3.8V for $LiCoO_2$ [5]) and restricts the applicability of $LiFePO_4$ to high-rate, low energy applications. One such important application is regenerative breaking in micro-hybrid vehicles.

The olivine structure of $LiFePO_4$ can be described as a distorted hexagonal close-packed (HCP) oxygen lattice with P occupying tetrahedral sites and Fe and Li occupying octahedral

sites (**Figure 1-8**(a)).[32] Li occupy M1 octahedral sites forming 1D chains of edge-sharing octahedra along the b direction while Fe occupy M2 octahedral sites forming 2d sheets of corner sharing octahedra in the bc plane[32]. Upon intercalation of Li in the $FePO_4$ structure, Li^+ intercalates on the Li sites while its associated electron reduces Fe^{3+} to Fe^{2+}. Li diffusion occurs via 1D migration along the crystallographic *b* direction (010) (**Figure 1-8**(b)).[33-35]

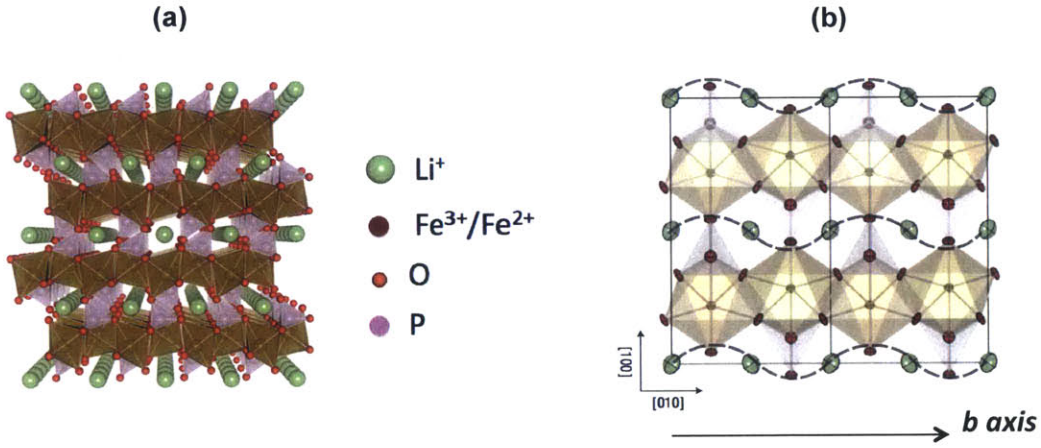

Figure 1-8 [33] **(a)** Crystal structure of $LiFePO_4$ **(b)** Li diffusion is dominated by 1D diffusion along the crystallographic b direction (010)[33]

Capacities as high as 130 mAh/g (out of the theoretical 170 mAh/g) have been achieved at a 50 C rate (where *n* C corresponds to full (dis)charge in 1 / *n* hours) in $LiFePO_4$, and rates as high as 200 C and 400 C have been achieved by removing kinetic limitations at the electrode level (**Figure 1-9**(a)).[36-40] These high rates are accessible only when the particle size is reduced to the nano-scale (~50-100 nm, **Figure 1-9**(b)), a limitation that has been attributed to reduced Li mobility due to channel-blocking anti-site defects that are present in larger particles.[35,41,42]

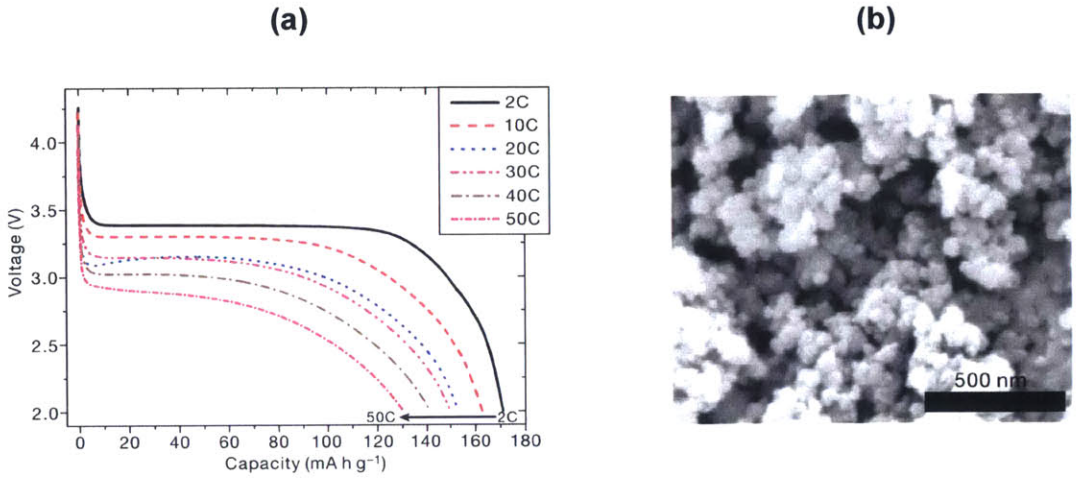

Figure 1-9 [40]**(a)** High-rate performance of $LiFePO_4$ **(b)** Particle nano-sizing is required to reach high performances (~50-100 nm)

Despite its commercial adoption, the fundamental lithiation mechanisms in $LiFePO_4$ single particles are not fully understood and remains an object of debate in the $LiFePO_4$ literature. The complication comes from the two-phase nature of $LiFePO_4$. At thermodynamic equilibrium, Li_xFePO_4 phase-separates into a nearly fully-delithiated phase and a nearly fully-lithiated phase ((Li_xFePO_4 ➔ $xLiFePO_4 + (1-x)FePO_4$)). Early lithiation models of $LiFePO_4$ single particles predicted lithiation to be initiated by a nucleation event[43-46] followed by two-phase growth along the elastically favorable crystallographic *bc* plane.[45,46] However, overpotentials in practical electrochemical conditions are low and thus unlikely to provide enough driving force to overcome the nucleation barrier required to form the critical nucleus.[47] (Overpotentials as low as 20mV are sufficient to cycle entire electrodes[48]).

A solution to the apparent discrepancy between the high-rate capabilities and the the two-phase nature of $LiFePO_4$ was first proposed by Malik et al.[47,49] Using Density Functional Theory

(DFT), the authors identified a non-equilibrium solid-solution pathway accessible at low overpotentials (~30mV), which circumvents the kinetically prohibitive nucleation step and enables homogeneous lithiation at low overpotentials. Since then, with the development of advanced *in situ* characterization techniques, the presence of solid-solution states during electrochemical (de)lithiation has been experimentally demonstrated. Several *in situ* X-Ray Diffraction (XRD) experiments have identified lattice parameters intermediate to those of the equilibrium $FePO_4$ and $LiFePO_4$ phases, at (dis)charge rates varying from 0.1 C to 60 C.[50-53]

A key mystery that remains to be elucidated, however, is the persistence of solid-solution states in single particles at *low-to-moderate* C-rates, (for example, rates in the 0.1 C - 5 C range). Due to the concave shape of the non-equilibrium solid-solution free energy, homogeneous solid-solution states are unstable with respect to small inhomogeneities in Li concentration (**Figure 1-10**). Considering the high diffusivity of Li in $LiFePO_4$ ($D \sim 10^{-8}$-10^{-10} cm^2/s, from Density Functional Theory[34] and muon-spin relaxation[54] respectively), Li diffusion in a 100 nm particle can occur on time scales as rapid as 1-100 ms, [a] which is much faster than the typical time required to lithiate a single particle. In summary, while each particle is expected to initiate (de)lithation through a non-equilibrium solid solution, it remains surprising that homogeneous solid-solution states could persist at low-to-moderate C-rates despite their thermodynamic instability.

[a] These values were obtained using Fickian scaling $t \sim r^2/D$, with the theoretical and experimental values of D provided above.

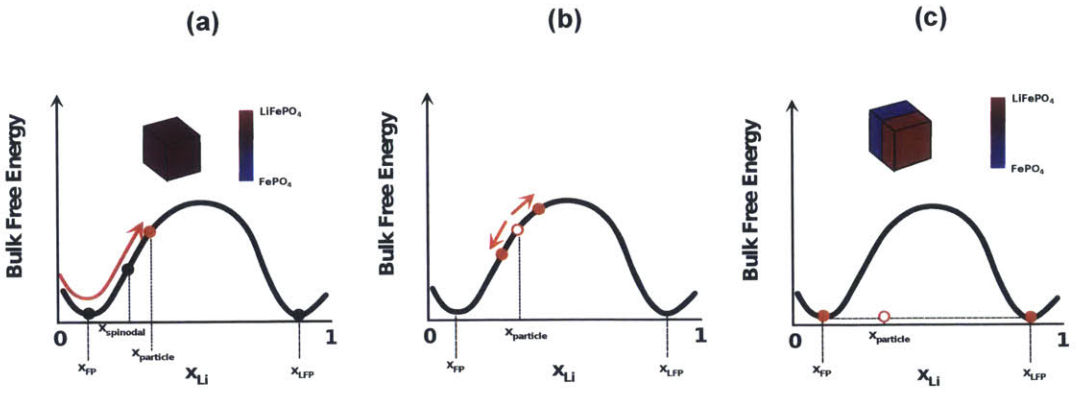

Figure 1-10 After initiating lithiation via a non-equilibrium solid solution, $LiFePO_4$ particles are expected to rapidly phase-separate **(a)** Lithiation initiates via the non-equilibrium solid solution pathway **(b)** Past the spinodal point, states of uniform concentration are unstable with respect to small fluctuations in concentration **(c)** The expected final state consists in a two-phase coexistence within the particle

In this thesis, we use a combination of first principles calculations and continuum elasticity to elucidate the persistence of solid-solution states during the (dis)charge of $LiFePO_4$ electrodes at low-to-moderate C-rates.

1.7 Overview of the thesis

This thesis uses first principles methods to provide critical insights on the voltage profile of high-capacity cation-disordered rocksalts as well as to understand the fundamental lithiation mecanisms in high-power $LiFePO_4$ olivine.

In Chapter 3, we use first principles calculations to investigate the effect of cation disorder on the average voltage of Li transition metal oxides, which controls the total accessible electrochemical energy upon disorder. We demonstrate that cation disorder increases the average voltage of some transition metals while it lowers the average voltage of others, depending on the relative disordering energy of the compound in the lithiated and delithiated limits. We further demonstrate that the disordered $Ni^{3+/4+}$ voltage is high and thus potentially hard to access upon first charge. Finally, we establish voltage evolution rules for transition metal oxides that disorder upon cycling.

In Chapter 4, we use first principles calculations to investigate the effect of cation disorder on the voltage slope of Li transition metal oxides, which controls the capacity accessible below the stability limit of the electrolyte. We combine lattice models and Monte Carlo techniques to demonstrate that cation disorder increases the voltage slope of Li transition metal oxides via an increase in the site energy distribution and extended availability of tetrahedral Li sites. We further demonstrate that high voltage transition metals generally display a lower voltage slope than low voltage transition metals. We finally demonstrate that short-range order plays a critical role in decreasing the voltage slope of disordered compounds with respect to the fully random limit, and that the additional high-voltage tetrahedral capacity induced by disordering

is smaller in Li-excess compounds than in stoichiometric compounds.

In Chapter 5, we investigate the lithiation mechanisms in $LiFePO_4$ nano-particles and elucidate the origin of the thermodynamic stability of intermediate solid solution states at low-to-moderate C-rates. We demonstrate that, given the symmetry of the low-energy solid-solution Li/Va orderings in Li_xFePO_4 and the 1D character of Li diffusion, spinodal decomposition from a solid solution preferentially leads to the formation of a diffuse high-strain *ac* interface with a *large intermediate solid-solution region,* as opposed to the commonly assumed sharp *bc* interface. Our first principles predictions not only rationalize the persistence of solid-solution states at low-to-moderate C-rates in high-rate $LiFePO_4$ electrodes, but also explain the observations of large intermediate solid-solution regions at an *ac* interface in single Li_xFePO_4 particles quenched from a high-temperature solid solution.

This thesis therefore provides important voltage-based design rules for the emerging field of high-capacity Li-excess cation-disordered rocksalts and establishes new understanding of the fundamental Li insertion mechanisms in high-rate $LiFePO_4$ nanoparticles.

Chapter 2 :

Methods

In this chapter, we present the computational methods used in this thesis. Density Functional Theory, cluster expansions, Monte Carlo techniques, Special Quasi-Random Structures and the thermodynamics of phase-separating systems are presented.

2.1 Density Functional Theory

Calculating ground-state energies for specific Li/Va arrangement in crystalline host structures is an integral part of this thesis. This can be achieved in principle by solving the multi-body Schrodinger equation on a periodic unit cell. For a unit cell containing M nuclei of atomic number Z_k and therefore $N = \sum_k Z_k$ electrons, the ground-state energy E_0 is obtained by solving the following minimization problem over all normalized wavefunctions Ψ :

$$E_0 = \min_{\Psi} \langle \Psi | H | \Psi \rangle \tag{3}$$

$$H = \sum_{i=1}^{N} -\frac{\hbar^2}{2m_i}\nabla^2 - \sum_{i=1}^{N}\sum_{k=1}^{M}\frac{Z_k e^2}{4\pi\varepsilon_0\|\boldsymbol{r}_i - R_k\|} + \frac{1}{2}\sum_{i=1}^{N}\sum_{j=1,j\neq i}^{N}\frac{e^2}{4\pi\varepsilon_0\|\boldsymbol{r}_i - \boldsymbol{r}_j\|} + \frac{1}{2}\sum_{k=1}^{M}\sum_{l=1,l\neq k}^{M}\frac{Z_k Z_l e^2}{4\pi\varepsilon_0\|\boldsymbol{R}_k - R_l\|} \tag{4}$$

In equation (4), H is the Hamiltonian operator, r_i is the position of the i^{th} electron, R_k is the position of the k^{th} nuclei, m is the mass of the electron, $\hbar$ is Planck's constant and ε_0 is the vacuum permittivity. The Hamiltonian operator is the sum of the kinetic energy of electrons, the electrostatic attraction between electrons and nuclei, the electrostatic repulsion between electrons and the electrostatic repulsion between nuclei. The kinetic energy of the nuclei, which is much smaller than the kinetic energy of electrons in solid compounds at room temperature, is neglected. The set of nuclei positions R_k therefore effectively acts as a minimization parameter (Born-Oppenheimer approximation) and will not be explicitly tracked in the subsequent equations presented in this section. Further note that a constraint exists on the wavefunction, which must be antisymmetric with respect to exchange of any two variables r_i and r_j (Pauli principle).

Direct numerical resolution of equation (3) is difficult. Discretization of the spatial grid into P points for example, leads to a system of P^{3N} unknowns to describe the wavefunction. The number of unknown values therefore scales exponentially with the number of electrons in the system, rendering direct resolution rapidly intractable for realistic systems. Density Functional Theory (DFT) overcomes this difficulty by reformulating the minimization problem (4) via the charge density $n(\boldsymbol{r})$ instead of the wavefunction Ψ. The charge density is defined as:

$$n(\boldsymbol{r}) = N \int_{r_2} (...) \int_{r_N} \Psi(r, r_2, ..., r_N) \Psi^*(r, r_2, ..., r_N) d^3 r_2 (...) d^3 r_N \qquad (5)$$

Note that equation (5) takes advantage of the exchange (anti)symmetry of the wavefunction. Reformulating the problem in terms of the electronic density dramatically reduces the

complexity of the system (P^3 unknowns instead of P^{3N} for spatial discretization; note however that spatial discretization of r is not the method employed in DFT). This reformulation is possible by virtue of the Hohenberg-Kohn theorem,[55] which states that there exists a one-to-one correlation between the ground-state charge density $n_0(\boldsymbol{r})$ and the external potential V_{ext}. The external potential is defined as the interaction terms between the electrons and the nuclei :

$$\left\langle \Psi \left| -\sum_{i=1}^{N}\sum_{k=1}^{M} \frac{Z_k e^2}{4\pi\varepsilon_0 \|\boldsymbol{r}_i - R_k\|} \right| \Psi \right\rangle = \int v_{ext}(\boldsymbol{r}) n(\boldsymbol{r})\, d^3\boldsymbol{r} \tag{6}$$

According to the Hohenberg-Kohn theorem, there therefore exists a universal functional $\boldsymbol{F}[n]$ such that:

$$\boldsymbol{E}_0 = \mathbf{min}_n \left(F[n] + \int v_{ext}(\boldsymbol{r}) n(\boldsymbol{r})\, d^3\boldsymbol{r} \right) \tag{7}$$

Although this functional exists in principle, it is not known. The challenge of DFT is to find accurate approximations for this unknown functional. The Kohn-Sham *ansatz*[56,57] provides a framework for achieving this. The assumption behind the Kohn-Sham *ansatz* is that the exact charge density can be represented by the ground-state of an auxiliary system of non-interacting particles :

$$\Psi_{KS}(r_1, \ldots, r_N) = \phi_1(r_1) \ldots \phi_N(r_N) \tag{8}$$

The energy of the auxiliary system is:

$$\langle \Psi_{KS}|H|\Psi_{KS}\rangle = \sum_i \left\langle \phi_i \left| \frac{-\hbar^2}{2m}\nabla^2 \right| \phi_i \right\rangle + \int v_{ext}(\boldsymbol{r}) n(\boldsymbol{r})\, d^3\boldsymbol{r} + \frac{1}{2}\int \frac{n(\boldsymbol{r})n(\boldsymbol{r}')}{4\pi\varepsilon_0 \|\boldsymbol{r}-\boldsymbol{r}'\|} d^3\boldsymbol{r} d^3\boldsymbol{r}' + E_{xc}[n] \quad (9)$$

The first term is the kinetic energy of a set of independent electrons, the second term is the contribution of the external potential, the third term is the Hartree potential of a classical distribution of positive charges and the third term is the exchange-correlation energy E_{xc}. E_{xc} adds the effects of the anti-symmetry of the wave function (exchange) and the correlation between electrons (correlation), which are omitted by virtue of the form of the Kohn-Sham wavefunction (equation (8)). The Kohn-Sham ansatz therefore states that the unknown functional of the charge density can be decomposed the following way:

$$F[n] = T_i[n] + E_{Hartree}[n] + E_{xc}[n] \quad (10)$$

Where T_i is the kinetic energy of independent electrons. The auxiliary Kohn-Sham equations amount to solving the following eigenvalue problem :

$$H_{KS}\,\phi_i = \varepsilon_i \phi_i \quad (11)$$

Where :

$$H_{KS} = \frac{-\hbar^2}{2m}\nabla^2 + v_{ext}(\boldsymbol{r}) + \int \frac{n(\boldsymbol{r}')}{4\pi\varepsilon_0 \|\boldsymbol{r}-\boldsymbol{r}'\|} d^3\boldsymbol{r}' + v_{xc}[n] \quad (12)$$

$$v_{xc}[n] = \frac{\delta E_{xc}[n]}{\delta n} \tag{13}$$

Note that, in equation (13), δ is a functional derivative. The art of DFT therefore consists in developing accurate exchange-correlation functionals for $v_{xc}[n]$. Several functional forms have been proposed in the literature. Once a functional form is established, its parameters are fitted to simple systems (e.g. the homogeneous electron gas) using more accurate but computationally expensive first principles methods such as Quantum Monte Carlo.

In this thesis, the Hubbard-U corrected Generalized Gradient Approximation (GGA+U) approximation to DFT is used. The GGA framework consists in a family of functionals in which the exchange correlation potential is expressed as a local integral of the charge density, as well as its spatial gradient:[58]

$$E_{xc}[n] = \int v_{xc}[n(r), \nabla n(r)] n(r) d^3r \tag{14}$$

In this work, we use the Purdue-Berk-Ernzerhof (PBE) functional. The U correction is a Hubbard-like correction applied to d orbitals of transition metals to remove spurious self-interactions, allowing charge to localize on the transition metal.[59,60] The PBE+U framewok has been shown to accurately predict the redox levels of transition metal oxides and polyanionic systems to within ~0.1V. In this thesis, U values for transition metal oxides are taken from the work of Jain et al[61] (experimental fit on oxide formation energies), while the U value for

$LiFePO_4$ is taken from the self-consistent evaluation of Zhou et al.[62]

Lastly, a few words will be mentioned on the numerical resolution of the Kohn-Sham equations. Following the Bloch theorem, wave functions in a periodic potential have the following form:

$$\Psi(\boldsymbol{r}) = e^{i\boldsymbol{k}\cdot\boldsymbol{r}}\varphi_{n,k}(\boldsymbol{r}) \tag{15}$$

Where k is a wave-vector in the first Brillouin zone, n is a band index and $\varphi_{n,k}(\boldsymbol{r})$ is a function that shares the same periodicity as the unit cell. This theorem is leveraged to solve the Kohn-Sham equations. k-points are sampled in the first Brillouin zone with a fixed density (such that the product of the nominal number of k-points and the number of atoms in the cell is on the order of 1000-2000), $\varphi_{n,k}(\boldsymbol{r})$ is expressed in a plane wave basis using a sufficient number of basis functions (energy cutoff ~ 520eV). Furthermore, core electrons are not explicitly represented in the Kohn-Sham equations but are instead taken into account via pseudo-potentials (Projector-Augmented Method[63]).

2.2 Cluster Expansions

Cluster expansions[64,65] are useful tools to map lattice dependent quantities, such as the total energy, onto a set of finite cluster interactions (pair interactions, triplet interactions, etc). Once fitted to a finite set of DFT energy calculations, cluster expansions can be used in conjunction with Monte Carlo methods to calculate thermodynamic quantities, such as the chemical

potential $\mu(x)$, from which the open circuit voltage $\Delta V^{oc}(x)$ can be derived. In this thesis, cluster expansions are used to calculate the average voltage of fully disordered $LiMO_2$ rocksalts, as well as to estimate their voltage slope. Both binary (A-B system) and ternary cluster expansions (A-B-C systems) are used. The following section presents the theoretical foundations behind cluster expansions, as well as the method employed to fit them.

Consider a lattice containing N sites, and consider that each site can be occupied by m distinct species. Several quantities need to be defined before the formal definition of a cluster expansion is presented. An occupation variable σ_i is defined for each site of the lattice. In the binary case where each site can be occupied by species A or B, a common choice of the occupation variable is $\sigma_i = \{1,-1\}$ for $\{A,B\}$, respectively. For a ternary system where each site can be occupied by species A,B or C , a common choice of the occupation variable is $\sigma_i = \{1,0,-1\}$ for $\{A,B,C\}$ respectively. Each configuration on the lattice is expressed by an occupation vector $\boldsymbol{\sigma} = (\sigma_1, \ldots, \sigma_N)$. A series of m-1 site functions θ_s ($s \in [0, m-1]$) are defined on each site. In a binary system, the unique point function is $\theta_1(\sigma_i) = \sigma_i$. In a ternary system, the two point functions are $\theta_1(\sigma_i) = \sigma_i$ and $\theta_2(\sigma_i) = \sigma_i^2$ (note that this choice of point functions is not unique and that other possible sets of functions can be used[65]). Consider a specific cluster α (pair of sites, triplet of sites, etc) containing l sites (l=2 for pairs, l=3 for triplets, etc). A vector of point function indices, s, is defined over all sites in the cluster: $\{s\} = (s_1, \ldots, s_i, \ldots, s_l)$. To each cluster is associated l^{m-1} cluster functions (one for each possible value of $\{s\}$): $\phi_\alpha^s(\boldsymbol{\sigma}) = \prod_{i \in \alpha} \theta_{s_i}(\sigma_i)$. With these definitions in place, the general expression of a cluster expansion can be written as:

$$E(\boldsymbol{\sigma}) = \sum_{\alpha} \sum_{\{s\}} J_{\alpha}^{\{s\}} \phi_{\alpha}^{\{s\}}(\boldsymbol{\sigma}) \tag{16}$$

Where $J_{\alpha}^{\{s\}}$ is the Effective Cluster Interaction (ECI) associated with the cluster function $\phi_{\alpha}^{\{s\}}$. Symmetry considerations reduce the number of independent variables in the expansion. All symmetrically equivalent clusters must share the same set of ECI's, such that the expansion can be re-written:

$$E(\boldsymbol{\sigma}) = \sum_{\alpha} \sum_{\{s\}} m_{\alpha} J_{\alpha}^{\{s\}} \bar{\phi}_{\alpha}^{\{s\}}(\boldsymbol{\sigma}) \quad , \quad \bar{\phi}_{\alpha}^{\{s\}}(\boldsymbol{\sigma}) = \frac{1}{m_{\alpha}} \sum_{\alpha_i \in \alpha} \phi_{\alpha_i}^{\{s\}}(\boldsymbol{\sigma}) \tag{17}$$

Where α is summed over all symmetrically distinct clusters, each with multiplicity m_{α}. The term $\bar{\phi}_{\alpha}^{\{s\}}(\boldsymbol{\sigma})$ is the correlation of the configuration over the cluster function $\phi_{\alpha}^{\{s\}}$.

In the binary case, the explicit expression of equation is given by:

$$E(\boldsymbol{\sigma}) = J_0 + J_{\text{point}} \sum_i \sigma_i + \sum_{\alpha \in pairs} J_{pair\,\alpha} \sum_{(i,j) \in \alpha} \sigma_i \sigma_j + \sum_{\alpha \in triplets} J_{triplet\,\alpha} \sum_{(i,j,k) \in \alpha} \sigma_i \sigma_j \sigma_k + (\ldots) \tag{18}$$

Where pair clusters include the nearest neighbor pair, the next nearest neighbor pair, etc. (Note that, to simplify, we assume that the lattice has one symmetrically distinct site, such as is the case in the rocksalt lattice). In the ternary case, cluster expansions have the following and somewhat more complex form:

$$E(\boldsymbol{\sigma}) = J_0 + J^{(1)}_{\text{point}} \sum_i \sigma_i + J^{(2)}_{\text{point}} \sum_i \sigma_i^2$$

$$+ \sum_{\alpha \in pairs} \sum_{(i,j) \in \alpha} \left(J^{(1,1)}_{\text{pair}\,\alpha} \sigma_i \sigma_j + J^{(1,2)}_{\text{pair}\,\alpha} \sigma_i \sigma_j^2 + J^{(2,1)}_{\text{pair}\,\alpha} \sigma_i^2 \sigma_j + J^{(2,2)}_{\text{pair}\,\alpha} \sigma_i^2 \sigma_j^2 \right) \qquad (19)$$

$$+(...)$$

Note, that if the expansion were to be pursued to triplets, it would include eight cluster functions, and correspondingly eight ECI's, for each triplet term ($J^{(a,b,c)}_{triplet\,\alpha} \sigma_i^a \sigma_j^b \sigma_k^c$, where $\{a,b,c\} = \{1,2\}$). Site symmetry considerations can also reduce the number of independent ECI's for each cluster. In a lattice where each site is equivalent (such as is the case in the rocksalt lattice studied in this thesis), the pair term ECI's $J^{(1,2)}$ and $J^{(2,1)}$ are guaranteed to be equal. Regardless of the available symmetry, the expansion expressed in equation (19) is general.

In principle, a cluster expansion is exact if all terms up to the N-tuplets are considered (where N is the number of sites in the lattice). In practice, it is sufficient to truncate the expansion to a finite set of ECI's, typically by reducing it to pair, triplets and quadruplet clusters and by setting, for each type of cluster, a cutoff radius beyond which clusters are not considered.

Fitting a cluster expansion requires a sufficiently large set of input energies obtained from first principles. The challenge in fitting a cluster expansion is to select the smallest possible number of relevant clusters that most accurately fit the input energies. Furthermore, cluster expansions must have predictive power, such that configurations that are not in the fit are accurately represented by the cluster expansion. The predictive quality of a cluster expansion fit is

estimated by its cross-validation (CV) score, which represents a quantitative measure of the predictability of the fit. The CV score is generally calculated using the "leave one out" algorithm. For a cluster expansion fitted to the DFT energy of M configurations, the CV score is calculated by performing cluster expansions on *M-1* configurations and calculating the error of the configuration that was left out. The CV score is then calculated by taking the root mean squared value of this ensemble of errors (obtained by sequentially leaving out each of the M configurations in the fit).

$$CV = \sqrt{\frac{1}{M}\sum_{i=1}^{M}\left(E_i^{CE\ with\ i\ left\ out} - E_i\right)^2} \tag{20}$$

In this thesis, cluster expansions are fitted using the compressive sensive method.[66] This method, which originated from signal processing theory, aims at fitting a cluster expansion with the smallest possible number of ECI's. It follows the physical intuition that only a handful of short-range interactions are relevant. Compressive sensing meets this requirement by simultaneously minimizing the L^1 norm of the solution vector (in other words the number of ECI's in the fit) as well as the L^2 norm of the error resulting from the ECI fit:

$$\mathbf{min}\left(\mu\left\|\underline{J}\right\|_{L_1} + \left\|\underline{\underline{C}}\,\underline{J} - \underline{E}\right\|_{L_2}\right) \tag{21}$$

In equation (21) , $\underline{J}$ is the vector of ECI's considered in the fit, $\underline{E}$ is a vector containing the list of input energies and $\underline{\underline{C}}$ is the correlation matrix. The L_1 norm $\left\|\underline{J}\right\|_{L_1}$ is used as a proxy to count the number of non-zero ECI's. μ is an adjustable parameter that weighs the importance of

having a sparse ECI solution with respect to having an accurate fit. The minimization problem is fitted using the split Bregman algorithm, as described by Nelson et al.[66]

2.3 Statistical Mechanics via Monte Carlo

Once a cluster expansion is constructed, thermodynamic quantities such as chemical potentials can be accurately calculated using Monte Carlo algorithms. In this thesis, we use Monte Carlo methods to calculate the Li chemical potential as a function of Li concentration $\mu_{Li}(x_{Li})$. The Li chemical potential determines the open circuit voltage via the relation:

$$e\Delta V^{oc}(x_{Li}) = -\mu_{Li}(x_{Li}) + C \tag{22}$$

Where the constant C is a reference chemical potential that is set to the chemical potential of Li in its metallic form. (As a result, all voltages reported in this thesis are given with respect to metallic Li, which is a common practice in the Li-ion battery community.) According to statistical mechanics, the lithium concentration can be expressed as a function of the Li chemical potential via a Boltzmann sum:

$$x_{Li}(\mu_{Li}) = \frac{1}{N}\frac{\sum_{\{\boldsymbol{\sigma}\}} N_{Li}(\boldsymbol{\sigma}) \exp\left(-\beta\left(E(\boldsymbol{\sigma}) - \mu_{Li}N_{Li}(\boldsymbol{\sigma})\right)\right)}{\sum_{\{\boldsymbol{\sigma}\}} \exp\left(-\beta\left(E(\boldsymbol{\sigma}) - \mu_{Li}N_{Li}(\boldsymbol{\sigma})\right)\right)} \tag{23}$$

The sums in the numerator and the denominator are performed over all possible Li-vacancy

configurations $\boldsymbol{\sigma}$ in the grand canonical ensemble (with the metal framework being otherwise fixed). $N_{Li}(\boldsymbol{\sigma})$ is the number of Li in a given configuration $\boldsymbol{\sigma}$ and $\beta = \frac{1}{kT}$, where k is the Boltzmann constant and T is the absolute temperature in Kelvin.

The Metropolis algorithm[67] is used to numerically solve equation (23). The Metropolis algorithm performs importance sampling, which consists in sampling configurations according to their equilibrium Boltzmann probability:

$$P_{equilibrium}(\boldsymbol{\sigma},T,\mu) = \frac{\exp\left(-\beta\left(E(\boldsymbol{\sigma}) - \mu_{Li}N_{Li}(\boldsymbol{\sigma})\right)\right)}{\sum_{\{\boldsymbol{\sigma}'\}} \exp\left(-\beta\left(E(\boldsymbol{\sigma}') - \mu_{Li}N_{Li}(\boldsymbol{\sigma}')\right)\right)} \tag{24}$$

Importance sampling is achieved asymptotically via a Markov chain construction. Starting from an initial state $\boldsymbol{\sigma}^0$, a Markov chain of configurations $\boldsymbol{\sigma}^n$ is generated. The probabilistic criterion used to generate $\boldsymbol{\sigma}^{n+1}$ from the previous configuration in the chain, $\boldsymbol{\sigma}^n$, is chosen such that the probability to sample a given configuration eonverges to the Boltzmann probability in the limit of large n. This property is expressed in equation (25):

$$\begin{aligned} &\boldsymbol{\sigma}^0 \rightarrow \boldsymbol{\sigma}^1 \rightarrow (...) \rightarrow \boldsymbol{\sigma}^n \rightarrow (...) \rightarrow \boldsymbol{\sigma}^M \\ &P_{Metropolis}\left(\boldsymbol{\sigma}^n\right) \underset{n\rightarrow\infty}{\rightarrow} P_{equilibrium}\left(\boldsymbol{\sigma}^n, T, \mu\right) \end{aligned} \tag{25}$$

The Metropolis algorithm can be summarized the following way. In a periodic supercell

containing N Li/Va sites with an initial Li-Va configuration $\boldsymbol{\sigma}^0$:

(1) Randomly sample a site i in the lattice

•Change the occupation value σ_i for that site

•If the change in σ_i decreases the grand potential $(E-\mu N)$ of the configuration, the change is accepted. Otherwise, accept the change with a probability $\exp\left(-\beta\left(\left(E_{final}-E_{initial}\right)-\left(N_{final}-N_{initial}\right)\mu_{Li}\right)\right)$

(2) Repeat step (1) N times to obtain the next configuration of the Markov chain ($\boldsymbol{\sigma}^1$).

(3) Repeat the process M times, to obtain a Markov chain of length M

It can be shown that the Metropolis asymptotically achieves Boltzmann importance sampling as expressed in equation (25).[67] Importance sampling allows equation (24) to be numerically evaluated using an arithmetic average over the sampled configurations in the Markov chain:

$$\langle x_{Li}\rangle(\mu_{Li},T)\approx\frac{1}{(M-m)}\sum_{i=m}^{M}\frac{N_{Li}(\boldsymbol{\sigma})}{N} \tag{26}$$

Where the number m represents the number of configurations that are discarded in the statistics, to account for the fact that convergence towards Boltzmann sampling is an asymptotic property of the Markov chain. Parameters of a Monte Carlo simulation include the number of Li/Va sites N, the number of discarded sampled configurations m and the total

number of configurations *M*. In this thesis, it is found that *m=10,000* and *M=50,000* with supercells containing 16x16x16 repetitions of the rocksalt primitive cell are sufficient to ensure convergence.

2.4 Special Quasi-Random Structures (SQS)

Special Quasi-random structures (SQS) are small periodic structures whose cluster correlations ($\bar{\phi}_{\alpha}^{\{s\}}$ in equation (17)) approach those of a fully random structure.[68] SQS's are useful tools to estimate the statistically expected energy (hereinto referred to simply as "energy") of a fully random structure and can be used in lieu of cluster expansions for that specific purpose. SQS's have the advantage of requiring a single DFT energy evaluation to predict the energy of a fully disordered structure, as opposed to a full cluster expansion fit. Furthermore, once an SQS is generated for a certain stoichiometry on a certain lattice (e.g. rocksalt $LiMO_2$), it can be used for any chemical species (e.g. any rocksalt ABO_2). In this thesis, we use SQS's to validate the predictions made by cluster expansions on the energy of fully random systems.

The principle behind SQS's can be inferred from the expression of a full (in other words exact) cluster expansion, which is expressed in equation (17) and repeated below for convenience.

$$E(\boldsymbol{\sigma}) = \sum_{\alpha} \sum_{\{s\}} m_{\alpha} J_{\alpha}^{\{s\}} \bar{\phi}_{\alpha}^{\{s\}}(\boldsymbol{\sigma})$$

Cluster expansions can in principle be a perfect representation of the configuration-dependence

of a supercell containing N sites if all clusters up to the N-tuplets are considered. A DFT calculation on a specific configuration can therefore be considered as an "exact" cluster expansion calculation on a specific configuration.

The statistically expected energy $\langle E \rangle$ of a system is given by a Boltzmann sum over configurations at a given temperature. Given the form of equation (17), this reduces to a Boltzmann sum over the cluster correlations :

$$\langle E \rangle = \sum_{\alpha} \sum_{\{s\}} m_{\alpha} J_{\alpha}^{\{s\}} \left\langle \bar{\phi}_{\alpha}^{\{s\}} \right\rangle$$

$$\left(\langle f \rangle = \sum_{\{\boldsymbol{\sigma}\}} f(\boldsymbol{\sigma}) P_{Boltzmann}(\sigma) \right) \tag{27}$$

The principle behind SQS's is that the expectation value of the correlations in a random structure are known *a priori*. In a fully random structure, the probability that a given site be occupied by atoms of a certain species is simply given by the global concentration of that species (this corresponds to the infinite temperature limit of equation (27)). As a result, the cluster correlations in equation (27) are simply given by:

$$\left\langle \phi_{\alpha}^{s}(\boldsymbol{\sigma}) \right\rangle = \prod_{i \in \alpha} \theta_{s_i}(\bar{\sigma}_i) \tag{28}$$

Where $\bar{\sigma}_i$ is the expected value of the occupation of site i based on the global concentration of each species on the lattice. For example, in a fully disordered binary AB system (fully cation-

disordered Li_xMO_2 system at $x_{Li}=0$ and 1 is an example of such a system), the average site occupancy is simply zero (σ_i can take -1 and 1 values with equal probability). Referring to equation (18), the energy of a fully disordered AB system therefore reduces to:

$$E(\boldsymbol{\sigma}) = J_0 \tag{29}$$

An SQS for an *AB* system on a given lattice is therefore a specific periodic structure on that lattice containing a large number of zero correlations. In the general case, an SQS is a small periodic structure whose cluster correlations approach that of a random structure for a large number of clusters (with priority igiven to the short range clusters, whose contribution to the Hamiltonian is larger). Several SQS's have been developed in the literature for binary and ternary FCC systems with various stoichiometries.[68,69] In this thesis, we use the SQS-16 developed by Zunger et al[68] to calculate the average energy of fully cation-disordered $LiMO_2$. This SQS contains 16 cation sites and its correlations are identical to that of a fully disordered $LiMO_2$ system for the first eight pairs and the first eight triplets.

2.5 Thermodynamics of phase-separating systems

Phase-separating systems are defined as systems whose thermodynamic ground state, in the incoherent limit, is a coexistence of two distinct phases. In Li_xA systems, where A is the host structure for Li intercalation, two-phase coexistence over a concentration range $[x_1,x_2]$ occurs if the formation free energy is concave between x_1 and x_2. An important phase separating system in Li-ion battery is the Li_xFePO_4 system. Partially lithiated Li_xFePO_4 phase separates into a

stoichiometric mix $FePO_4$ and $LiFePO_4$ phases ($LixFePO_4$ ➔ $xLiFePO_4 + (1-x)FePO_4$) , with negligible solubility in its end members. The bulk free energy for Li intercalation in Li_xFePO_4 is schematically illustrated in **Figure 2-1**(a).

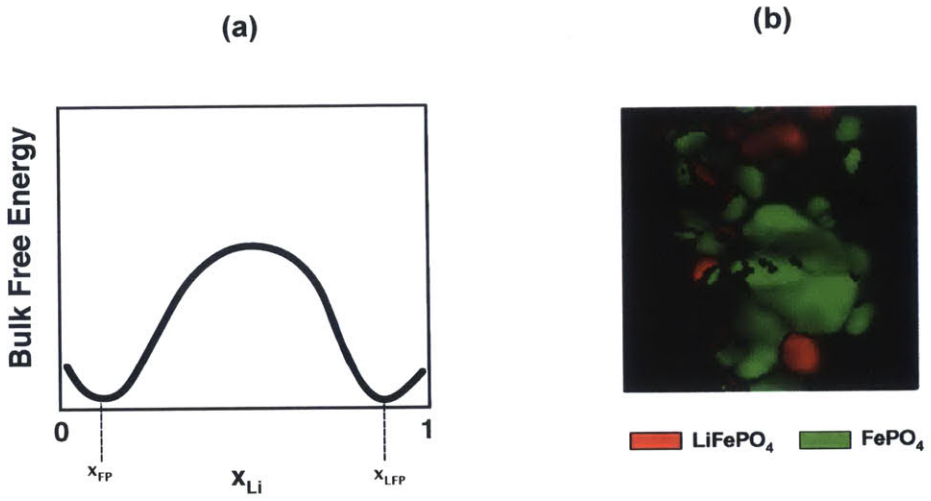

Figure 2-1 **(a)** Bulk free energy in an Li_xFePO_4 single particle **(b)** Multi-particle equilibrium, where some particles are fully lithiated and others are fully delithiated[70]

Practical $LiFePO_4$ electrodes contain a large number of particles. At the electrode level, the thermodynamic equilibrium state is the incoherent equilibrium, where some particles are fully lithiated ($LiFePO_4$) and some are fully delithiated ($FePO_4$) (**Figure 2-1**(b)). Accessing this electrode-level equilibrium state is possible via Li-redistribution between particles. The free energy of the electrode in that case is simply a weighted sum of the bulk free energy of the $FePO_4$ and the $LiFePO_4$ phases (as no phase coexistence exists within a single particle).

During charge/discharge, each particle must however intake Li from the counter-electrode. During the (de)lithiation process, actively transforming particles therefore exist in a state of

intermediate Li concentration. In this thesis, the lithiation mechanism of $LiFePO_4$ is investigated, and the persistence of intermediate solid solution states in $LiFePO_4$ electrodes at low-to-moderate C-rates in $LiFePO_4$ is explained. We demonstrate that the persistence of large intermediate solid solution regions at $LiFePO_4/FePO_4$ interfaces is largely a volumetric effect dictated by the relative ratio of the solid solution free energy and the coherency strain energy at a sharp coherent interface. In the rest of this section, we focus our attention on how the (bulk) free energy in the particle resulting from the presence of a sharp or a diffuse interface can be calculated by a combination of first principles calculations and continuum elasticity.

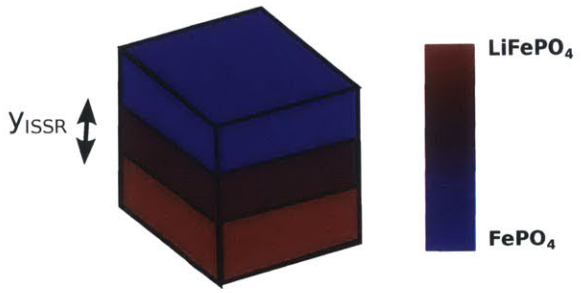

Figure 2-2 Equilibrium state in a partially lithiated single Li_xFePO_4 particle. The particle contains an $FePO_4$ region, an $LiFePO_4$ region and potentially an intermediate solid solution region (ISSR) with volume fraction y_{ISSR}.

The bulk free energy penalty for phase-separation associated with a sharp coherent interface ($y_{ISSR}=0$ in **Figure 2-2**), with respect to the incoherent equilibrium, is given by:

$$F_{sharp\ boundary} = Ve_{strain}^{sharp\ boundary} + A\gamma \tag{30}$$

Where V is the particle volume, $e_{\text{strain}}^{\text{sharp boundary}}$ is the volume-averaged coherency strain energy density in the particle (resulting from a sharp interface), A is the interfacial area and γ is the chemical interfacial energy. More precisely, the quantity e_{strain} is equal to the total strain energy in the particle divided by the total volume of the particle, as expressed in equation (31).

$$e_{strain} = \frac{1}{V_{particle}} \int_{V_{particle}} \frac{1}{2} \sigma_{ij} \varepsilon_{ij}^{elastic} \, dV \tag{31}$$

In equation (31), σ_{ij} is the stress tensor, $\varepsilon_{ij}^{elastic}$ is the elastic strain tensor, defined as the difference between the total strain tensor and the stress-free strain tensor (see the end of this section for more details). The free energy penalty for the creation of a diffuse interface is the sum of the bulk free energy of the intermediate solid solution region (ISSR), the coherency strain energy resulting from the presence of a diffuse interface and the gradient energy penalty in the ISSR (**Figure 2-2**):

$$F_{diffuse\ boundary} = V y_{ISSR} \bar{f}_{solid-solution} + V e_{strain}^{diffuse\ boundary} + \int_{V_{ISS}} k \left| \nabla x_{Li} \right|^2 dV \tag{32}$$

where y_{ISSR} is the volume fraction of the ISSR, $\bar{f}_{solid-solution}$ is the volume-averaged bulk free energy density in the ISSR, $e_{strain}^{diffuse\ boundary}$ is the volume-averaged coherency strain energy density in the particle resulting from a diffuse boundary, κ is the gradient energy coefficient

and ∇x_{Li} is the concentration gradient in the ISSR. Comparing the bulk free energy penalty of sharp and diffuse interfaces therefore requires calculating coherency strain energy, chemical interfacial energies and gradient energy penalties for various particle sizes and morphologies.

In this thesis, coherency strain energies are calculated by numerically solving the equations linear elasticity. The nomenclature used in linear elasticity is noted in Table 2-1, while the equations of linear elasticity are provided in equations (33) to (37) (in cartesian coordinates). The corresponding boundary and continuity conditions are expressed in equations (38) and (39).

Table 2-1 Definition of variables used to calculate coherency strain energy

Stress tensor	Displacement vector	Total strain tensor
σ_{ij}	$\underline{u}$	ε_{ij}^{total}
Elastic strain tensor	Vegard coefficients tensor	Stiffness tensor
$\varepsilon_{ij}^{elastic}$	ε_{ij}^{0}	C_{ijkl}

Table 2-2. Equations of Linear Elasticity

Mechanical equilibrium	$\frac{\partial \sigma_{ij}}{\partial x_j} = 0$	(33)
Strain compatibility	$\varepsilon_{ij}^{total} = \frac{1}{2}\left(\frac{\partial u_i}{\partial x_j} + \frac{\partial u_j}{\partial x_i}\right)$	(34)

Elastic strain	$\varepsilon_{ij}^{elastic} = \varepsilon_{ij}^{total} - x_{Li}\varepsilon_{ij}^{0}$	(35)
Linear stress-strain relation	$\sigma_{ij} = C_{ijkl}\varepsilon_{kl}^{elastic}$	(36)
Concentration-dependent stiffness tensor (linear approximation)	$C_{ijkl}(x_{Li}) = C_{ijkl}^{FePO_4} + x_{Li}\left(C_{ijkl}^{LiFePO_4} - C_{ijkl}^{FePO_4}\right)$	(37)

Table 2-3. Boundary and continuity conditions

Traction free condition on the particle surface	$\sigma_{ij} \cdot n_j\big\|_{External\ surface} = \underline{0}$	(38)
Coherency condition at the $FePO_4$/$LiFePO_4$ interface (sharp interface)	$\underline{u}$ is continuous across the interface	(39)

Equation (33) ensures that the system is at equilibrium, equation (34) links the total strain tensor with the displacement field, equation (35) defines the elastic strain tensor as the difference between the total strain tensor and the natural strain induced by variation in lithium concentration, equation (36) expresses the linear relation between stress and elastic strain through the stiffness tensor and equation (37) expresses the concentration-dependence of the stiffness tensor. The traction-free boundary condition in equation (38) expresses the fact that no external traction is applied on the particle surface, while the continuity condition in equation (39) ensures that the interface between the lithium-poor and lithium rich phases is coherent (used in the case of sharp interfaces).

It is to be noted that, due to the form of the equations (33)-(39), the volume-averaged coherency strain energy density as defined in equation (31) is identical for two systems that can be obtained from one another via a single scaling factor. The volume-averaged coherency strain energy density associated with a sharp interface, for example, depends only on the lithium concentration x_{Li}, the interface orientation and the particle morphology, but not on the particle volume (at a given particle morphology). In other words, the total coherency strain energy E_{strain} for a sharp interface can be written as:

$$E_{strain} = V_{particle} \bullet e_{strain}\left(x_{Li}, \text{interface orientation, particle morphology}\right) \quad (40)$$

A similar scaling law applies to particles containing an ISSR. In this thesis, the equations of continuum elasticity are solved numerically. These equations are cast into the smoothed boundary method as formulated by Yu *et al.*[71] to solve for the elastic stress tensor and strain tensor using the alternative direction iterative (ADI) method in a second-order central-difference scheme in space. Values of the elastic constants for the $LiFePO_4$ and $FePO_4$ phases and values of the Vegard coefficients are taken from the first principles evaluations of Maxisch et al [72].

Chemical interfacial energies per unit area are calculated using the Generalized Gradient Approximation (GGA+U) to Density Functional theory (DFT) as implemented in the Vienna Ab Initio Simulation Package, with a self-consistent U value for Fe of 4.3 as previously determined by Zhou et al.[62] Energies of supercells containing pure $LiFePO_4$, pure $FePO_4$ and an $LiFePO_4/FePO_4$ interface are calculated and their difference is divided by the area of the

$LiFePO_4/FePO_4$ interface to obtain the chemical interfacial energy per unit area. This standard procedure is illustrated in equation (41). (Note that, in equation (41), the two-phase supercell contains an equal fraction of each phase.)

$$\gamma_{coherent} = \lim_{N\to\infty} \frac{\left[E^{2-phase}_{N\ unit\ cells} - \frac{N}{2}E^{FePO_4} - \frac{N}{2}E^{LiFePO_4}\right]_{\text{Fixed lattice parameters along the interface plane}}}{2A_{\text{interface}}} \quad (41)$$

Energy calculations of the fully lithiated, fully delithated, and two-phase states are performed at the same lattice parameters along the plane of the interface, while the dimension perpendicular to the interface is allowed to relax. This standard procedure is essential to capture only the chemical interfacial energy component of the energy penalty for phase-separation, without any contribution from the coherency strain energy. In general, the exact values of the lattice parameters along the interface depend on the relative phase fraction of the $FePO_4$ and $LiFePO_4$ phases. Since it was found that the calculated chemical interfacial energy per unit area has a weak dependence on the choice of these lattice parameters (e.g. $\pm$ 0.5 mJ/m^2 for the *ac* interface), only the average values obtained at the $FePO_4$ and $LiFePO_4$ lattice parameters is reported. Using the linear interpolation method of Fiorentini and Methfessel,[73,74] γ values were found to converge at a supercell size consisting of three unit cells of each phase ($N=6$ in equation (41)). All the calculation parameters stated above ensure that the reported γ values are converged to within 1 mJ/m^2.

Note that other surface-scaling effects such as the surface energy differences between a sharp interface and a diffuse interface are ignored. This approximation is justified *a posteriori* given that the identified mechanism for the retention of intermediate solid solutions is a volumetric effect and that is it observed at particle sizes where surface effects are small (~200 nm[52]).

Chapter 3

The effect of cation disorder on the average Li intercalation voltage of transition metal oxides

3.1 Introduction

Cation disorder is a phenomenon that is becoming increasingly important in the field of Li-ion batteries. As-synthesized disordered Li-excess rocksalts ($Li_{1+x}Nb_yM_zO_2$ [M=Mn, Fe, Co, Ni], [1,8,19] $Li_{1.2}Ni_{0.33}Ti_{0.33}Mo_{0.14}O_2$,[17] $Li_{1+x}Ti_{2x}Fe_{1-3x}O_2$ [20]) were recently shown to achieve high reversible capacity, paving the way towards a new design space of high-capacity Li-ion battery cathodes. These high capacities are enabled by macroscopic Li transport through percolating zero-transition-metal pathways, which remain active upon disorder.[15,75] *In situ* cation disorder also occurs in a large class of ordered materials, resulting in the formation of disordered bulk phases ($Li_{1.211}Mo_{0.467}Cr_{0.3}O_2$,[15] Li_2VO_3,[16] $LiCrO_2$,[14,76] $Li_{0.96}VO_2$,[77] rutile TiO_2 [78,79]). Furthermore, *in situ* cation disorder can also occur at the surface of ordered compounds as a result of oxygen loss and transition metal migration, such as is the case for the NCA ($LiNi_{0.8}Co_{0.2}Al_{0.05}O_2$)[29] and Li-excess NMC ($Li_{1+y}Ni_wCo_zMn_{2-y-w-z}O_2$) compounds.[23,27,28]

Cation disorder can have a strong impact on the lithium intercalation voltage of transition metal oxides, as is evidenced by the change in voltage profiles in materials that undergo *in situ* disorder.[15,16,78] Surface disorder can also significantly affect the measured voltage if surface transport properties are poor. Disordered surfaces with an increased TM/Li ratio[27] are likely to exhibit poor transport properties, as Li-excess is required to sustain macroscopic diffusion in disordered materials.[10] As a result, the measured voltage profile in the particle may be greatly influenced by the redox processes occurring in the disordered surface region, where Li insertion/extraction occurs.

Understanding the effect of cation disorder on the voltage profile of transition metal oxides is therefore critical, both to rationally design high-capacity disordered Li-excess rocksalts as well as to predict the voltage evolution of ordered materials subject to *in situ* bulk or surface cation disorder. Despite the growing importance of cation disorder in the Li-ion battery field, however, little work has been done on quantitatively understanding its effect on the Li-intercalation voltage of transition-metal oxides. To our knowledge, the only work on this topic was conducted by Saubanere et al.[21] Using a simplified voltage model based on chemically intuitive quantities, the authors argued that the average voltage of $LiMO_2$ cation-disordered rocksalts must be higher than their ordered homologues.

In general, cation disorder can have two important effects on the Li-intercalation voltage profile of transition metal oxides : (i) a change in the average voltage, and (ii) an increase in the slope of the voltage profile. The average voltage controls the total energy deliverable from the electrochemical reaction, while the slope of the voltage profile determines the fraction of capacity accessible in a certain voltage window. In this Chapter, we use first principles methods to understand and quantify the effect of cation disorder on the average Li-insertion

voltage of transition metal oxides.

In order to isolate the effect of cation disorder from other parameters such as the Li/TM ratio (in other words the Li-excess or Li-deficiency level), we consider the average voltage of *stoichiometric* transition metal oxides. The effect of cation disorder on transition metals undergoing a $3^+/4^+$ redox reaction is investigated through a systematic study of first-row $LiMO_2$ compounds (M=Ti, V, Cr, Mn, Fe, Co, Ni). Among these compounds, $LiTiO_2$ and $LiFeO_2$, disorder at solid-state synthesis temperature,[80] while $LiVO_2$ [77] and $LiCrO_2$ [14,76] can disorder upon cycling at room temperature. Mn, Co and Ni, although not found to disorder in the stoichiometric $LiMO_2$ form (with the exception of high-energy ball-milling[81]), disorder as part of mixed transition metal compounds ($LiM_{0.5}Ti_{0.5}O_2$ compounds, where M=Mn, Fe, Co, Ni)[82-85] and can also form disordered surface layers upon cycling in mixed-transition metal environment such as NCA[22] and Li-excess NMC.[23,27]

In summary, this study aims at providing a quantitative examination of the effect of cation disorder on the $3^+/4^+$ redox couple of stoichiometric lithium transition metal oxides, and thereby also provide insights on the effect of cation disorder on the building blocks of more complex bulk or surface cation-disordered systems.

3.2 Methodology

Ordered and disordered states of a lithium transition-metal oxide are schematically illustrated in **Figure 3-1**(a) and are based on the rocksalt framework, consisting of interpenetrating cation (Li and M) and anion (O) FCC sublattices. In the cation sublattice, Li and transition metals are

octahedrally coordinated by oxygen (LiO_6 and MO_6 octahedra). In an ordered state, Li and M atoms occupy distinct periodic sublattices of the FCC rocksalt cation framework (**Figure 3-1**(a)-(i)). Examples of experimentally observed ordered $LiMO_2$ structures include the layered, overlithiated spinel, γ-$LiFeO_2$ and orthorombic structures.[80] In the fully disordered state, Li and TM atoms randomly occupy sites of the FCC rocksalt cation framework (**Figure 5-1**(a)-(ii)). Note that cation-disordered structures need not be fully random, but can in fact exhibit short-range order.[82] In this Chapter, we only consider the limit of fully disordered lithium transition metal oxides.

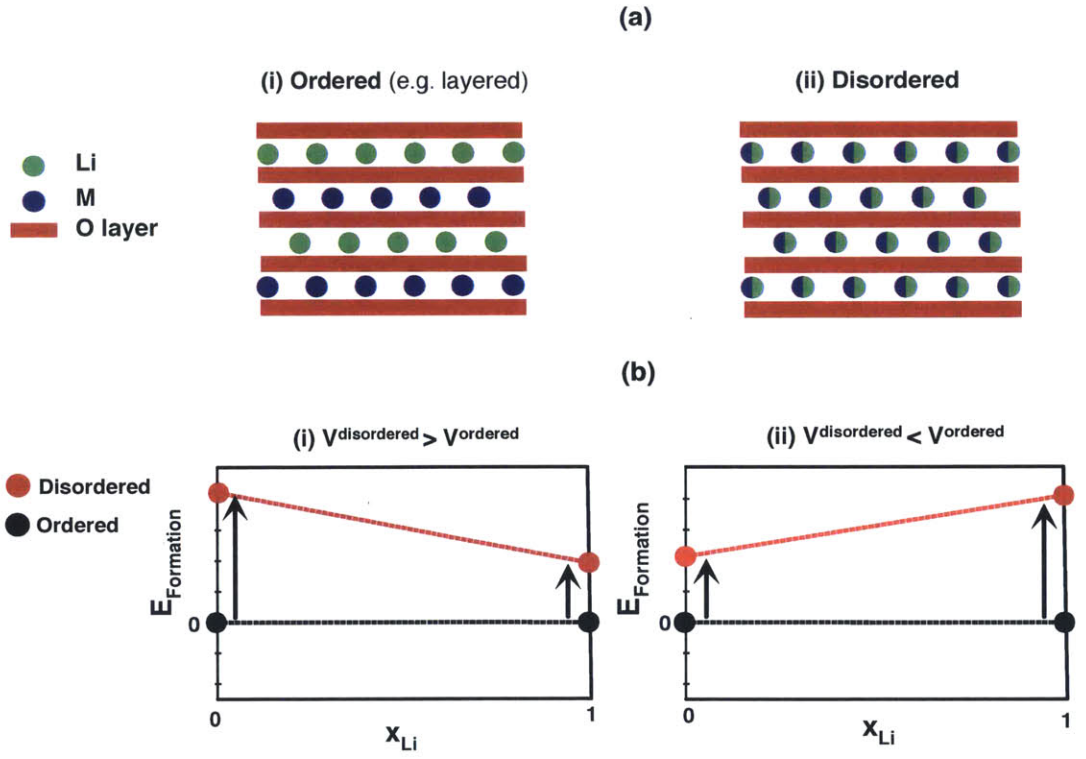

Figure 3-1: **(a)** Cation arrangement in ordered (left; the layered structure is shown as an example) and disordered (right) structures. The layers displayed in the figure are the (111) planes of the FCC cation sublattice. **(b)** The voltage of the disordered structure is larger than the voltage of the ordered structure if the disordering energy is larger in the delithiated limit

than in the lithiated limit $\left(\underline{E}^{dis}_{MO_2} - \underline{E}^{ord}_{MO_2}\right) > \left(\underline{E}^{dis}_{LiMO_2} - \underline{E}^{ord}_{LiMO_2}\right)$ **(i)**. Conversely, the voltage of the disordered structure is smaller than the voltage of the ordered structure if the disordering energy is smaller in the delithiated limit than in the lithiated limit $\left(\underline{E}^{dis}_{MO_2} - \underline{E}^{ord}_{MO_2}\right) < \left(\underline{E}^{dis}_{LiMO_2} - \underline{E}^{ord}_{LiMO_2}\right)$ **(ii)**.

The average voltage resulting from the intercalation of one formula unit of Li in a stoichiometric MO_2 compound, with respect to metallic Li, is given by equation (42). [86] This relation is general and is valid both for ordered and disordered structures.

$$e\overline{\Delta V} = -\left(\underline{G}_{LiMO_2} - \underline{G}_{MO_2} - \underline{G}_{\text{Li metal}}\right) \tag{42}$$

In equation (42), $\overline{\Delta V}$ is the average (open circuit) voltage and $\underline{G}_{\text{LiMO}_2}$, $\underline{G}_{\text{MO}_2}$, $\underline{G}_{\text{Li metal}}$ are the free energy of the lithiated transition metal oxide, delithiated transition metal oxide and metallic lithium compounds, expressed in eV per formula unit. The difference between the disordered and ordered average voltage is obtained by expressing equation (42) for ordered and disordered structures and taking the difference between the two expressions. The result is given in equation (43):

$$e\left(\overline{\Delta V}_{dis} - \overline{\Delta V}_{ord}\right) = \left(\underline{G}^{dis}_{MO_2} - \underline{G}^{ord}_{MO_2}\right) - \left(\underline{G}^{dis}_{LiMO_2} - \underline{G}^{ord}_{LiMO_2}\right) \tag{43}$$

Equation (43) can be simplified further by neglecting the configurational entropy of ordered structures and by noting that the configurational entropy of a fully random system is the same in the lithiated and delithiated limits ($S = -k\sum_i x_i \ln(x_i)$). As a result, the difference in average

voltage between the disordered and ordered structure depends only on the relative energy of the two structures:

$$e\left(\overline{\Delta V}_{dis} - \overline{\Delta V}_{ord}\right) = \Delta \underline{E}^{dis}_{MO_2} - \Delta \underline{E}^{dis}_{LiMO_2} \quad (44)$$

With: $\Delta \underline{E}^{dis}_{Li_xMO_2} = \underline{E}^{dis}_{Li_xMO_2} - \underline{E}^{ord}_{Li_xMO_2}$

Note that, in equation (44), we define the "disordering energy", $\Delta \underline{E}^{dis}_{Li_xMO_2}$, as the energy difference between the fully disordered structure and the ordered structure at a given Li concentration.

The voltage change upon disorder is controlled by the relative disordering energy in the lithiated and delithiated limits (**Figure 5-1**(b)). If the disordering energy is larger in the delithiated limit than in the lithiated limit $\left(\Delta \underline{E}^{dis}_{MO_2} > \Delta \underline{E}^{dis}_{LiMO_2}\right)$, the voltage of the disordered structure is higher than the voltage of the ordered structure (**Figure 5-1**(b)-(i)). Conversely, if the disordering energy is smaller in the delithiated limit than in the lithiated limit $\left(\Delta \underline{E}^{dis}_{MO_2} < \Delta \underline{E}^{dis}_{LiMO_2}\right)$, the voltage of the disordered structure is smaller than the voltage of the ordered structure (**Figure 5-1**(b)-(ii)).

In this Chapter, we compare the voltage of fully disordered $LiMO_2$ with the voltage of the $LiMO_2$ ordered ground-state structure for first-row $LiMO_2$ compounds (M=Ti, V, Cr, Mn, Fe, Co, Ni). The lithiated ground-state structure is calculated to the layered structure for $Li(Co,Ni,V,Cr)O_2$, the γ-$LiFeO_2$ structure for $Li(Fe,Ti)O_2$ and the orthorhombic structure for $LiMnO_2$. These ground-state structures are all validated by experimental results,[80] with the

exception of $LiTiO_2$, which cannot be synthesized in its ground-state structure as it disorders at normal solid-state synthesis temperatures.[80] Note that, in the case of $LiTiO_2$, the γ-$LiFeO_2$ structure is equivalent to the lithiated anatase structure.

The energy of ordered ground-state structures are calculated within the Hubbard-U corrected Generalized Gradient Approximation (GGA+U) to Density Functional Theory (DFT), using the PBE exchange-correlation functional[58,87], as implemented in the Vianna Ab Initio Simulation Package (VASP). The U parameters are extracted from the work of Jain et al.[61] (Detailed calculations parameters are given in section 2.1 of Chapter 2). A large number of spin-orderings are considered, among which the spin ordering with the lowest energy is selected.

The energy of the cation-disordered structure is calculated using the cluster expansion technique, which parametrizes the energy of any cation arrangement using a finite number of Effective Cluster Interactions (ECI's). Two cluster expansions are fitted: one in the lithiated limit and another in the delithiated limit. The ECI's, encompassing the zero order, point, pair, triplet and quadruplet interactions, are fitted on the DFT energies of all cation-mixed structures with unit cells containing up to four formula units of $LiMO_2$ (and therefore eight cations). This subset of 121 symmetrically distinct structures includes all experimentally observed structures in the $LiMO_2$ rocksalt lattice, including the layered, γ-$LiFeO_2$, orthorombic and overlithiated spinel structure. Only structures that map onto the FCC rocksalt lattice, where both Li/Va and M atoms are octahedrally coordinated by oxygen, are conserved in the fit (structures where transition metals migrate to tetrahedral sites are not included). Structures where O-O bonds form are also disregarded, as GGA+U is known to overstabilize O-O bonding. The CE is fitted using the compressive sensing paradigm and optimized through the split-Bregman algorithm.[66] Using the fitted cluster expansion, the energy of the cation-disordered structure is calculated by

evaluating the energy of randomly populated 30x30x30 supercells, such that the energy of the disordered structure is converged to within 0.005V. These energy calculations were performed using the Cluster Assisted Statistical Mechanics (CASM) software.[88]

The root mean square error (RMSE) and the cross-validation (CV) score are used to judge the quality and the predictive ability of the fit, respectively. Since disordered energies are an average quantity over a large number of local configurations, and therefore prone to error cancellation, the error bars on the disordered energies are in fact smaller than the CV score. The error bar on the disordered average voltage is approximated by fitting several cluster expansions for each system. In practice, an error bar of ±50mV is found to be a conservative estimate for all transition metal oxides studied in this Chapter. (Limiting the cluster expansions to only the first 5 neighboring pair interactions, for example, gives average voltage predictions within the predicted error bar.) The CV scores are found to be on average 50 meV/f.u. in the $LiMO_2$ limit and 80 meV/f.u. in the MO_2 limit. Note that the energy difference between the lowest energy and highest energy structure at a given Li concentration is large (~1500 meV/f.u. in the $LiMO_2$ limit and ~2300 meV/f.u. in the MO_2 limit, on average over all transition metals).

We find that our predictions are in good agreement with calculations of disordering energies using special quasi-random structures (SQS). The SQS-16 developed by Zunger et al[68] predicts disordering energies that are consistent with our cluster expansion predictions to within ~30 meV/f.u. in the $LiMO_2$ limit. This SQS contains 16 cationic sites and its correlations are identical to that of a fully disordered $LiMO_2$ system for the first eight pairs and the first eight triplets.

3.3 Results

Figure 3-2(a) shows the disordering energy in the lithiated and delithiated limits for first-row $LiMO_2$ compounds (M=Ti, V, Cr, Mn, Fe, Co, Ni). In the Discussion section of this Chapter, we explain how experimental observations and electronic structure trends explain the position of most disordering energies calculated in **Figure 3-2**(a).

These disordering energies can be used to calculate the voltage difference between disordered and ordered structures via equation (44). The results are illustrated in **Figure 3-2**(b). Cation disorder increases the voltage of transition metals that have a higher disordering energy in the delithiated limit (Ti,Mn,Fe,Co,Ni), while it decreases the voltage of transition metals that have a higher disordering energy in the lithiated limit (V, Cr). The difference between the disordered voltage and the ordered ground-state voltage varies between extremal values of ~ -0.3V (for $LiCrO_2$) and ~0.6V (for $LiTiO_2$ and $LiNiO_2$).

Figure 3-2(c), shows the absolute average voltage values of the disordered and lithiated ground-state structures (see also **Table 3-1**). Both sets of voltages follow the known trend that transition metals with higher atomic number display larger voltages, due to the lower energy of the 3d transition metal band as the atomic number of the transition metal increases.[86] The $LiMO_2$ transition-metal oxide compound with the highest disordered average voltage is predicted to be $LiNiO_2$ at ~4.4V (compared to ~3.9V for the layered structure).

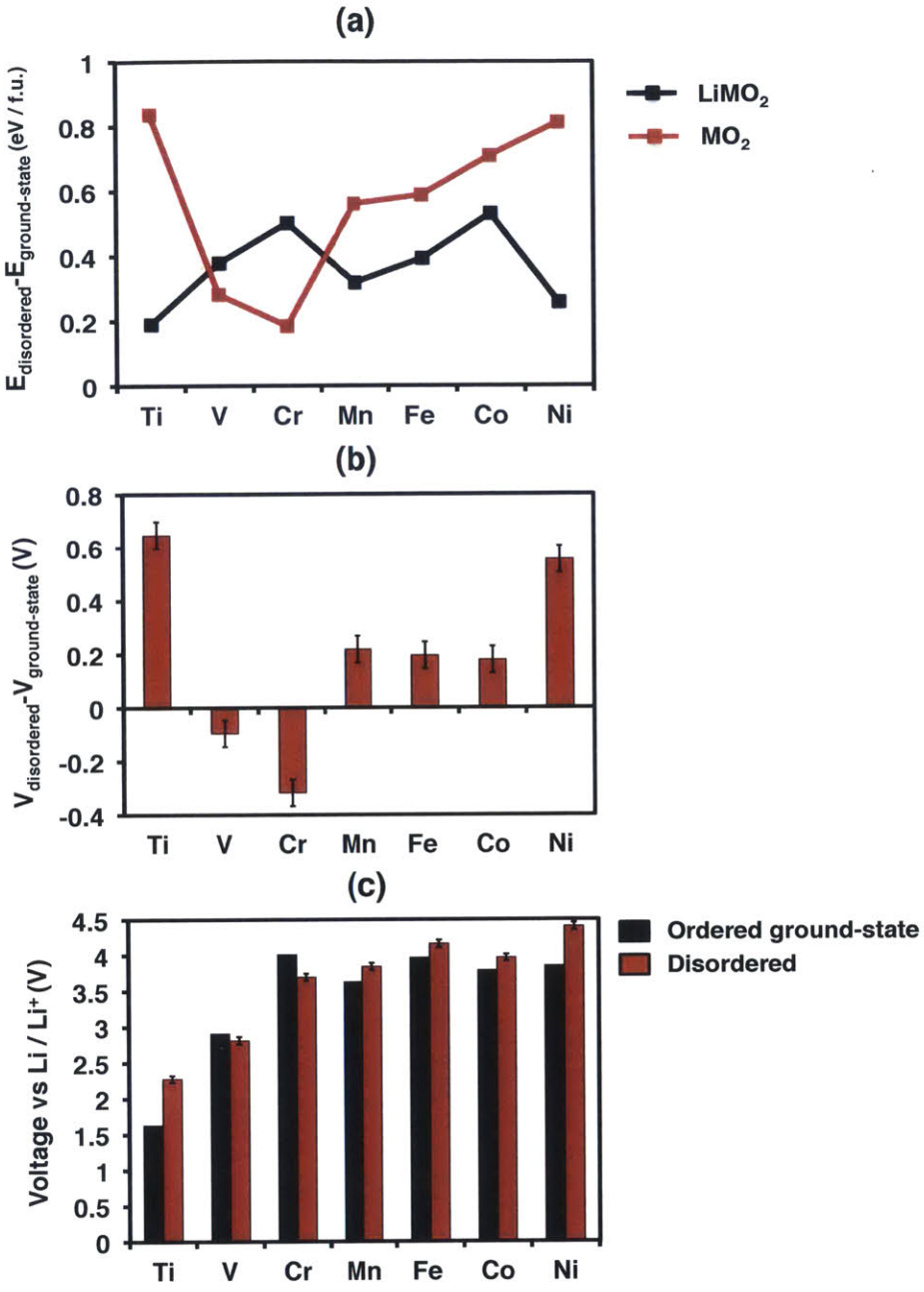

Figure 3-2: **(a)** Disordering energy (with respect to the $LiMO_2$ ground-state structure) for different transition metals, in the $LiMO_2$ and MO_2 limits. **(b)** Voltage difference between disordered $LiMO_2$ and the $LiMO_2$ ordered ground-state **(c)** Absolute average voltage for fully disordered and ground-state $LiMO_2$ structures.

Table 3-1 : Calculated Average voltage of fully disordered $LiMO_2$ (all reported values have an uncertainty of ±0.05V)

Ti	V	Cr	Mn	Fe	Co	Ni
2.25 V	2.80 V	3.70V	3.85 V	4.15 V	3.95 V	4.40 V

Direct comparison of the predicted disordered voltages with experimental results is difficult, as disordered $LiMO_2$ structures cannot be electrochemically cycled given their poor Li diffusivities (Li-excess is required to enable macroscopic diffusivity in cation-disordered rocksalts[15]). The only disordered material that has been partially cycled in the $LiMO_2$ family is disordered $LiTiO_2$, which is formed *in situ* upon lithium insertion in rutile TiO_2.[78,79] Particle nano-sizing allows for small diffusion lengths (as low as 10 nm[78,79]), which partially compensates for the poor diffusivity of Li in stoichiometric disordered $LiTiO_2$. After a first discharge, during which disordered $LiTiO_2$ is formed, the voltage profile changes and the average voltage upon cycling of 200 mAh/g ($LiTiO_2 \leftrightarrow Li_{0.4}TiO_2$) is found to be on the order of 1.8V.[78,79] This value is lower than the 2.25V value calculated in the present study. However, only 60% of the theoretical capacity can be accessed upon charge, indicating that the average voltage for full Li extraction is likely higher than the experimentally reported value. Furthermore, significant hysteresis is still present in the experimental charge-discharge profile curves even at low rates, rendering the extraction of the average open circuit voltage difficult. We further note that our 2.25V prediction is consistent with the experimentally observed 2.2V-2.3V plateau associated with $Ti^{3+/4+}$ redox in disordered $Li_{1+z/3}Ni_{1/2-z/2}Ti_{1/2+z/6}O_2$ [89] and $Li_{1.2}Ni_{0.33}Ti_{0.33}Mo_{0.14}O_2$.[17]

Our predictions of a high disordered $Ni^{3+/4+}$ voltage (~4.4V) are consistent with the observed

inaccessibility of the $Ni^{3+/4+}$ redox in the disordered Li-excess $Li_{1.2}Ni_{0.33}Ti_{0.33}Mo_{0.14}O_2$ compound.[17] While this disordered material shows very high reversible capacity, XANES analyses demonstrate that the transition metal redox activity is in fact limited to the $Ni^{2+/3+}$ redox couple, with the remainder of capacity attributed to reversible redox capacity from the $O^{2-/1-}$ redox couple.[17] The redox level of this $O^{2-/1-}$ couple, calculated at ~4.3V,[90] would therefore be accessible before the disordered $Ni^{3+/4+}$ couple, which is calculated in this work to be at ~4.4V.

To further corroborate the high voltage of the $Ni^{3+/4+}$ redox in the disordered form, we performed a cluster expansion fit of fully disordered $LiTi_{0.5}Ni_{0.5}O_2$, which is the material from which Li-excess $Li_{1.2}Ni_{0.33}Ti_{0.33}Mo_{0.14}O_2$ is derived. This compound can indeed be written as a solid solution between $LiNi_{0.5}Ti_{0.5}O_2$ and $Li_{1.6}Mo_{0.4}O_2$ ($Li_{1.2}Ni_{0.33}Ti_{0.33}Mo_{0.14}O_2 = \frac{2}{3}(LiNi_{0.5}Ti_{0.5}O_2) + \frac{1}{3}(Li_{1.6}Mo_{0.4}O_2)$). A ternary cluster expansion fit was performed over the input structure of all 469 periodic structures with periodicity up to 8 cations and performed both in the lithiated and delithiated limits. A similar accuracy of ±50 mV was obtained, as for the disordered $LiMO_2$ cluster expansions. Furthermore, the energy of fully disordered $LiNi_{0.5}Ti_{0.5}O_2$ agreed to within ~35 meV/f.u. with direct energy evaluation using the $LiA_{0.5}B_{0.5}O_2$ Special Quasi-Random Structure developed by Shin et al.[69]

Using this method, the average voltage for $Ni^{2+/4+}$ oxidation in fully disordered $LiNi_{0.5}Ti_{0.5}O_2$ was calculated to be (4.20±0.05)V. We find that this prediction is consistent with the 3.6V-4.8V voltage range obtained during charge profiles of disordered $LiNi_{0.5}Ti_{0.5}O_2$ between $x_{Li}=0.05$ and $x_{Li}=0.7$.[83] Note, however, that experimental voltages display significant hysteresis and are only available between $x_{Li}=0.05$ and $x_{Li}=0.7$, thus rendering extraction of the (open circuit)

average voltage difficult. Based on our theoretical predictions, the $Ni^{3+/4+}$ redox in $LiNi_{0.5}Ti_{0.5}O_2$ is therefore higher than 4.2V (which constitutes an average over the two-step $Ni^{2+/3+}$ and $Ni^{3+/4+}$ redox process), in general agreement with the 4.4V $Ni^{3+/4+}$ average voltage predicted for fully disordered $LiNiO_2$. We therefore speculate that the high voltage of disordered $Ni^{3+/4+}$ is a general feature in cation-disordered rocksalts.

3.4 Discussion

Experimental observations and electronic structure trends explain the position of most disordering energies calculated in **Figure 3-2**(a), as detailed in the following paragraphs.

We find that while most $LiMO_2$ compounds increase their average voltage upon disordering, when M=Cr or V the average voltage decreases with disorder (by 0.3V and 0.1V, respectively). Furthermore, in the MO_2 limit, the disordering energies of VO_2 and CrO_2 are found to be significantly lower than the disordering energy of other transition metals (~200-280 meV/f.u. compared to ~600 meV/f.u. and above for other transition metals), thus making these transition metal compounds more likely to disorder upon delithiation. This is in agreement with experimental observations, as layered $LiVO_2$ [77] and $LiCrO_2$ [14,76] are known to disorder *in situ* upon charge. Although 200 meV/f.u. is still too large to drive a transition to a fully random structure at room temperature (the entropy term $TS = -kT\ln(2)$ being only ~35 meV/f.u. for a fully random MO_2 system at room temperature), it is possible that these compounds only partially disorder upon cycling at room temperature, or that cation disorder occurs at intermediate Li compositions (the concavity of the disordered free energy curve being more pronounced than that of the ordered free energy curve due to the larger voltage slope).

On the $LiMO_2$ side, the disordering energy of lithiated $LiTiO_2$ is calculated to be the smallest among all first row transition metals. Consistent with this result, $LiTiO_2$ experimentally disorders at solid-state synthesis temperatures.[80]

The trend in the disordering energy of $LiMO_2$ (**Figure 3-2**(a)) is generally upward as the electron count on the transition metal increases, with only Mn and Ni modifying the upward trend. It is notable that both Mn and Ni are Jahn-Teller active in the 3^+ state.[91] Cation disorder creates local distortions in MO_6 octahedra, by virtue of the large variety of local environments around transition metal atoms. Because Mn^{3+} and Ni^{3+} are Jahn-Teller active, they can accommodate a certain degree of MO_6 distortion along the Jahn-Teller distortion mode.[91] This additional degree of freedom contributes in lowering the disordering energy of these compounds and therefore break the general upward trend.

Electronic structure arguments can also be used to justify points of high disordering energy in **Figure 3-2**(a). Transition metal ions with a low spin d^6 configuration (Co^{3+}, Ni^{4+}) or high spin d^3 electronic configuration (Cr^{3+}, Mn^{4+}) have filled or half-filled (resp. empty) t_{2g}(resp.e_g) bands, and consequently favor the highly symmetrical octahedral MO_6 environments found in ordered arrangements. The disordering energy for these compounds is therefore expected to be high, as cation disorder leads to distortions of the MO_6 octahedra. In agreement with this statement, $LiCrO_2$ (Cr^{3+}) and $LiCoO_2$ (Co^{3+}) are found to have the highest disordering energies among lithiated $LiMO_2$ compounds, and NiO_2 (Ni^{4+}) is found to have the highest disordering energy among delithiated MO_2 compounds. MnO_2 (Mn^{4+}), while not a maximum value in the MO_2 curve, sits at a much higher disordering energy than neighboring CrO_2, which can be attributed to the electronic structure of Mn^{4+} as described above.

The disordering energy of $LiFeO_2$, however, is not consistent with experimental observations. $LiFeO_2$ is known to disorder at solid state synthesis temperatures.[80] The data in **Figure 3-2**(a) however suggests that the disordering energy of $LiFeO_2$ is higher than the disordering energy of lithiated transition metals such as $LiVO_2$, $LiMnO_2$ and $LiNiO_2$, which do not disorder at solid-state synthesis temperatures. It is possible that experimentally synthesized $LiFeO_2$ has in fact a certain level of off-stoichiometry, as partial reduction of Fe^{3+} to Fe^{2+}, mediated by oxygen loss, is likely at synthesis temperatures.[92] It is also possible that PBE+U overestimates the disordering energy of $LiFeO_2$. In the latter case, the predicted voltage change for $LiFeO_2$ upon disorder would be underestimated. This potential underestimation, however, does not change the conclusions presented in this Chapter, among which that the voltage of $LiFeO_2$ increases upon disorder.

This study has shown that, depending on the transition metal species, cation disorder can lead to an increase or a decrease of the average voltage (**Figure 3-2**(b)). We note that this conclusion is in disagreement with a previous result presented in the literature.[21] Using a simplified model for the average voltage based on chemically intuitive quantities, it was argued that the voltage of disordered $LiMO_2$ compounds is necessarily higher than the voltage of their ordered counterparts. This statement, however, can be shown to be in contradiction with the existence of compounds that disorder *in situ* during delithiation, such as $LiVO_2$,[16] and $LiCrO_2$.[1,4,76] Such materials are ordered in their lithiated forms, thus guaranteeing that the disordering energy is high enough to prevent cation disorder upon synthesis (**Figure 3-3**(a)). At a certain level of delithiation, the disordered state becomes thermodynamically favorable over the ordered state, leading to *in situ* cation disorder upon first charge. During subsequent cycles, the material cycles in the disordered form. By virtue of the relative free energies of the ordered and

disordered states in the lithiated and delithiated limits (**Figure 3-3**(a)), the condition $\left(\underline{E}^{dis}_{MO_2} - \underline{E}^{ord}_{MO_2}\right) < \left(\underline{E}^{dis}_{LiMO_2} - \underline{E}^{ord}_{LiMO_2}\right)$ is necessarily verified (the left hand term is negative, while the right hand term is positive). Consequently, the voltage of the disordered state is necessarily lower than the voltage of the ordered state. This analysis further rationalizes the voltage drop observed following first charge in the Li-excess $Li_{1.211}Mo_{0.467}Cr_{0.3}O_2$ compound,[15] which also disorders *in situ* upon delithiation.

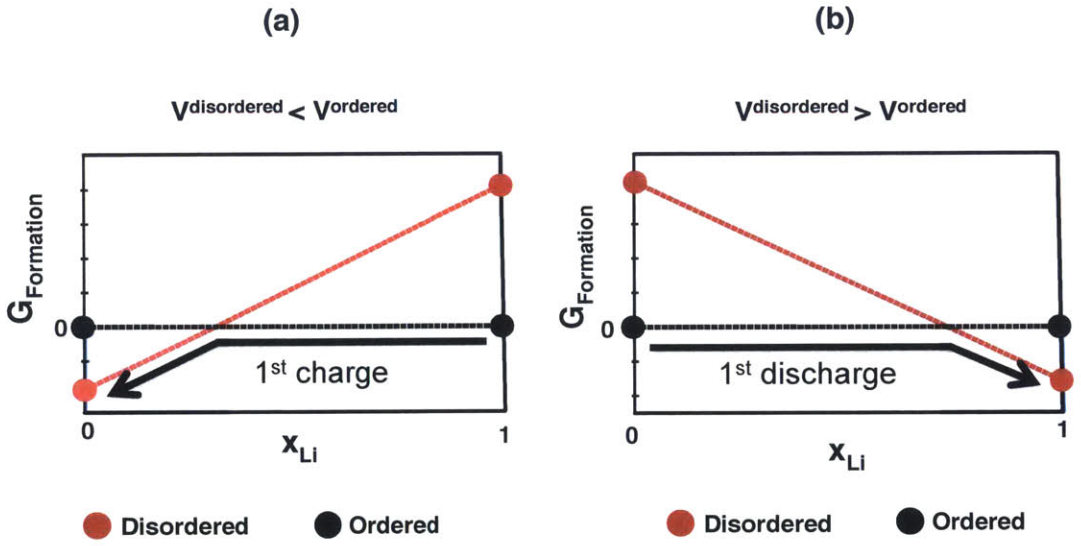

Figure 3-3: Free energy landscape and ensuing voltage relations for compounds that disorder in situ during **(a)** Lithiation **(b)** Delithiation.

Conversely, compounds that disorder *in situ* during lithiation must have a higher voltage in their disordered form than in their ordered form (**Figure 3-3**(b)). Using the reasoning presented in the previous paragraph, the relative ordered and disordered free energies in the lithiated and delithiated limits ensure that $\left(\underline{E}^{dis}_{MO_2} - \underline{E}^{ord}_{MO_2}\right) > \left(\underline{E}^{dis}_{LiMO_2} - \underline{E}^{ord}_{LiMO_2}\right)$. Consequently, the voltage

of the disordered state is necessarily higher than the voltage of the ordered state. This analysis explains the increase in average voltage that is observed after the first discharge of $Li_{1+y}VO_3$ [16] and rutile TiO_2.[78,79]

This analysis provides general rules for the voltage evolution of materials that disorder *in situ*. In systems that allow it, *in situ* cation disorder can therefore be used as leverage to increase or decrease the average voltage. Certain Cr-containing compounds, for example, are known to disorder upon delithiation ($LiCrO_2$,[14,76] $Li_{1.211}Mo_{0.467}Cr_{0.3}O_2$ [15]). The reduction in the average voltage that ensues can be leveraged to access more capacity at moderate voltages before competing mechanisms, such as oxygen oxidation[90,93,94] or oxygen loss,[24] occur at higher voltages. In line with this statement, the disordered $Li_{1.211}Mo_{0.467}Cr_{0.3}O_2$ compound was experimentally shown to access the $Cr^{3+/4+}$ redox at the end of charge with minimal competing redox from oxygen loss.[95] In $Li_{1+y}VO_3$, *in situ* cation disorder during lithiation is also leveraged to increase the low voltage in the initial ordered compound, thus enabling higher energy density in this compound. Note that the previous analysis does not apply to compounds that experience a change of chemical composition in conjunction with cation disorder (surface cation disorder mediated by oxygen loss is one such instance).[17,22,23,27,28]

General conclusions about the relative average voltages of the ordered and disordered phases cannot be drawn, however, for materials that disorder upon synthesis. In this family of compounds ($LiFeO_2$,[80] $LiTiO_2$,[80] $LiM_{0.5}Ti_{0.5}O_2$ (M=Mn, Fe, Co, Ni),[82-84] $Li_{1+x}Nb_yM_zO_2$ [M=Mn, Fe, Co, Ni],[18,19] $Li_{1.2}Ni_{0.33}Ti_{0.33}Mo_{0.14}O_2$,[17] $Li_{1+x}Ti_{2x}Fe_{1-3x}O_2$ [20]), the free energy difference between the disordered state and the ordered ground-state in the lithiated limit is small enough to ensure that cation disorder can occur at synthesis temperatures (the energy

increase upon disorder being compensated by the *-TS* term at high temperature). There is no *a priori* relationship, however, between the relative disordering energy in the lithiated and delithiated limits for these compounds. The disordering energy can be higher in the delithiated limit, which leads to a higher disordered voltage (such is the case for $LiTiO_2$ and $LiFeO_2$ as calculated in this study). It is also possible that compounds in this family be even easier to disorder in the delithiated limit, in which case the voltage of the disordered phase would be lower than that of the lithiated ordered ground-state.

Our analysis also demonstrates that the disordered voltage of the $Ni^{3+/4+}$ redox is high. This conclusion, demonstrated both for disordered $LiNiO_2$ and disordered $LiNi_{0.5}Ti_{0.5}O_2$, has important implications, as Ni is an important high-voltage transition metal for Li-ion battery cathodes. While the large voltage of the disordered Ni^{3+}/Ni^{4+} couple leads to a beneficial increase in energy density, it can also lead to the appearance of competitive redox processes. Such processes include oxygen oxidation[90,93,94] and oxygen evolution.[24] The ~4.4V range calculated for the $Ni^{3+/4+}$ redox suggests that the disordered $Ni^{3+/4+}$ redox can be hard to access in practice, consistent with the large oxygen activity observed in the disordered Li-excess $Li_{1.2}Ni_{0.33}Ti_{0.33}Mo_{0.14}O_2$ compound.[17] If oxygen oxidation is to be avoided, transition metals with lower disordered voltages such as Cr, Mn, Co and Fe may be preferable over Ni. On the other hand, if oxygen oxidation were to be reversibly achieved without degradation of overall performance, synthesizing disordered materials with a high $3^+/4^+$ redox voltage may be a valid design strategy.

3.5 Conclusion

Using first principles calculations, this work demonstrated that, depending on the transition metal species, cation disorder can result in an increase or a reduction of the average Li intercalation voltage of lithium transition-metal oxides. Transition metals that have a higher disordering energy in the MO_2 limit display larger average voltages than their ordered ground-states, while transition metals that have a higher disordering energy in the $LiMO_2$ limit display a lower voltage than their ordered ground-state. Cation-disorder can significantly alter the average voltage of lithium transition metal oxides (ΔV between -0.3V and 0.6V) and can therefore lead to significant changes in their voltage operating windows. In particular, the disordered $Ni^{3+/4+}$ redox was found to be high (~4.4V), suggesting that it is likely to be preceded by oxygen activity in disordered compounds. We also showed that compounds that disorder *in situ* during delithiation have a lower voltage in their disordered form, while compounds that disorder *in situ* during lithiation have a higher voltage in their disordered form. Our work therefore establishes the first bases towards rational design of high-capacity Li-excess disordered transition-metal oxides based upon voltage considerations.

Chapter 4 :

The effect of cation disorder on the voltage profile of Li transition metal oxides

4.1 Introduction

Cation disorder is a phenomenon that is becoming increasingly important in the field of Li-ion batteries. As-synthesized disordered Li-excess rocksalts ($Li_{1+x}Nb_yM_zO_2$ [M=Mn, Fe, Co, Ni],[18,19] $Li_{1.2}Ni_{0.33}Ti_{0.33}Mo_{0.14}O_2$,[17] $Li_{1+x}Ti_{2x}Fe_{1-3x}O_2$ [20]) were recently shown to achieve high reversible capacity, paving the way towards a new design space of high-capacity Li-ion battery cathodes. These high capacities are enabled by macroscopic Li transport through percolating zero-transition-metal pathways, which remain active upon disorder.[15,75] *In situ* cation disorder also occurs in a large class of ordered materials, resulting in the formation of disordered bulk phases ($Li_{1.211}Mo_{0.467}Cr_{0.3}O_2$,[15] Li_2VO_3,[16] $LiCrO_2$,[14,76] $Li_{0.96}VO_2$,[77] rutile TiO_2 [78,79]). Furthermore, *in situ* cation disorder can also occur at the surface of ordered compounds as a result of oxygen loss and transition metal migration, such as is the case for the NCA

($LiNi_{0.8}Co_{0.2}Al_{0.05}O_2$)[29] and Li-excess NMC ($Li_{1+y}Ni_wCo_zMn_{2-y-w-z}O_2$) compounds.[23,27,28]

Understanding the effect of cation disorder on the voltage profile of transition metal oxides is therefore critical, both to rationally design high-capacity disordered Li-excess rocksalts as well as to predict the voltage evolution of ordered materials subject to *in situ* bulk or surface cation disorder.

Cation disorder is expected to increase the voltage slope of lithium transition metal oxides, as Li sees a variety of local transition metal environments in a disordered structure, and hence a large variety of local Li chemical potentials. The voltage slope ($\frac{dV}{dx_{Li}}$) is a critical quantity for the design of cation-disordered rocksalts, as it controls the capacity accessible at voltages below the stability limit of the electrolyte (nominally 4.5V for standard organic electrolytes,[3] limit which can be pushed to 4.7V with proper surface coatings). In this study, we develop models based on first principles to understand the magnitude and the factors that control the voltage slope of cation-disordered rocksalts. The effect of cation disorder on transition metals undergoing a $3^+/4^+$ redox reaction is investigated through a systematic study of first-row $LiMO_2$ compounds (M=Ti, V, Cr, Mn, Fe, Co, Ni). Among these compounds, $LiTiO_2$ and $LiFeO_2$, are known to disorder at solid-state synthesis temperature[80] while $LiVO_2$ [77] and $LiCrO_2$[14,76] can disorder upon cycling at room temperature. Co and Ni, although not found to disorder in the stoichiometric $LiMO_2$ form, disorder as part of mixed transition metal systems ($LiM_{0.5}Ti_{0.5}O_2$ compounds, where M=Mn, Fe, Co, Ni).[82-85]

Our work demonstrates that the voltage slope increase upon cation disorder is induced by a statistical distribution of Li site energies and by the occupancy of tetrahedral sites by Li. We

further show that short-range order, which is present in actual disordered materials, reduces the voltage slope with respect to the fully random limit. Finally, we demonstrate that the voltage slope increase upon disorder is generally smaller for high-voltage transition metals than for low-voltage transition metals and that the additional tetrahedral capacity resulting from disorder is smaller in Li-excess compounds than in stoichiometric compounds. This study therefore provides critical insights for the design of high-capacity Li-excess cation disordered rocksalts based upon voltage considerations.

4.2 Model

Cation disorder is defined as cation-mixing between the transition metal sublattice and the Li sublattice of an initially ordered structure (e.g. the layered structure of **Figure 4-1**(a)). To quantify the amount of cation-mixing, we further distinguish between *partial* (**Figure 4-1**(b)) and *full* (**Figure 4-1**(c)) cation disorder. In the limit of fully disordered $LiMO_2$ rocksalts, Li and M randomly occupy cation sites in the rocksalt lattice (**Figure 4-1**(c)). In this section, we outline the factors that contribute to the voltage slope of cation disordered rocksalts. We demonstrate that the voltage slope of cation disordered rocksalts is a combination of a statistical distribution of site energies (controlled by the effective Li-M interaction, as defined later in the text), interaction between adjacent Li sites (controlled by the effective Li-Va interaction, as defined later in the text) and occupancy of high-voltage tetrahedral sites by Li. We further explain how each contribution to the voltage slope can be quantitatively evaluated using first principles calculations and a simple lattice model.

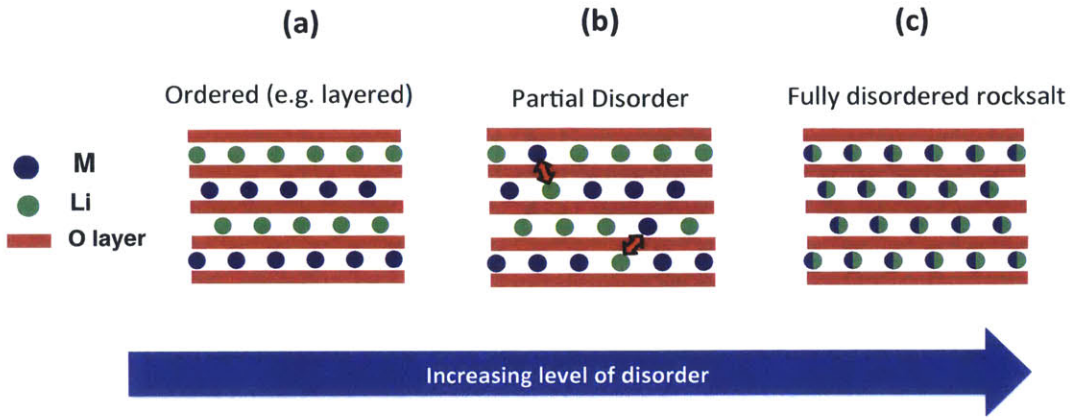

Figure 4-1: Different levels of cation-disorder in $LiMO_2$ compounds **(a)** Fully ordered (e.g. layered) $LiMO_2$ compound (the layers being the (111) planes of the FCC cation sublattice) **(b)** Partially disordered compound **(c)** Fully disordered rocksalt.

We first consider the factors that control the voltage slope in ordered (e.g. layered) $LiMO_2$ compounds. In the layered structure, each Li site sees the same local transition metal environment (six out of the twelve nearest neighbor sites are occupied by M, as indicated by the red curve of **Figure 4-2**(b)-(i)). The site energy ΔE_{site}, which is defined as the Li insertion/extraction energy when adjacent Li sites do not interact with each other, is uniform across the structure due to the uniformity of the transition metal environment around each Li site. In the absence of interactions between adjacent Li sites, the Li-Va binary system is therefore an ideal solution, with a small ~0.1 V voltage slope induced solely by entropic effects ($V(x_{Li}) = \overline{V} - kT\ln\left(\frac{x_{Li}}{1-x_{Li}}\right)$, $\left.\frac{dV}{dx_{Li}}\right|_{x_{Li}=0.5} = -4kT \approx 0.1V$). In practice, the voltage slope in the layered structure is therefore controlled by the interaction between adjacent Li sites (or more rigorously, by the effective Li-Va interaction, as will be defined later in the text). This

interaction makes states of intermediate Li concentration thermodynamically favorable over a linear combination of the $LiMO_2$ and MO_2 end-members (**Figure 4-2**(a)-(i)), by favoring Li-Va pairs over a linear combination of Li-Li and Va-Va pairs. This in turn increases the voltage slope, which is given by the curvature of the formation free energy curve $\left(\frac{dV}{dx_{Li}} = -\frac{d^2G_f}{(dx_{Li})^2}\right)$.

Thus, the stronger the interaction between Li sites, the more stable states at intermediate concentrations are, and the larger the voltage slope becomes (**Figure 4-2**(a)-(ii)) .

We now consider the factors that control the voltage slope in disordered structures. Cation disorder creates a statistical distribution of local transition metal environments around Li sites. **Figure 4-2**(b)-(i) (black curve) shows the probability that, out of the 12 nearest neighbors of a given Li atom, Z^M neighbors be transition metals. This variety of local environments results in a spread of Li site energies (controlled by the effective Li-M interaction, as defined later in the text), characterized by a standard deviation $\sigma_{\Delta E_{site}}$. Cation disorder therefore creates a voltage slope even in the absence of interaction between Li sites (Li sites with high ΔE_{site} are extracted first, followed by sites with low ΔE_{site}). The interaction between Li sites further contributes to increase the voltage slope, by favoring Li-Va pairs over phase-separated Li-Li and Va-Va pairs. In disordered structures, the net voltage slope is therefore a combination of both the site energy distribution and the effective Li-Va interaction, as illustrated in **Figure 4-2**(b)-(ii). Disordering a layered compound is therefore expected to lead to a voltage slope increase.

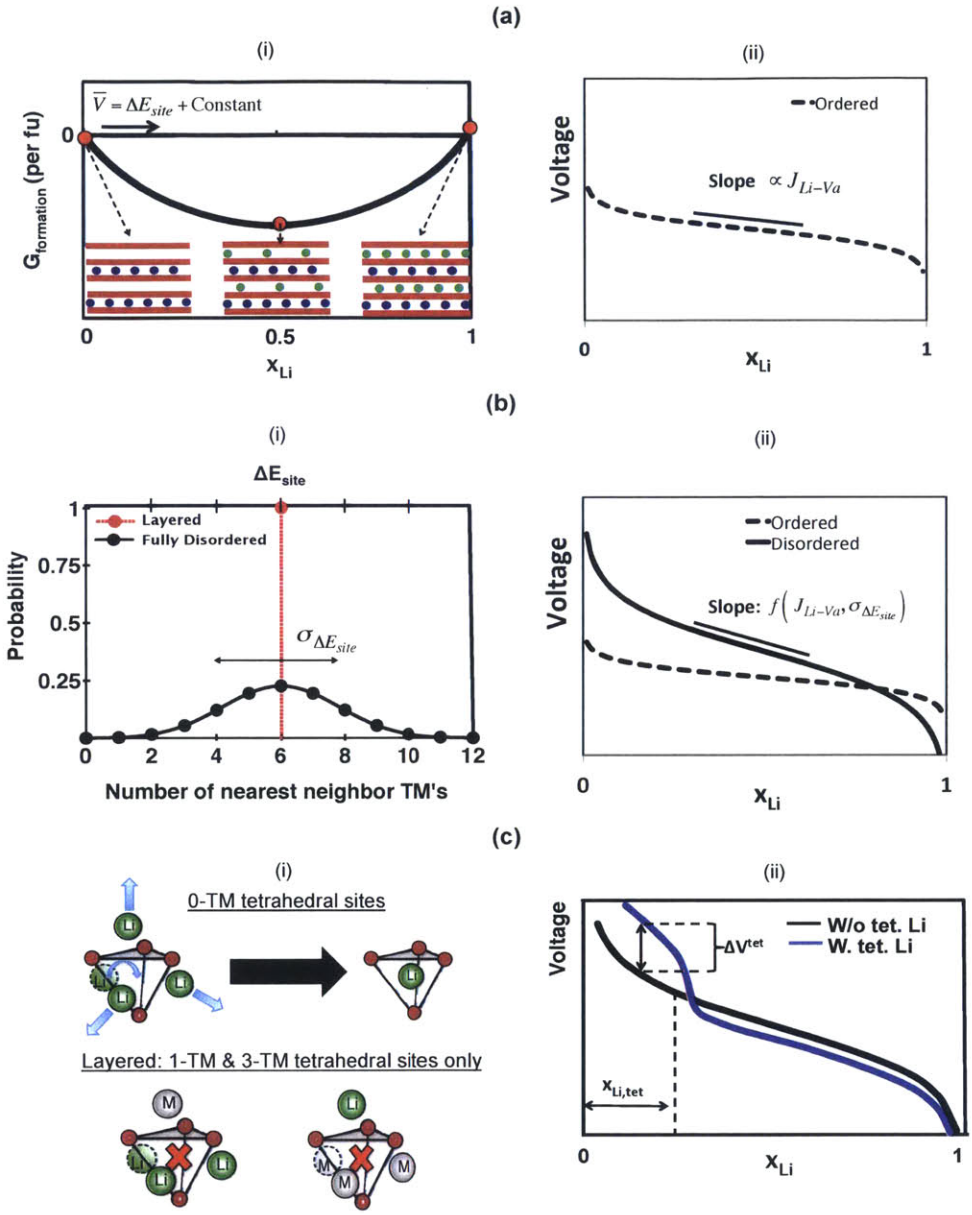

Figure 4-2: Factors that contribute to the voltage slope increase upon cation disorder in lithium transition metal oxides **(a)** In ordered (e.g. layered) compounds, the effective Li-Va interaction (J^{Li-Va}) controls how stable states of intermediate concentrations are relative to the $LiMO_2$ and MO_2 end members (i), which in turn controls the voltage slope (ii) **(b)** In

disordered compounds: (i) The statistical distribution of local environments around Li sites results in a statistical distribution of ΔE_{site} and (ii) Both J^{Li-Va} and $\sigma_{\Delta E_{site}}$ (the standard deviation of ΔE_{site}) contribute to the voltage slope. **(c)** High-voltage tetrahedral sites can be occupied by Li when all face-sharing octahedral sites are vacant (i) This can occur in disordered $LiMO_2$ compounds via delithiation of "0-TM" tetrahedral sites, but not in the (stoichiometric) layered structure, as each tetrahedral site has at least one transition metal neighbor. (ii) Tetrahedral Li occupancy leads to a voltage increase at the end of charge, and a corresponding lowering of the voltage everywhere else to conserve the average voltage.

Cation disorder also leads to occupancy of high-voltage tetrahedral sites by Li (**Figure 4-2**(c)). Tetrahedral sites are energetically favorable over octahedral sites if all face-sharing octahedral sites are vacant. Occupancy of tetrahedral sites by Li creates a high-voltage region in the voltage profile, as is observed in cation-mixed $LiNi_{0.5}Mn_{0.5}O_2$ [96] and spinel Li_xMnO_2 (in the $x_{Li}=[0, 0.5]$ range[97]). Only tetrahedral sites that respect the "0-TM" condition[15] in the lithiated form of the compound can be occupied by Li upon delithiation (**Figure 4-2**(c)-(i)). After extraction of three out of the four face-sharing Li around such 0-TM tetrahedral sites, the remaining Li migrates into the tetrahedral site, where it sits at a high voltage. The 0-TM condition is never met in the (stoichiometric) layered structure, as each tetrahedral site has at least one transition metal neighbor (**Figure 4-2**(c)-(i)). Cation disorder, however, creates a statistical distribution of metal environments around tetrahedral sites, such that the 0-TM condition can be met with a certain probability. The effect of tetrahedral occupancy on the voltage profile of cation-disordered rocksalts is schematically illustrated in **Figure 4-2**(c)-(ii). Note that the presence of a high voltage region at the end of charge is accompanied by a lowering of the voltage everywhere else, to conserve the average voltage (which only depends on the free energy of the $LiMO_2$ and MO_2 end-members).

In order to quantitatively evaluate the voltage slope of cation-disordered rocksalts, the standard

deviation of the site energy distribution, the interaction between Li sites and the high-voltage capacity resulting from tetrahedral Li occupancy are evaluated from first principles. Cluster expansions based on pair interactions are developed to evaluate the voltage slope arising from Li insertion in octahedral sites (capturing the combined effect of the site energy distribution and the interaction between Li sites), while the additional effect of tetrahedral Li occupancy on the voltage profile ($x_{Li,tet}$ and ΔV^{tet} in **Figure 4-2**(c)) is estimated from probability theory and from first principles evaluations. These methods are detailed in the following paragraphs.

Cluster expansions[64-66,88,98] allow to map the energy of any Li-M-Va configuration in disordered Li_xMO_2 onto a finite set of Effective Cluster Interactions (ECI's). In this work, pair-wise cluster expansions are used to evaluate the voltage slope associated with Li insertion into octahedral sites. In order to take advantage of the cluster expansion framework, the site energy ΔE^i_{site} and the interaction between adjacent Li sites must be expressed in terms of Effective Cluster Interactions, which are then fitted to a set of energies obtained from first principles.

Under a pair term approximation, the energy landscape in a Li-M-Va system is entirely described by three effective cluster interactions: the effective Li-M interaction ($J^{Li\text{-}M}$), the effective Va-M interaction ($J^{Va\text{-}M}$) and the effective Li-Va interaction ($J^{Li\text{-}Va}$). These effective interactions can be expressed as combinations of all possible pair energies on the lattice ($E^{Li\text{-}M}$, $E^{Va\text{-}M}$, $E^{Li\text{-}Va}$, $E^{Li\text{-}Li}$, $E^{Va\text{-}Va}$, $E^{M\text{-}M}$):

$$-2J^{A-B} = \left[E^{A-B} - \frac{\left(E^{A-A} + E^{B-B}\right)}{2} \right] \tag{45}$$

Where A and B can be either Li, M or Va. Now consider a disordered rocksalt in which the transition-metal positions are random but fixed. Limiting the interaction between Li sites to the nearest neighbor shell, the energy of a given Li/Va configuration in the Li/Va sublattice can be written as :

$$E(\sigma) = \sum_i \frac{\Delta E^i_{site}}{2} \sigma_i + \sum_{i,j \in nn\ pairs} J^{Li-Va}_{nn} \sigma_i \sigma_j \tag{46}$$

Where σ_i is the occupation of site i on the Li/Va sublattice ($\sigma_i = \{1,-1\}$ for $\{Li,Va\}$), ΔE^i_{site} is the site energy of site i and J^{Li-Va}_{nn} is the interaction term between adjacent Li sites. More precisely, J^{Li-Va}_{nn} is the nearest neighbor effective Li-Va interaction, which captures the preference for Li-Va pairs over phase-separated Li-Li and Va-Va pairs (equation (45) with A=Li and B=Va).

The site energy ΔE^i_{site} is defined as the Li insertion energy when adjacent Li sites do not interact with each other ($J^{Li-Va}_{nn} = 0$). It can be expressed terms of the following lattice pair energies:

$$\Delta E^i_{site} = \sum_{Neighbor\ shell\ k} \left\{ Z^{M,(i)}_k \left(E^{Li-M}_k - E^{Va-M}_k \right) + \frac{\left(Z_k - Z^{M,(i)}_k \right)}{2} \left(E^{Li-Li}_k - E^{Va-Va}_k \right) \right\} \tag{47}$$

Where the subscript k denotes the k^{th} neighbor shell, Z_k is the total coordination number of the k^{th} neighbor shell and $Z_k^{M,(i)}$ is the number of transition metals around site i in the k^{th} neighbor shell. The site energy can be re-expressed in terms of the effective Li-M and Va-M interactions via the following relation:

$$\Delta E_{site}^{i} = \sum_{Neighbor\ shell\ k} \left[-2Z_k^{m,(i)} \left(J_k^{Li-M} - J_k^{Va-M} \right) \right] + C \tag{48}$$

Where C is a constant chemical potential shift that defines the chemical potential reference (set to zero for Li metal). The site energy therefore emerges as the difference between the effective Li-M interaction and the effective Va-M interaction over several neighbor shells, which we will simply refer to as the "effective Li-M interaction" in the rest of the text. After obtaining suitable values for J^{Li-Va}, J_k^{Li-M} and J_k^{Va-M}, the lattice model can be combined with Monte Carlo simulations to determine the open circuit voltage profile $V(x_{Li})$ and hence the voltage slope $\frac{dV}{dx_{Li}}$. Note that all octahedral voltage slopes reported in this Chapter are obtained by performing a linear fit to the voltage curve in the x_{Li}=[0.25, 0.75] capacity range.

J_{nn}^{Li-Va} is fitted to the slope of the layered structure. The lowest-energy Li_xMO_2 configurations (x=0, 0.25, 0.5, 0.75, 1) are identified among all structures containing up to four formula units of Li_xMO_2 (this size limit ensures that known ground-states on the layered structure are captured[99]). Energy evaluations are performed within the Hubbard-U corrected Generalized Gradient Approximation (GGA+U) to Density Functional Theory (DFT), using the PBE

exchange-correlation functional.[58,87] The U parameters are extracted from the work of Jain et al.[61]

J^{Li-M} and J^{Va-M} are obtained by fitting two pair-based cluster expansion: one for Li/M occupancy in disordered $LiMO_2$ and one for Va/M occupancy in disordered MO_2. The structure set on which the fit is performed is the set of all periodic cation-mixed structures with unit cells containing up to four formula units of $LiMO_2$ (i.e. eight cations). This subset of 121 symmetrically distinct structures includes all experimentally observed structures in the $LiMO_2$ rocksalt lattice, including the layered, γ-$LiFeO_2$, orthorombic and spinel structure. Only structures that map onto the FCC rocksalt lattice, where both Li/Va and M atoms are octahedrally coordinated by oxygen, are considered in the fit, i.e. structures where transition metals migrate to tetrahedral sites are not included. Structures where O-O bonds form are also disregarded, as GGA+U is known to overstabilize O-O bonding. The fit is obtained by considering pair interactions up to the fifth neighbor. The cluster expansion fits are performed within the compressive sensing paradigm, using the split Bregman algorithm.[66]

In this study, we therefore limit the lattice model for Li insertion into octahedral sites to pair interactions. The accuracy of this approximation can be assessed by comparing the predictions of the pair term model with alternate methods using higher order interactions (see the Appendix of this chapter). In the Appendix of this Chapter, we demonstrate that Monte Carlo sampling on fully lithiated and fully delithiated supercells is able to extract the standard deviation of the site energy distribution ($\sigma_{\Delta E_{site}}$) in the random limit using cluster expansions containing higher order interactions (including triplets and quadruplets interactions, as detailed in Chapter 3). We find that the pair term model correctly predicts the (site-energy induced)

voltage slope of fully disordered $LiMO_2$ to within 0.2V, which leads to an uncertainty of 0.1V in the high voltage limit and therefore constitutes a good approximation (c.f. **Figure 4-7** in the Appendix of this Chapter).

We further estimate the additional voltage step induced by tetrahedral Li occupancy (ΔV^{tet} in **Figure 4-2**(c)-(ii)) based on the spinel structure. The topology of the spinel structure is such, that at $x_{Li}=0.5$, all Li atoms occupy 0-TM tetrahedral sites.[97] Tetrahedral Li occupancy therefore induces a high-voltage region in the $x_{Li}=[0, 0.5]$ range. Using Density Functional Theory, we can compare the voltage plateau arising from tetrahedral occupancy with the voltage plateau arising from octahedral Li occupancy in the same concentration range. The difference between these two voltage plateaus can be used to estimate the voltage slope increase in disordered rocksalts resulting from tetrahedral Li occupancy (ΔV^{tet} in **Figure 4-2**(c)-(ii); more details are given in **Figure 4-7** of the Appendix of this Chapter). The capacity resulting from tetrahedral Li occupancy ($x_{Li,\,tet}$) can then be calculated from probability arguments (method detailed in the Results section).

Using the model described above, the voltage slope can be evaluated for both fully disordered (i.e. random) $LiMO_2$ as well as for practical disordered $LiMO_2$ compounds containing a certain degree of short-range order. The method for determining short-range order is presented in the Results section.

4.3 Results

4.3.1 Octahedral Li occupancy

In this section, we consider the contribution of octahedral Li insertion to the voltage slope of fully disordered $LiMO_2$ compounds. We first consider the effect of the site energy distribution on the voltage profile. The black curves of **Figure 4-3**(a) illustrate two voltage profiles, for $LiTiO_2$ and $LiNiO_2$ respectively, in the absence of the effective Li-Va interaction. The difference in the site-energy induced voltage slopes between these compounds is large, suggesting that the site energy contribution to the voltage slope strongly depends on the transition metal. The black bars of **Figure 4-3**(a) show the site energy contribution to the voltage slope for different transition metals. This slope varies between extremal values of 2.1V for $LiTiO_2$ and 0.5V for $LiNiO_2$. **Figure 4-4**(a) shows the relationship between the (site-energy induced) voltage slope and the average voltage of disordered $LiMO_2$ compounds. It is found that high-voltage transition metals generally have a lower (site-energy induced) voltage slope than low voltage transition metals (**Figure 4-4**(b)). This inverse correlation is favorable for the design of high-voltage cation-disordered rocksalts, as a high average voltage and a low voltage slope are simultaneously desirable to access maximal capacity at high energy. The origin and implication of this inverse correlation are discussed further in the Discussion section of this Chapter.

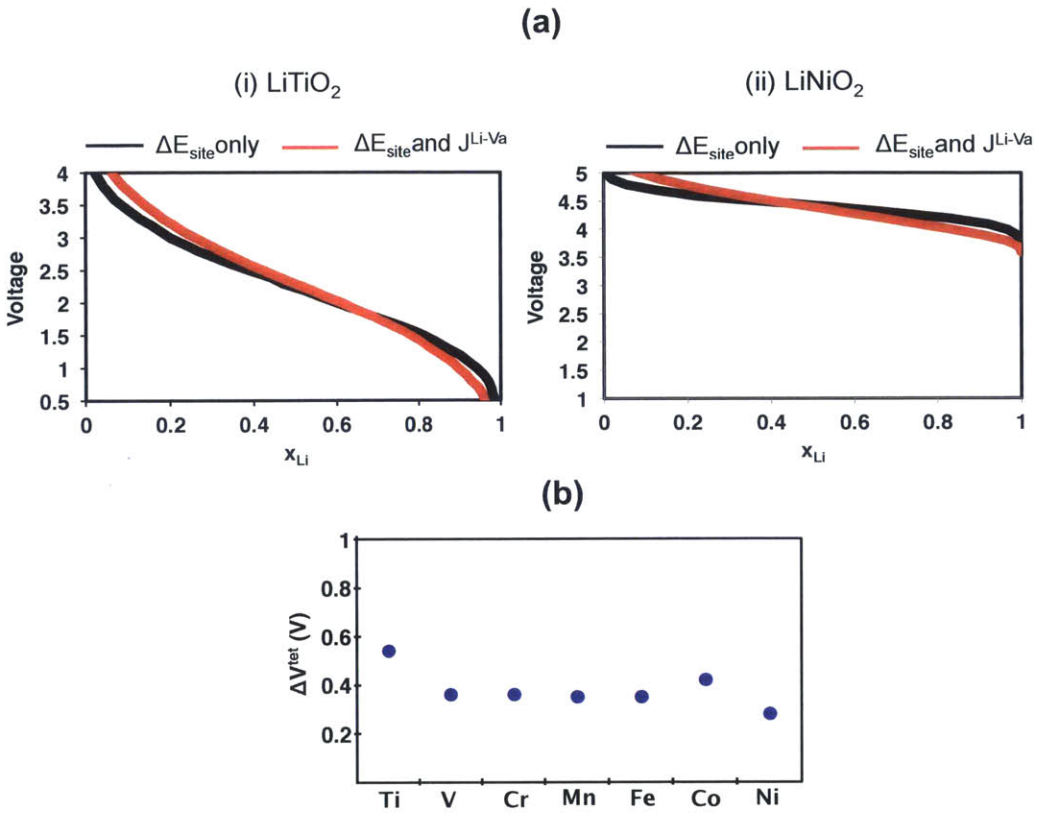

Figure 4-3: **(a)** Illustration of the voltage profile of fully disordered (i) $LiTiO_2$ and (ii) $LiNiO_2$ when Li insertion is restricted to octahedral sites. The black curves show the site energy contribution to the voltage slope, while the red curve shows the combined effect of ΔE_{site} and J^{Li-Va} **(b)** Additional high-voltage contribution resulting from tetrahedral site occupancy in disordered $LiMO_2$ (ΔV^{tet} in **Figure 4-2**(c)), as determined from the spinel structure.

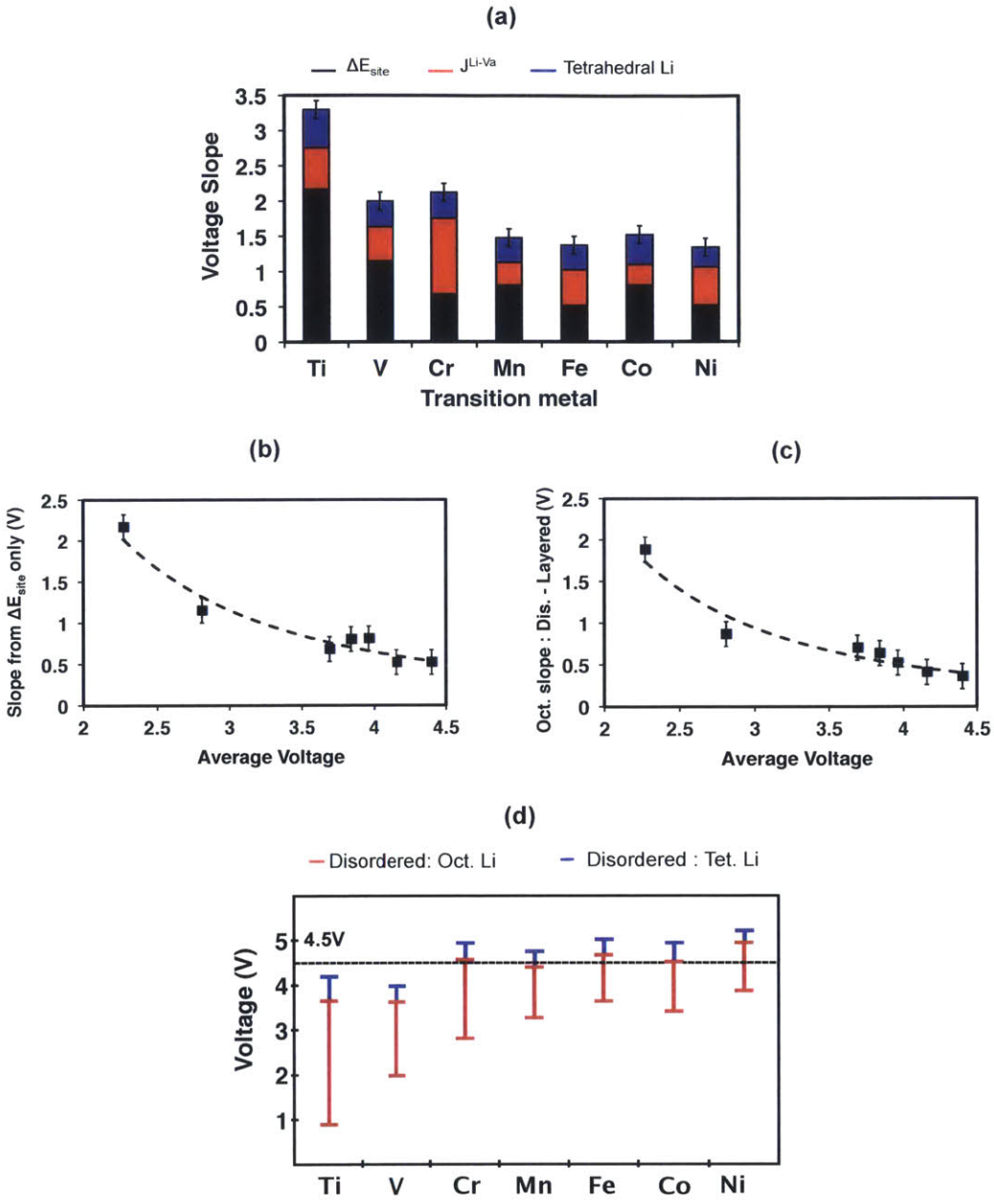

Figure 4-4: Voltage slope and voltage range of fully disordered $LiMO_2$ **(a)** Voltage slope contributions from ΔE_{site} , $J^{Li\text{-}Va}$ and tetrahedral Li for each compound **(b)** Site-energy contribution to the voltage slope as a function of the average voltage of the disordered structure. High-voltage compounds have a lower (site-energy induced) voltage slope than low-

voltage compounds, as evidenced by the dashed trend line **(c)** Octahedral voltage slope increase upon full disorder of an initially layered $LiMO_2$ compound. The voltage slope increase is smaller for high-voltage compounds, due to the smaller effect of the site-energy induced slope. **(d)** Voltage range of fully disordered $LiMO_2$. The red bar represents the voltage range associated with octahedral Li insertion, while the blue bar highlights the additional high voltage contribution associated with insertion of Li in tetrahedral sites. The dashed line represents the 4.5V line, which represents a lower bound for the electrolyte stability limit.

We now consider the additional effect of the effective Li-Va interaction on the voltage slope of fully disordered $LiMO_2$. The calculated voltage slope of the layered structure, on which the effective Li-Va interaction J_{nn}^{Li-Va} is fitted, is given in Table 4-1.

Table 4-1: Calculated voltage slope of the layered structure in first row $LiMO_2$ compounds (M=Ti, V, Cr, Mn, Fe, Co, Ni) (PBE+U)

	$LiTiO_2$	**$LiVO_2$**	**$LiCrO_2$**	**$LiMnO_2$**	**$LiFeO_2$**	**$LiCoO_2$**	**$LiNiO_2$**
Slope (V)	0.85V	0.75V	1.05V	0.50V	0.60V	0.60V	0.70V

The red curves of **Figure 4-3**(a) illustrate the combined contribution of ΔE_{site} and of the effective Li-Va interaction on the voltage profile of fully disordered $LiTiO_2$ and $LiNiO_2$. The presence of the effective Li-Va interaction increases the voltage slope, while keeping the average voltage constant. The combination of the black and red bars in **Figure 4-3**(a) shows the voltage slope associated with Li insertion in octahedral sites for different transition metals, when both the site energy distribution and the effective Li-Va interaction are taken into account. The effect of the Li-Va interaction on the voltage slope is found to be proportional to the slope of the layered structure reported in Table 4-1. It is strongest for $LiCrO_2$ (layered

slope of 1.05V) and lowest for $LiMnO_2$ (layered slope of 0.5V). The strong Li-Va interaction in the Cr system is responsible for the higher octahedral voltage slope of disordered $LiCrO_2$ with respect to other high-voltage transition metals (Mn, Fe, Co, Ni) and also accounts for the higher octahedral voltage slope of $LiCrO_2$ with respect to $LiVO_2$, despite $LiVO_2$ having a larger site-energy induced voltage slope due to its lower average voltage.

Figure 4-4(c) illustrates the increase in voltage slope resulting from full disorder of an initially layered $LiMO_2$ compound. The voltage slope increase upon disorder is found to inversely correlate with the average voltage of the disordered structure, in a manner similar to that of the site energy (**Figure 4-4**(c)). This indicates that the octahedral voltage slope increase upon disorder is largely attributable to the creation of a site energy distribution resulting from Li-M interactions.

The voltage range for octahedral Li insertion in fully disordered $LiMO_2$ is illustrated by the red bars of **Figure 4-4**(d) (this voltage range is defined by $\left[\overline{V}-\frac{Slope}{2},\overline{V}+\frac{Slope}{2}\right]$, where $\overline{V}$ is the average voltage) . As a result of the smaller site energy contribution to the voltage slope, high-voltage transition metal compounds are found to only have a small amount of capacity above the 4.5-4.7V stability limit of the electrolyte, with the exception of $LiNiO_2$ which has a high average voltage in its disordered form.[100] For all transition metals except Ni, cation disorder therefore does not lead to significant inaccessible octahedral Li capacity. (It is to be noted that, in the case of $LiCrO_2$, disorder also leads to an average voltage decrease of ~0.3V with respect to the layered ground-state (cf Chapter 3). [100] This decrease partially accounts for the small capacity observed above 4.5V in this compound).

4.3.2 Tetrahedral Li occupancy

In addition to octahedral sites, Li can also occupy tetrahedral sites in disordered structures. Probability arguments can be used calculate the tetrahedral Li capacity in a fully disordered $LiMO_2$ rocksalt. In a fully lithiated $LiMO_2$ rocksalt, each cation site can be occupied by Li with a probability of $\frac{1}{2}$. The probability for a given tetrahedral site to respect the 0-TM condition is therefore $\left(\frac{1}{2}\right)^4$. Furthermore, there are 2 tetrahedral sites per cation site, or 4 tetrahedral sites per formula unit of $LiMO_2$. The maximal tetrahedral capacity in fully disordered $LiMO_2$ is therefore 0.25 formula units (f.u.) of Li:

$$\text{Tetrahedral Capacity}\left(\text{fully disordered } LiMO_2\right) = 4\left(\frac{1}{2}\right)^4 = 0.25 \tag{49}$$

Figure 4-3(b) shows the scale of the voltage increase at the end of charge resulting from Li occupancy of tetrahedral sites, as determined from the spinel structure. The resulting voltage increase is found to be on the order of 0.3V-0.5V, depending on the transition metal. This additional contribution therefore leads to up to 25% capacity outside the 4.5V-4.7V stability of the electrolyte for high-voltage transition metals (blue bars of **Figure 4-4**(d)).

4.3.3 Effect of short-range order

In practice, cation-disordered rocksalts are not random but in fact exhibit a certain degree of short-range order.[82] The degree of short-range order resulting from an order-disorder transition at high synthesis temperatures can be computationally evaluated using Monte Carlo annealing simulations (**Figure 4-5**(a)). This is made possible by the use of $LiMO_2$ cluster expansions which accurately reproduce the $LiMO_2$ ground-state structure while predicting the energy of any given Li/M ordering to within ~25 meV/cation (cf Chapter 3). For all transition metals, it is found that the energy of thermally disordered structure is lower than the energy of the fully random structure, indicating that a certain amount of short-range order is still present upon thermal disorder. In the case of $LiFeO_2$, for example, the energy of the disordered structure (referenced to the ground-state energy) is only 60% that of the random structure at 200K above the temperature of the order-disorder transition.

Short-range order affects the site energy distribution ($\sigma_{\Delta E_{site}}$ in the random limit, as in **Figure 4-2**(b)-(i)) by reducing the spread of local environments around Li sites. As a result, the voltage slope is expected to decrease, with a stronger effect expected in compounds that have a large site energy distribution (i.e. low-voltage compounds). To illustrate this, **Figure 4-5**(b)-(c) show the voltage profile of $LiTiO_2$ and $LiMnO_2$ in the fully disordered and short-range ordered cases, as obtained from Monte Carlo annealing (octahedral Li insertion only). $LiTiO_2$ has a much larger voltage slope in the disordered form than $LiMnO_2$ (cf **Figure 4-5**(a)). Consequently, **Figure 4-5**(b)-(c) demonstrate that the voltage slope decrease upon cation disorder is also more pronounced for $LiTiO_2$ (slope decrease of 0.8V) than for $LiMnO_2$ (slope decrease of 0.25V).

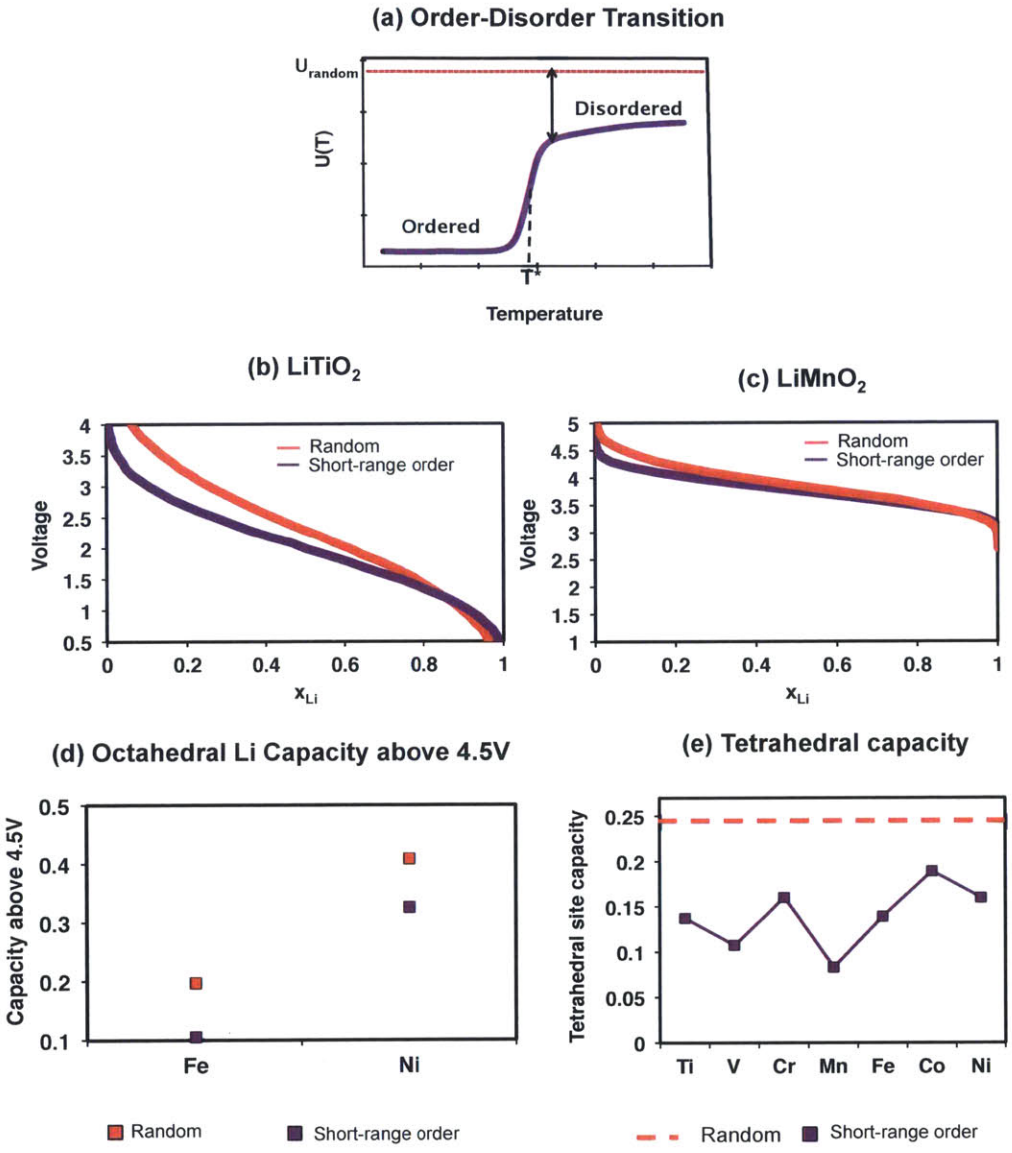

Figure 4-5: Effect of short-range order on the voltage profile of disordered $LiMO_2$ **(a)** Order-disorder transition at high temperature leads to a disordered but not fully random $LiMO_2$ structure **(b)-(c)** Voltage profiles of $LiTiO_2$ and $LiMnO_2$ equilibrated at temperatures larger than the order disorder-transition temperature **(d)** Capacities above 4.5V for fully disordered and short-range ordered high-voltage $Li(Fe,Ti)O_2$ compounds **(e)** Comparison of tetrahedral Li capacity in fully disordered and short-range ordered $LiMO_2$ compounds.

Figure 4-5(d) shows the octahedral Li capacity above 4.5V for fully disordered and short-range ordered high-voltage Li(Fe, Ni)O_2, as obtained from Monte Carlo annealing. Fully disordered Li(Fe,Ni)O_2 respectively exhibit ~0.2 and ~0.4 formula units of Li above 4.5V. Note that other high-voltage Li(Cr,Mn,Co)O_2 compounds have minimal capacity above 4.5V even in the fully random limit (<0.07 f.u.) and are not illustrated in the figure. It is found that short-range order results in ~0.1 additional f.u.'s of Li available below 4.5V in disordered $LiFeO_2$ and $LiNiO_2$. Short-range order also decreases the accessible tetrahedral Li capacity with respect to fully disordered compounds for all transition metals. While 25% of the total capacity is accounted for by tetrahedral Li occupancy in fully disordered (i.e. random) $LiMO_2$, it accounts for only 8-18% in thermally disordered compounds (**Figure 4-5**(e)). In general, short-range order therefore leads to more Li capacity accessible below the stability limit of the electrolyte in high-voltage transition metal oxides.

4.3.4 Effect of Li-excess on tetrahedral capacity

The previous sections have demonstrated that tetrahedral Li capacity can play an important role in determining the high voltage capacity of cation-disordered rocksalts. In practice, cation-disordered rocksalts require Li-excess ($y \approx 0.2$ in $Li_{1+y}M_{1-y}O_2$) to sustain macroscopic Li diffusion.[15,75] An important question that needs to be answered is therefore how Li-excess affects the relative octahedral and tetrahedral Li capacity in disordered Li-excess rocksalts.

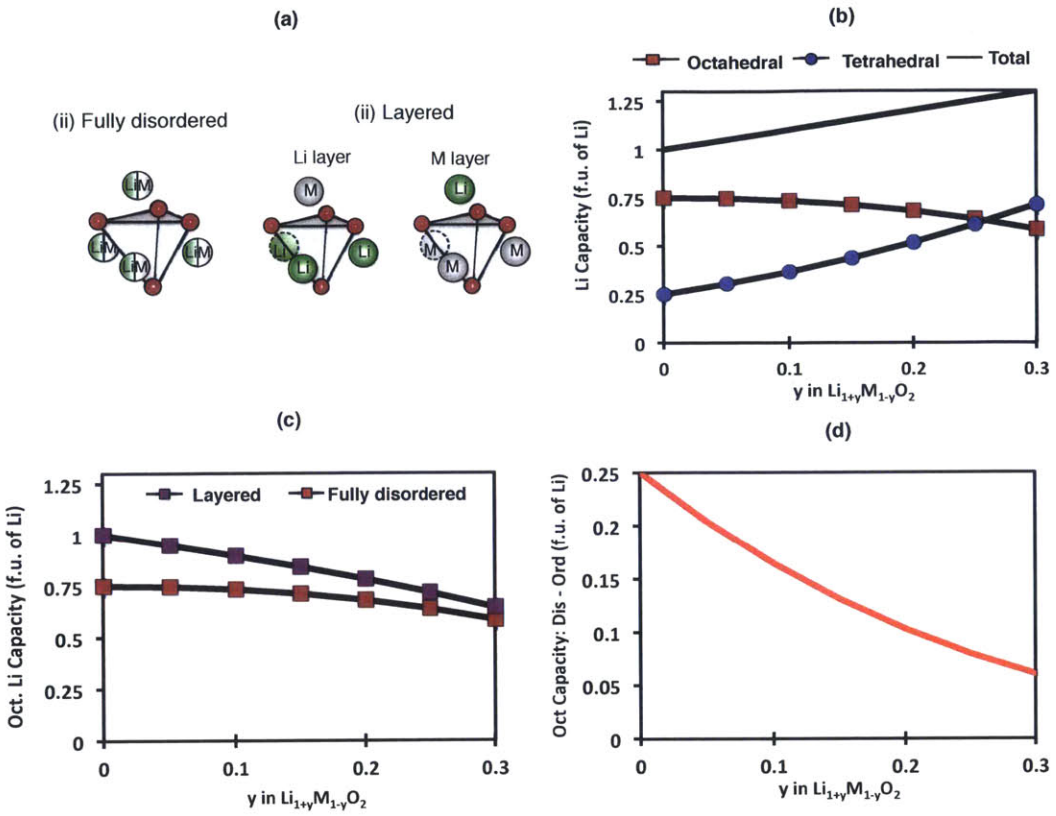

Figure 4-6: Effect Li-excess on the octahedral and tetrahedral Li capacity in layered and fully disordered $Li_{1+y}M_{1-y}O_2$ **(a)** Tetrahedral environments in fully disordered and layered $LiMO_2$ **(b)** Breakdown of the octahedral, tetrahedral and total Li capacity in fully disordered $Li_{1+y}M_{1-y}O_2$ **(c)** Octahedral Li capacity as a function Li-excess for layered and fully disordered $Li_{1+y}M_{1-y}O_2$ **(d)** Octahedral capacity lost upon full disorder in $Li_{1+y}M_{1-y}O_2$

Figure 4-6(b) shows the breakdown of octahedral and tetrahedral Li capacity in a fully disordered rocksalt, as a function of the Li-excess level (y in $Li_{1+y}M_{1-y}O_2$). In the absence of Li-excess ($y=0$), octahedral capacity accounts for 0.75 formula units (f.u.) of Li in a fully disordered $LiMO_2$ rocksalt, while tetrahedral capacity accounts for 0.25 f.u. of Li. As the Li-excess level is increased, the probability for a given tetrahedral site to be a zero-TM site

increases. The absolute capacity resulting from tetrahedral occupation in the presence of Li-excess can be obtained by performing the substitution $\frac{1}{2} \rightarrow \frac{1+y}{2}$ in equation (49) (the probability for a given cation site to be occupied by Li is $\frac{1+y}{2}$ in fully disordered $Li_{1+y}M_{1-y}O_2$). The result is given in equation (50):

$$\text{Tetrahedral Capacity}\left(\text{fully-disordered } Li_{1+y}M_{1-y}O_2\right) = 4\left(\frac{1+y}{2}\right)^4 \quad (50)$$

While the capacity resulting from tetrahedral Li occupancy increases, the total Li content in the compound also increases $(1+y)$. The octahedral capacity in a fully disordered $LiMO_2$ compound therefore decreases slower than the rate of increase of the tetrahedral capacity. The expression of the octahedral capacity at a given Li-excess level is given in equation (51) and the numerical values are illustrated in **Figure 4-6**(b).

$$\text{Octahedral Capacity}\left(\text{fully-disordered } Li_{1+y}M_{1-y}O_2\right) = (1+y) - 4\left(\frac{1+y}{2}\right)^4 \quad (51)$$

The octahedral capacity in a fully disordered $Li_{1.2}M_{0.8}O_2$ compound ($y=0.2$) is smaller than the octahedral capacity in a fully disordered $LiMO_2$ compound by only 0.07 f.u. of Li (**Figure 4-6**(b)). Based on this analysis, to cycle 1 f.u. of Li in a fully disordered $Li_{1.2}M_{0.8}O_2$ compound (~280 mAh/g), about ~90 mAh/g is expected to originate from tetrahedral Li sites.

Furthermore, the amount of octahedral Li capacity lost upon cation disorder decreases as the Li-excess level increases. To show this, we calculate the octahedral capacity in layered $Li_{1+y}M_{1-y}O_2$ and compare it with the octahedral capacity previously obtained for fully-disordered $Li_{1+y}M_{1-y}O_2$. In a layered $Li_{1+y}M_{1-y}O_2$ compound, one layer is entirely filled by Li, and the remaining *y* formula units of Li are distributed in the transition metal layer. In this work, we make the approximation that excess Li is randomly distributed in the transition metal layer, such that the probability for a cation site in the M layer to be occupied by Li is simply equal to *y*. (It is to be noted, however, that the exact structure of layered Li-excess compounds is an object of intense debate in the literature.[28,101] The disappearance of superstructure peaks after the first charge of layered $Li_{1+y}M_{1-y}O_2$,[101] however, suggests that a random distribution of Li site is a reasonable approximation.)

Because of Li-excess, some tetrahedral sites will respect the 0-TM condition even in the absence of cation disorder. Tetrahedral sites in the Li layer, which are coordinated by 3 Li and 1 M in the stoichiometric form, have a probability $P(0-TM)=(1)^3(y)$ to respect the 0-TM condition in the presence of Li-excess. Tetrahedral sites in the M layer, which are coordinated by 1 Li and 3 M in the stoichiometric form, have a probability $P(0-TM)=(1)(y)^3$ to respect the 0-TM condition in the presence of Li-excess. The total tetrahedral capacity in layered $Li_{1+y}M_{1-y}O_2$ is therefore given by:

$$\text{Tetrahedral Capacity}\left(\text{layered } Li_{1+y}M_{1-y}O_2\right)=2\left[(1)^3(y)+(1)(y)^3\right] \qquad (52)$$

Note that the factor of 2 accounts for the fact that there are two tetrahedral sites per cation site. Finally, the octahedral capacity in layered $Li_{1+y}M_{1-y}O_2$ is:

$$\text{Octahedral Capacity}\left(\text{layered } Li_{1+y}M_{1-y}O_2\right) = (1+y) - 2\left[(1)^3(y) + (1)(y)^3\right] \qquad (53)$$

Figure 4-6(c) compares the octahedral capacity in layered and fully disordered $Li_{1+y}M_{1-y}O_2$ (via equations (51) and (53)). In both cases, the octahedral capacity decreases with Li-excess. But interestingly, the difference in octahedral capacity between the layered and the fully disordered structure also decreases with the amount of Li-excess. This is illustrated in **Figure 4-6**(d), which shows the octahedral capacity lost upon full disorder of an initially layered structure as a function of Li-excess. While 0.25 f.u. of octahedral capacity is lost to tetrahedral sites upon full disorder in layered $LiMO_2$, only 0.1 f.u. of Li is lost to tetrahedral sites upon disorder in layered $Li_{1.2}M_{0.8}O_2$. This suggests that Li occupancy of tetrahedral sites is a general feature of Li-excess materials, regardless of the amount of cation disorder. The voltage slope increase resulting from the availability of additional tetrahedral Li sites upon disorder is therefore expected to be less pronounced in Li-excess compounds than in stoichiometric compounds.

4.4 Summary and Discussion

This work demonstrated that the voltage slope of cation-disordered rocksalts is a combination of the Li site energy distribution (controlled by Li-M interactions), the effective Li-Va interaction and the occupancy of tetrahedral sites by Li. It was found that the voltage slope

increase upon disorder is generally smaller for high-voltage transition metals than for low-voltage transition metals. Short-range order in practical disordered compounds was found to reduce the voltage slope with respect to fully random structures by narrowing the width of the site energy distribution as well as via a decrease in the availability of tetrahedral sites. Finally, it was found that the additional tetrahedral capacity resulting from disorder is smaller in Li-excess compounds than in stoichiometric compounds.

The inverse correlation between the average voltage and the voltage slope increase upon disorder (**Figure 4-4**(c)) is beneficial for the design of high-capacity disordered rocksalts, as a high average voltage and a moderate voltage slope are simultaneously desirable to access a maximum of capacity at high voltage. This trend can be attributed to the site energy contribution to the voltage slope (**Figure 4-4**(b), controlled by the effective Li-M interaction) and can be qualitatively explained by the relative positions of the transition metal 3d bands and the oxygen 2p bands. As the atomic number of the transition metal increases, the energy of the metal 3d band decreases, resulting in a higher average voltage (higher $M^{3+/4+}$ extraction energy).[86] Simultaneously, as the energy difference between the metal 3d and oxygen 2p bands decreases, the bonds between transition metal and oxygen atoms become more covalent, leading to a more effective screening of the $M^{3+/4+}$ charge by oxygen electrons.[86] This more effective screening reduces the energy dependence of Li on its environment, as the energy difference between Li sites with a large number of transition metal neighbors (resulting in high electrostatic repulsion between Li^{3+} and $M^{3+/4+}$ cations) and Li sites with a small number of transition metal neighbors (resulting in low electrostatic repulsion) decreases (cf **Figure 4-2**(b)-(i)). This in turn leads to a decrease in the voltage slope.

This inverse correlation is consistent with the limited amount of electrochemical data currently available on cation-disordered rocksalts. The only disordered rocksalt that has been partially cycled in the $LiMO_2$ family is disordered $LiTiO_2$, which is formed *in situ* during cycling of rutile TiO_2.[78,79] Particle nano-sizing allows for small diffusion lengths (as low 10 nm[78,79]), which partially compensate for the poor diffusivity of Li in stoichiometric disordered $LiMO_2$ rocksalts.[15,75] After first discharge, during which disordered $LiTiO_2$ is formed, the voltage profile changes and the voltage range upon cycling of 200 mAh/g of Li ($LiTiO_2$ <=> $Li_{0.4}TiO_2$) is found to be on the order of 2V.[78,79] The voltage range measured in this compound cannot provide a reliable reference for the open circuit voltage slope of disordered $LiTiO_2$, as only 60% of the capacity can be cycled and as significant hysteresis is present in the voltage profile. Nevertheless, this large voltage slope is in qualitative agreement with our predictions for $LiTiO_2$ (2.9V slope for octahedral Li insertion in fully disordered $LiTiO_2$). Another low voltage system that undergoes a single redox step, $Li_{1+x}VO_3$ ($V^{4+/5+}$),[16] cycles 1 f.u. of Li in a ~1.5V voltage range (based on the discharge data), at an average voltage of ~2.5V . On the other hand, higher voltage redox such as the $Ni^{2+/3+}$ in $Li_{1.2}Ni_{0.33}Ti_{0.33}Mo_{0.14}O_2$ [17] and the $M^{3+/4+}$ or $M^{2+/4+}$ redox in $Li_{1.3}Nb_yM_xO_2$ (M=Mn, Fe, Co, Ni)[18] all occur in a voltage range smaller or equal to 1V (based on the first charge data). These observations agree with the predicted inverse correlation between the average voltage and the voltage slope of cation-disordered compounds. Interestingly, within the $Li_{1.3}Nb_yM_xO_2$ family (M=Mn, Fe, Co, Ni), it can be observed that the transition metals with the lowest average voltage also have the largest voltage slope, and vice-versa (based on the transition metal redox as observed on first charge).[18]

With the exception of Ni, our model predicts that octahedral Li occupancy in high-voltage $LiMO_2$ (Cr, Mn, Fe, Co) does not result in significant capacity above the stability limit of the

electrolyte (~4.5-4.7V). This is largely due to the smaller spread of site energies in high-voltage transition metals. However, the availability of tetrahedral site upon delithiation contributes to a high-voltage region at the end of charge. By estimating the stabilization resulting from tetrahedral Li occupancy by the corresponding stabilization in the stoichiometric spinel structure, we find that the voltage increase at the end of charge resulting from tetrahedral Li extraction is on the order 0.3V-0.5V and accounts for 25% of the total capacity in fully disordered $LiMO_2$. This investigation therefore highlights the importance of tetrahedral capacity to the voltage profile of cation-disordered high-voltage transition metal oxides.

In practice however, cation-disordered rocksalts are not fully random. This was demonstrated for temperature-driven cation disorder of $LiMO_2$ compounds, where the energy of the disordered state is smaller than that of the fully random structure. Short-range order decreases the voltage slope with respect to random cation occupation, by reducing the spread of local transition metal environment around Li sites as well as by decreasing the number of tetrahedral sites accessible upon delithiation. Short-range order is therefore an important parameter for the design of high-voltage cation-disordered rocksalts. The synthesis of partially disordered compounds, for example, could both leverage the benefits of disordered rocksalts (high mobility at the top of charge) while minimizing the voltage slope increase upon disorder.

In practice, cation-disordered rocksalts require Li-excess to sustain macroscopic diffusion ($y \approx 0.2$ in $Li_{1+y}M_{1-y}O_2$).[10,15] The effect of Li-excess on the relative amount of octahedral and tetrahedral Li capacity was studied using probability theory. While the absolute amount of available tetrahedral sites increases upon introduction of Li-excess, the amount of octahedral capacity lost upon cation disorder decreases with the amount of Li-excess. This suggests that

the Li occupancy of tetrahedral sites is a general feature of Li-excess materials, regardless of the amount of cation disorder. The voltage slope increase resulting from additional availability of tetrahedral sites upon cation disorder is therefore expected to be minimal in Li-excess systems.

4.5 Conclusion

In this Chapter, we developed a model based on first principles to evaluate the voltage slope of stoichiometric cation-disordered lithium transition metal oxides. Our study demonstrated that high-voltage transition metals generally have a lower voltage slope than low-voltage transition metals and therefore have minimal Li capacity above the electrolyte stability limit (with the exception of $LiNiO_2$, which has a high average voltage in its disordered form). Cation disorder however leads to occupation of tetrahedral sites by Li, sites which are otherwise inaccessible in the stoichiometric layered structure. The availability of tetrahedral Li sites results in an additional high-voltage region outside the stability range of the electrolyte and can significantly affect the accessible capacity upon cycling.

Short-range order in practical disordered compounds mitigates the voltage slope increase by reducing the amount of local environments around Li sites, as well as by decreasing the availability of tetrahedral sites. Furthermore, the amount of octahedral capacity lost upon disorder decreases with the introduction of Li-excess, which is required to enable macroscopic diffusion in disordered rocksalts. Our work therefore provides critical insights for the design of high-capacity Li-excess cation-disordered rocksalts based upon voltage considerations.

4.6 Appendix

4.6.1 Pair term approximation for ΔE_{site}

The validity of the pair term approximation for the site energy distribution can be evaluated by considering the effect of higher-order interactions (i.e. triplet and quadruplet ECI's) on the site energy distribution. The standard deviation of the probability distribution $P(\Delta E_{site})$ can be obtained by fitting binary cluster expansions of higher complexity in the $LiMO_2$ and MO_2 limits (respectively for Li/M and V/M disorder) and using a Monte Carlo method to assess the standard deviation of the site energy, $\sigma_{\Delta E_{site}}$. This Monte Carlo method consists in calculating the energy for full Li extraction in randomly populated large supercells containing N formula units of $LiMO_2$ ($\left(E_{LiMO_2}-E_{MO_2}\right)_{\text{supercell}}$). This is equivalent to sampling the sum of N statistically independent site energies. $\sigma_{\Delta E_{site}}$ can then be obtained via the relation .

$$\sigma_{\Delta E_{site}} = \sqrt{\frac{Var\left(E_{LiMO_2}-E_{MO_2}\right)_{\text{supercell}}}{N_{Li}}} \tag{54}$$

The slope of the voltage profile can be estimated by assuming a Gaussian distribution. In this case, the voltage slope and the standard deviation are related by:

$$\left.\frac{dV}{dx_{Li}}\right|_{x_{Li}=0.5} = \sqrt{2\pi}\sigma_{\Delta E_{site}} \tag{55}$$

The cross-validation score of the $LiMO_2$ and MO_2 cluster expansions are such that the average voltages of the input $LiMO_2$ structures that are used to perform the fit is between 0.08V-1.2V, depending on the transition metal. The standard deviation, being a statistical quantity over a large number of local environments, is however predicted with higher accuracy than the voltage of a given structure. By performing multiple cluster expansions on the same systems, we find that the uncertainty on $\sigma_{\Delta E_{site}}$ is at most on the order ±0.06V. Using the Gaussian scaling in equation (55), we find that the uncertainty on the predicted voltage slope is ~ ±0.15V. We find that the pair term model correctly predicts the (site energy induced) voltage slope of fully disordered $LiMO_2$ to within 0.2V, resulting in a satisfying uncertainty of 0.1V at high voltage (the voltage range being given by $\left[\overline{\Delta V}-\frac{Slope}{2},\overline{\Delta V}+\frac{Slope}{2}\right]$) **(Figure 4-7)**.

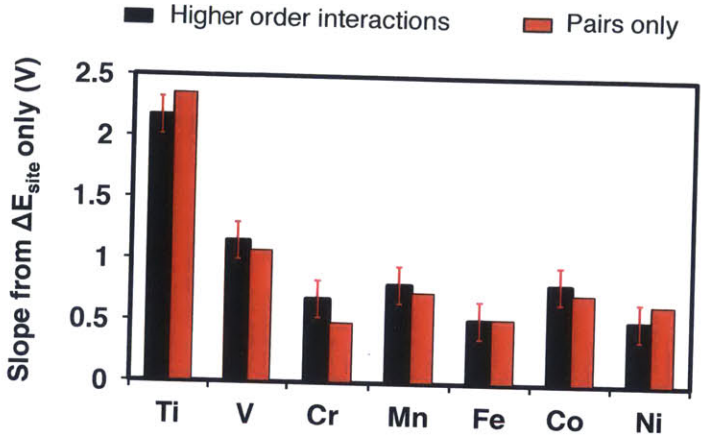

Figure 4-7: Accuracy of the pair term approximation for fully disordered $LiMO_2$. The black columns constitute the site energy induced slope using higher order interactions, while the red columns show the corresponding predictions by only considering pair terms.

4.6.2 Determining ΔV^{tet} from the spinel structure

We estimate the additional voltage step induced by tetrahedral Li occupancy (ΔV^{tet} in **Figure 4-2**(c)) based on the spinel structure (**Figure 4-8**). The topology of the spinel structure is such, that at $x_{Li}=0.5$, all Li atoms occupy 0-TM tetrahedral sites. Tetrahedral Li occupancy therefore induces a high-voltage region in the $x_{Li}=[0, 0.5]$ range. Using Density Functional Theory, we can compare the voltage plateau arising from tetrahedral occupancy with the voltage plateau arising from octahedral Li occupancy in the same concentration range. The difference between these two voltage plateaus can be used to estimate of the voltage slope increase in disordered rocksalts resulting from tetrahedral Li occupancy .

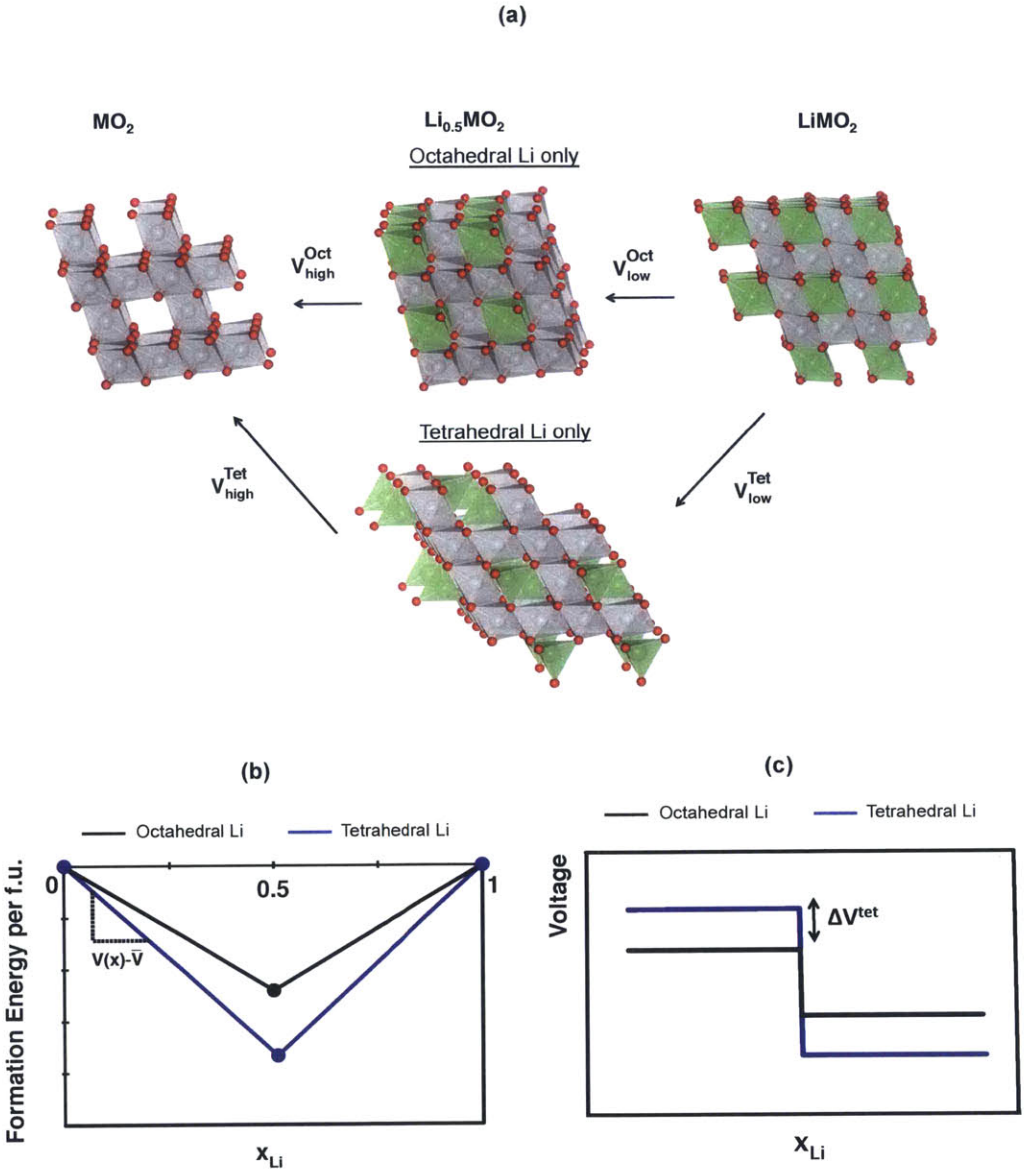

Figure 4-8: Estimating the voltage increase resulting from tetrahedral Li occupancy (ΔV^{tet} in **Figure 4-2**(c)) using the spinel structure. **(a)** Delithiation of the spinel $LiMO_2$ structure along the tetrahedral and octahedral pathways (Li is green, M is gray and O is red) **(b)** Energy hull of spinel $LixMO_2$ along the tetrahedral and octahedral pathways (x_{Li}=0, 0.5, 1) **(c)** The difference

in the high voltage step of the octahedral and tetrahedral pathways, labeled ΔV^{tet} in the plot, is used to estimate the scale of the voltage increase at the end of charge in disordered structures resulting from tetrahedral Li occupancy (ΔV^{tet} in **Figure 4-2**(c)).

Chapter 5 :

Thermodynamic Stability of Intermediate Solid Solutions in $LiFePO_4$ nano-particles

5.1 Introduction

$LiFePO_4$ is an important commercial cathode material for Li-ion batteries due to its safety,[30] reasonable energy density (170 mAh/g, 3.4 V vs. Li/Li^+),[31] and high-rate capability.[36-40] Capacities as high as 130 mAh/g have been achieved at a 50 C rate (where n C corresponds to full (dis)charge in $1/n$ hours), and rates as high as 200 C and 400 C have been achieved by removing kinetic limitations at the electrode level. These high rates are accessible only when the particle size is reduced to the nano-scale (~50-100 nm), a limitation that has been attributed to reduced Li mobility due to channel-blocking anti-site defects that are present in larger particles.[35,41,42] However, the mechanism by which pristine nano-sized particles achieve high rates given their equilibrium two-phase behavior ($Li_xFePO_4 \rightarrow xLiFePO_4 + (1-x)FePO_4$) is still an object of debate in the $LiFePO_4$ research community.

Early lithiation models of $LiFePO_4$ single particles predicted lithiation to be initiated by a

nucleation event[31,43-46] followed by two-phase growth along the elastically favorable crystallographic *bc* plane.[45,46] However, while nucleation can occur during chemical delithiation due to the high overpotentials associated with the chemical reagents (~1.5V[102]), overpotentials in practical electrochemical conditions are much lower and thus unlikely to provide enough driving force to overcome the nucleation barrier required to form the critical nucleus.[47] (Overpotentials as low as 20mV are sufficient to cycle entire electrodes[48]).

A solution to the apparent discrepancy between the high-rate capabilities and the the two-phase nature of $LiFePO_4$ was first proposed by Malik et al.[47,49] Using Density Functional Theory (DFT), the authors identified a non-equilibrium solid-solution pathway accessible at low overpotentials (~30mV), which circumvents the kinetically prohibitive nucleation step and enables homogeneous lithiation at low overpotentials. Since then, with the development of advanced *in situ* characterization techniques, the presence of solid-solution states during electrochemical (de)lithiation has been experimentally demonstrated. Several *in situ* X-Ray Diffraction (XRD) experiments have identified lattice parameters intermediate to those of the equilibrium $FePO_4$ and $LiFePO_4$ phases, at (dis)charge rates varying from 0.1 C to 60 C.[50-53] A recent *in situ* Transmission Electron Microscopy (TEM) experiment has also observed a ~20 nm solid-solution zone in micron-sized $LiFePO_4$ nanowires.[103] It has therefore clearly been established that solid-solution states can play, in various forms, a critical role in the electrochemical (de)lithiation of single $LiFePO_4$ particles.

A key mystery that remains to be elucidated, however, is the persistence of solid-solution states in single particles at *low-to-moderate* C-rates, (for example, rates in the 0.1 C - 5 C range). First principles calculations performed in this chapter indeed show that homogeneous solid-

solution states are thermodynamically unfavorable over two-phase coexistence in particles larger than 10 nm. Moreover, due to the concave shape of the non-equilibrium solid-solution free energy, homogeneous solid-solution states are unstable with respect to small inhomogeneities in Li concentration. As a particle takes up Li at a fixed current, Li can rapidly diffuse to form a two-phase state inside the particle so as to minimize the particle's free energy. Considering the high diffusivity of Li in $LiFePO_4$ ($D \sim 10^{-8}$-10^{-10} cm^2/s, from Density Functional Theory[34] and muon-spin relaxation[54] respectively), Li diffusion in a 100 nm particle can occur on time scales as rapid as 1-100 ms, [b] which is much faster than the typical time required to lithiate a single particle. At 5 C, for example, (de)lithiation of a single particle occurs in 720 s, which is much larger than the 1-100 ms time-scales required for phase-separation through Li diffusion. Even correcting for the fact that not all particles are simultaneously active in the electrode (a recent experiment has demonstrated that, at a 5 C rate, only ~30 % of the particles in an electrode are actively taking up Li at a given time[104]), the time required to (de)lithiate a single particle is still much larger than the time required for phase separation. In summary, while each particle is expected to initiate (de)lithation through a non-equilibrium solid solution, it remains surprising that homogeneous solid-solution states could persist at low-to-moderate C-rates despite their thermodynamic instability.

In this chapter, we propose that the persistence of solid-solution states during the (dis)charge of $LiFePO_4$ electrodes at low-to-moderate C-rates is *thermodynamic* in origin. Using first principles calculations, we demonstrate that spinodal decomposition from a homogeneous solid

[b] These values were obtained using Fickian scaling $t \sim r^2/D$, with the theoretical and experimental values of D provided above.

solution through Li diffusion is more likely to lead to the formation of an *ac* interface, rather than the elastically favored *bc* interface. As a result of the high coherency strain energy associated with a sharp *ac* interface, we further demonstrate that a driving force exists to form a large intermediate solid solution region at the interface, *whose dimensions are proportional to the size of the particle* (~25%-50% of the particle volume depending on the particle morphology). Our results not only rationalize the observation of intermediate lattice parameters at low-to-moderate C-rates in $LiFePO_4$ electrodes, but also explain the observations of stable intermediate solid-solution states at an *ac* interface in single particles quenched from a high-temperature solid solution.[105,106]

5.2 Methodology

We consider a single (Li)$FePO_4$ particle which, upon application of an over(under)potential, initiates Li (de)intercalation through the non-equilibrium solid-solution pathway (**Figure 5-1**(a)-(i)). Once the Li concentration surpasses the spinodal point, homogeneous solid-solution states become unstable against infinitesimally small fluctuation in Li concentrations due to the negative curvature of the solid-solution free energy curve in that concentration range (**Figure 5-1**(a)-(ii)). Such inhomogeneities are bound to occur during (dis)charge, as concentration gradients develop at the particle surface due to the applied current. In the presence of such inhomogeneities, uphill Li diffusion occurs from regions of low Li concentration to regions of high Li concentration, leading to phase separation (**Figure 5-1**(a)-(iii)). In practice, the final state of the particle after spinodal decomposition may not involve a sharp interface but rather a diffuse interface. The presence of an intermediate solid-solution region at the interface facilitates the reduction of the coherency strain energy and chemical interfacial energy

penalties of a sharp interface at the expense of a higher bulk energy (**Figure 5-1**(b)). The width of the intermediate solid-solution region at thermodynamic equilibrium depends on the ratio between the bulk free energy of the solid solution and the coherency and chemical interfacial energies of the interface orientation that is formed after spinodal decomposition.

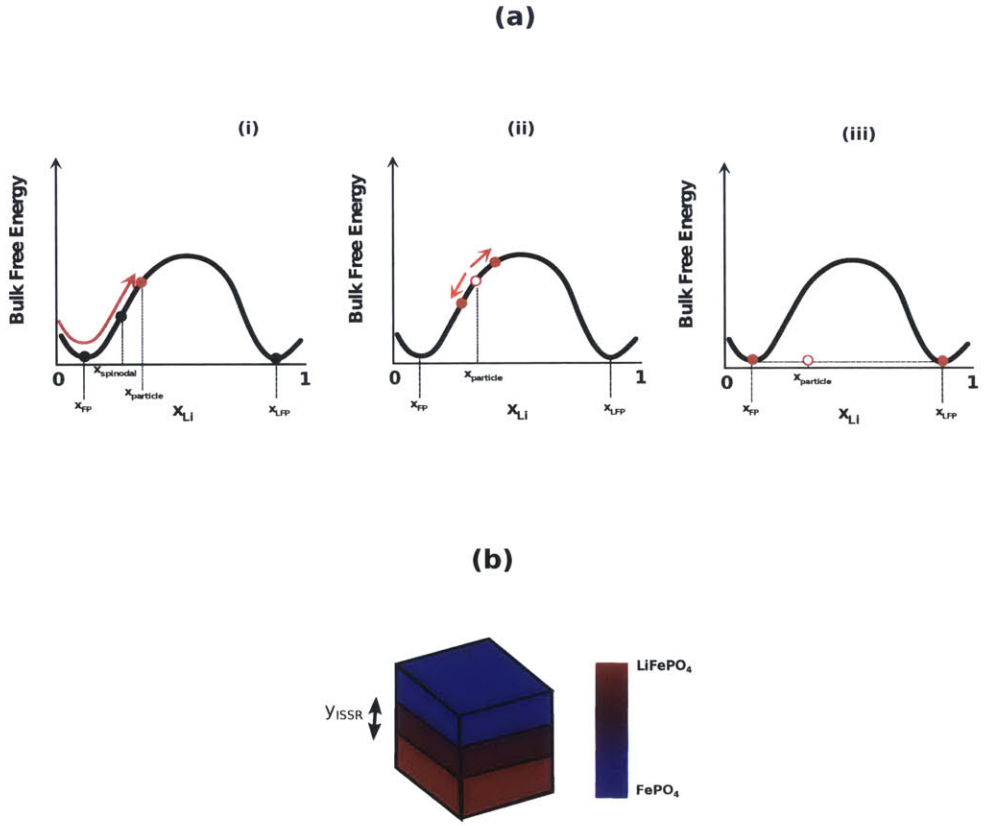

Figure 5-1: **(a)** Particle initiating lithiation through a non-equilibrium solid-solution pathway and subsequently relaxing to a two-phase state. **(b)** The final state after spinodal decomposition consists in a $LiFePO_4$ region, a $FePO_4$ region, and potentially and intermediate solid-solution region (ISSR), with a volume fraction y_{ISSR}.

In this chapter, we determine the free energy and topology (i.e. the symmetry of the low energy Li-Va orderings) of the non-equilibrium solid-solution pathway from first principles. Given the topology of the non-equilibrium solid-solution pathway and the 1D character of Li diffusion, we demonstrate that spinodal decomposition from a homogeneous solid-solution state preferentially leads to the formation of an *ac* interface, instead of the commonly assumed *bc* interface. By combining first principles calculations and continuum elasticity, we further demonstrate that a large intermediate solid-solution region at an *ac* interface is thermodynamically favorable over a sharp *ac* interface, as it reduces the high coherency strain energy penalty associated with a sharp *ac* interface. The following paragraphs present this approach in more details.

The free energy of the non-equilibrium solid-solution pathway is estimated by finding the lowest-energy solid-solution configurations that form a topotactic lithiation pathway between $FePO_4$ and $LiFePO_4$. To this end, a large number of Li-Va orderings are calculated within the Generalized Gradient Approximation (GGA(PBE)+U) to Density Functional theory (DFT), as implemented in the Vienna Ab Initio Simulation Package (VASP). A self-consistent U value for Fe of 4.3 is used,[62] with an energy cutoff of 520 eV and a k-points mesh density of one k-point per 0.04 A^{-1}. All calculations are performed in the ferromagnetic state, following previous studies.[107]

The driving force to form an intermediate solid-solution region at a $LiFePO_4/FePO_4$ interface is calculated using the setup illustrated in **Figure 5-1**(b). Three regions are defined in the particle: a $LiFePO_4$ region, a $FePO_4$ region and a Li_xFePO_4 solid- intermediate solution region (ISSR) with volume fraction y_{ISSR}. The free energy penalty to form a sharp interface ($y_{ISSR} = 0$) is the sum of its coherency strain energy and chemical interfacial energy penalties:

$$F_{sharp\ boundary} = Ve_{strain}^{sharp\ boundary} + A\gamma \tag{56}$$

Where V is the particle volume, $e_{\text{strain}}^{\text{sharp boundary}}$ is the volume-averaged coherency strain energy density in the particle (resulting from a sharp interface), A is the interfacial area and γ is the chemical interfacial energy.

The free energy penalty for the creation of a diffuse interface is the sum of the bulk free energy of the ISSR, the coherency strain energy resulting from the presence of a diffuse interface and the gradient energy penalty in the ISSR:

$$F_{diffuse\ boundary} = Vy_{ISSR}\overline{f}_{solid-solution} + Ve_{strain}^{diffuse\ boundary} + \int_{V_{ISS}} k\left|\nabla x_{Li}\right|^2 dV \tag{57}$$

where y_{ISSR} is the volume fraction of the ISSR, $\overline{f}_{solid-solution}$ is the volume-averaged bulk free energy density in the ISSR, $e_{strain}^{diffuse\ boundary}$ is the volume-averaged coherency strain energy density in the particle resulting from a diffuse boundary, κ is the gradient energy coefficient and ∇x_{Li} is the concentration gradient in the ISSR. The difference in free energy between a diffuse interface and a sharp two-phase boundary ($y_{ISSR} = 0$) is obtained by taking the difference between equation (57) and equation (56) :

$$F_{diffuse\ boundary} - F_{sharp\ boundary} = Vy_{ISSR}\overline{f}_{solid-solution} + V\left(e_{strain}^{diffuse\ boundary} - e_{strain}^{sharp\ boundary}\right) + \left(\int_{V_{ISSR}} k\left|\nabla x_{Li}\right|^2 dV - A\gamma\right) \quad (58)$$

The first term represents the bulk free energy penalty to form the ISSR (positive), the second represents the decrease in coherency strain energy in forming a diffuse interface (negative) and the third term represents the decrease in chemical interfacial energy in forming a diffuse interface (negative). The range of y_{ISSR} for which $F_{diffuse\ boundary} - F_{sharp\ boundary}$ is negative constitutes the range of ISSR volume fraction for which intermediate solid solutions are thermodynamically favorable over a sharp interface. The equilibrium thermodynamic value of y_{ISSR} (valid in the limit of zero rates) can be evaluated by minimizing equation (58) with respect to y_{ISSR}. This equilibrium value is denoted by $y_{ISSR,eq}$.

Coherency strain energy values for the sharp boundary and diffuse boundary cases are calculated by numerically solving the equation of continuum elasticity for coherent interfaces under a traction-free boundary condition (cf Chapter 2). Chemical interfacial energies are obtained from first principles (cf Chapter 2), and the associated gradient energy penalty term is calculated from the well-known relation:[108]

$$\kappa = \frac{\gamma^2 \Omega_{Li}}{\overline{f_{ss}}} \quad (59)$$

where γ is the chemical interfacial energy, Ω_{Li} is the volume per formula unit and $\overline{f_{ss}}$ is the average value of the solid-solution free energy (per formula unit) in the $x_{Li} = [0,1]$

concentration range.

Note that other surface-scaling effects such as the surface energy differences between a sharp interface and a diffuse interface are ignored. This approximation is justified *a posteriori*, given that the identified mechanism for the retention of intermediate solid solutions is a volumetric effect, which remains at particle sizes where surface effects are small (~200nm).

5.3 Results

Figure 5-2(a) shows the low-energy solid-solution orderings identified using Density Functional Theory. At each concentration, the lowest energy solid-solution states are comprised of a periodic arrangement of lithiated and delithiated *ac* planes, in proportion to the lithium concentration (for example, at $x_{Li} = 0.5$, one out of two *ac* planes is lithiated). In these low-energy solid-solution states, each *b*-channel in the particle is partially lithiated, contrarily to the channel-by-channel lithiation often assumed in the literature.[46,49] The maximum energy of these low-energy states is ~6 meV per formula unit (meV/f.u.), in agreement with the 700 J/mol (7 meV/f.u.) solid-solution mixing enthalpy obtained by Dodd et al. via Differential Scanning Calorimetry.[102] The overpotential required to access this solid-solution pathway can be estimated by taking the derivative $dE_{formation}/dx_{Li}$ at $x_{Li} = 0$, yielding a zero-rate overpotential of 25 mV. This overpotential is consistent with the low ~10 mV hysteresis measured in slow cycling of $LiFePO_4$ electrodes.[48]

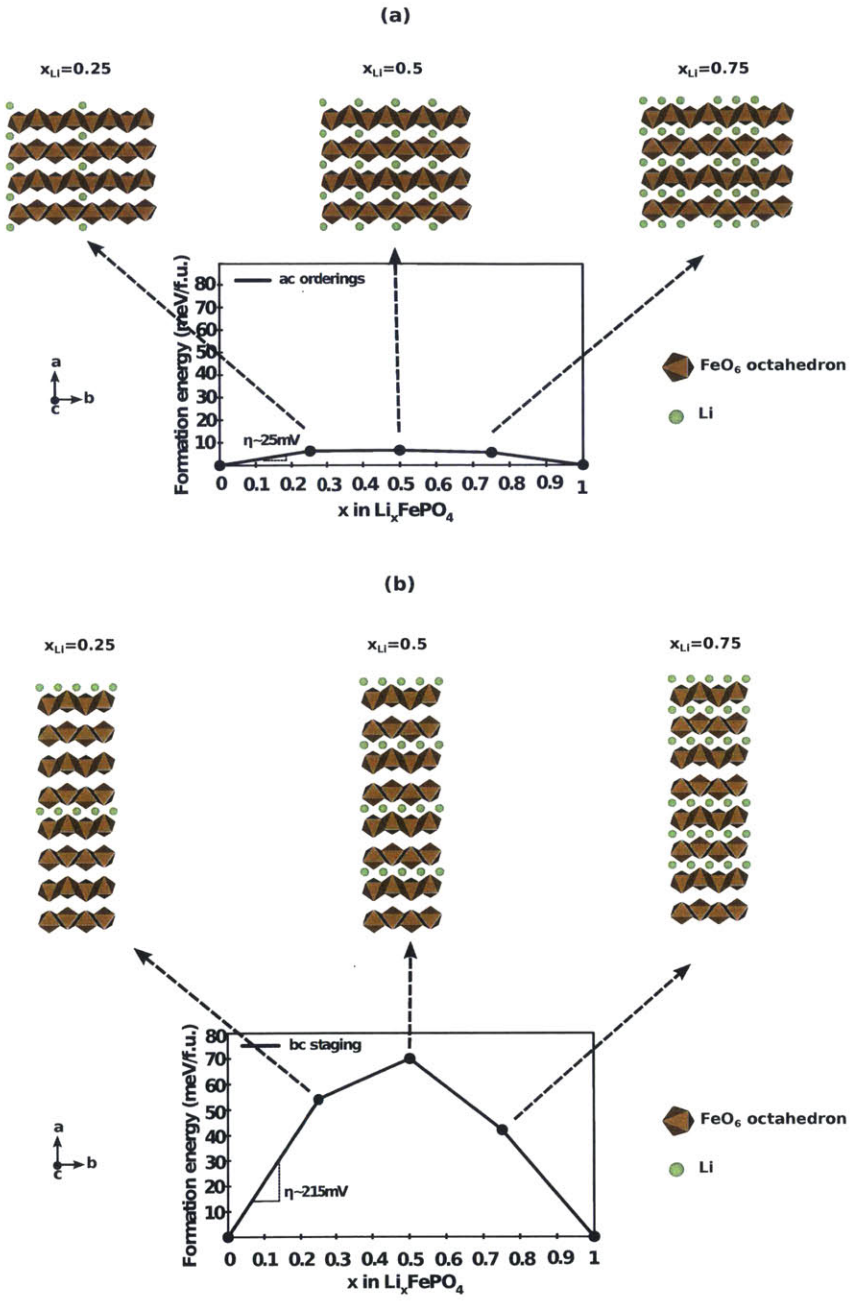

Figure 5-2: Low-energy orderings in the non-equilibrium solid-solution pathway in Li_xFePO_4, as determined by Density Functional Theory. **(a)** The non-equilibrium solid-solution pathway in Li_xFePO_4 is governed by the energetics of *ac* orderings (alternately lithiated/delithiated *ac*

planes in proportion to the Li concentration) and is accessible at low overpotentials (~25mV). **(b)** In comparison, previously reported *bc* staging configurations can only be accessed at high overpotentials (~215mV).

While the low-energy non-equilibrium solid-solution pathway (dominated by *ac* orderings) has a low bulk free energy, homogeneous solid-solution states are still thermodynamically unfavorable over two-phase coexistence in a single particle, even when the coherency strain energy and chemical interfacial energy penalties are considered. This is true for both a sharp *bc* interface (the elastically favorable interface orientation) and a sharp *ac* interface (which is observed in quenching experiments of Li_xFePO_4 solid solutions[105]). In the case of a cubic particle, the volume-averaged coherency strain energy is ~1.7 meV/f.u. for the *bc* interface and ~3 meV/f.u. for the *ac* interface,[109] which in both cases is lower than the 6 meV/f.u. bulk free energy of homogeneous solid-solution states. This is illustrated in **Figure 5-3**.

The additional contribution of chemical interfacial energy is found to be small in ~100 nm particles. Table 5-1 presents the chemical interfacial energies per unit area (excluding coherency strain energy) that were calculated using DFT.

Table 5-1 Calculated chemical interfacial energies per unit area

***bc* interface**	**ac interface**	**ab interface**
115 mJ/m^2	7 mJ/m^2	95 mJ/m^2

Our calculated values are consistent with the general order of magnitude of coherent chemical interfacial energies per unit area, which are known to be on the ~100 mJ/m^2 scale[108], with the exception of γ_{ac} which is found to be exceptionally low. The low chemical interfacial penalty

along the *ac* plane is however consistent with the low formation energy of *ac* orderings (~6 meV/f.u. at x_{Li}=0.5), which can be considered to be purely comprised of *ac* interfaces. By comparison, the "bc staging" ordering, which is can be considered to be purely comprised of *bc* interfaces, has a much higher energy of ~70 meV/f.u (**Figure 5-2**(b); note that the obtained values are in agreement with previously reported values by Zhu et al[110]). Taking into account the fact that the energy penalty for the *ac* ordering state is 10 times lower than that for the *bc* ordering, and taking into account the fact that the interfacial area per formula unit along the *ac* plane is approximately twice that along the *bc* plane (the lattice parameters approximately being $a=10.4\ A$, $b=6.1\ A$, $c=4.8\ A$ for $LiFePO_4$), a rough estimate indicates that γ_{ac} should be approximately 20 times lower than γ_{bc}. Using this ratio to calculate γ_{ac} based on the value of γ_{bc}, we find that this simple model gives an approximate value of $\gamma_{ac}=6\ mJ/m^2$, which is very close to the calculated value. The relative energies of *bc* and *ac* microscopic orderings are therefore consistent with the relative values of the *ac* and *bc* chemical interfacial energies per unit area.

Nevertheless, the additional effect of chemical interfacial energy penalty to the free energy penalty of phase-separation at typical ~100 nm particle sizes is small for any interface orientation (on the order of 0.5 meV/f.u. for a *bc* interface and 0.03 meV/f.u. for an *ac* interface) and can be neglected in when evaluating the stability of diffuse interfaces over sharp interfaces.

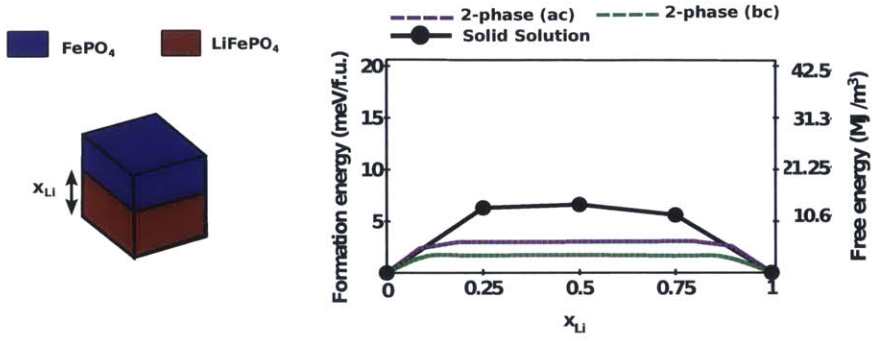

Figure 5-3: Comparing the free energy of a homogeneous solid solution with respect to the free energy of phase-separation to a sharp *bc* or *ac* interface at different Li concentrations. Since the effect of chemical interfacial energy is small for typical ~100 nm particles (0.5 meV/f.u. for a *bc* interface and 0.03 meV/f.u. for an *ac* interface), only the contribution of coherency strain energy to the energy penalty of phase-separation is considered.

In principle, spinodal decomposition can therefore lead to relaxation to either a *bc* interface or to an *ac* interface, with the *bc* interface being generally thermodynamically favorable by virtue of its lower coherency strain energy (by ~1.3 meV/f.u.). But while a driving force exists to form both interface orientations, the topology of the non-equilibrium solid-solution pathway, coupled with the constraint of 1D diffusion along the *b* direction, suggests that relaxation to an *ac* interface is much more likely. During the spinodal decomposition process, each region in the particle must indeed be dominated by local *ac* orderings in order for the bulk free energy to continuously decrease across the particle. With Li diffusion largely one-dimensional along the *b* direction, the continuous spinodal decomposition process is most likely to lead to the formation of an *ac* interface, as illustrated in **Figure 5-4**(a)-(c). Although the *bc* interface is the thermodynamically favorable interface, relaxation to a *bc* interface requires significant

diffusion in the *a* and *c* directions (**Figure 5-4**(d)), which is much slower than diffusion in the *b* direction (even with 1% Li-Fe antisite defect in the particle, D_b is larger than D_a and D_c by a factor of 1,000[42]). Moreover, relaxation to a *bc*-interface from an *ac* ordering can only occur at the expense of an initial increase in bulk free energy, since the symmetry of *ac* orderings must be broken locally (from *b*-channels being partially lithiated to some *b*-channels being fully lithiated and others being fully delithiated).

This prediction is consistent with the quenching experiment of Chen et al (**Figure 5-5**).[105] In this experiment, $LiFePO_4$ particles are chemically delithiated to $Li_{0.6}FePO_4$, producing a series of *bc* interfaces inside the particle (presumably through nucleation and growth, owing to the high overpotentials induced by chemical reagants[102]). After heating to T~200°C, a homogeneous, thermodynamically favorable solid-solution state is formed within the particle, through slow-Li diffusion along the *a* direction. After quenching to room temperature, at which homogeneous solid-solution states are thermodynamically unfavorable, spinodal decomposition occurs through Li diffusion in the *b* direction. This leads to the formation of an *ac* interface with a large intermediate solid-solution region at the interface, consisting in one or more intermediate phases. This intermediate solid-solution region is found to be indefinitely stable (stability longer than 5 months). The experiment yielded similar results for large *ac*-platelet particles (2μm x 200nm x 4μm) and intermediates-sized near-cubic particles (300nm x 200nm x 500nm). Therefore, both our first principles predictions and the quenching experiment of Chen et al.[105] demonstrate that no easily accessible topotactic pathway exists for a particle to continuously relax from a homogeneous solid solution to a *bc* interface, despite the *bc* interface generally being the thermodynamically favorable interface.[109]

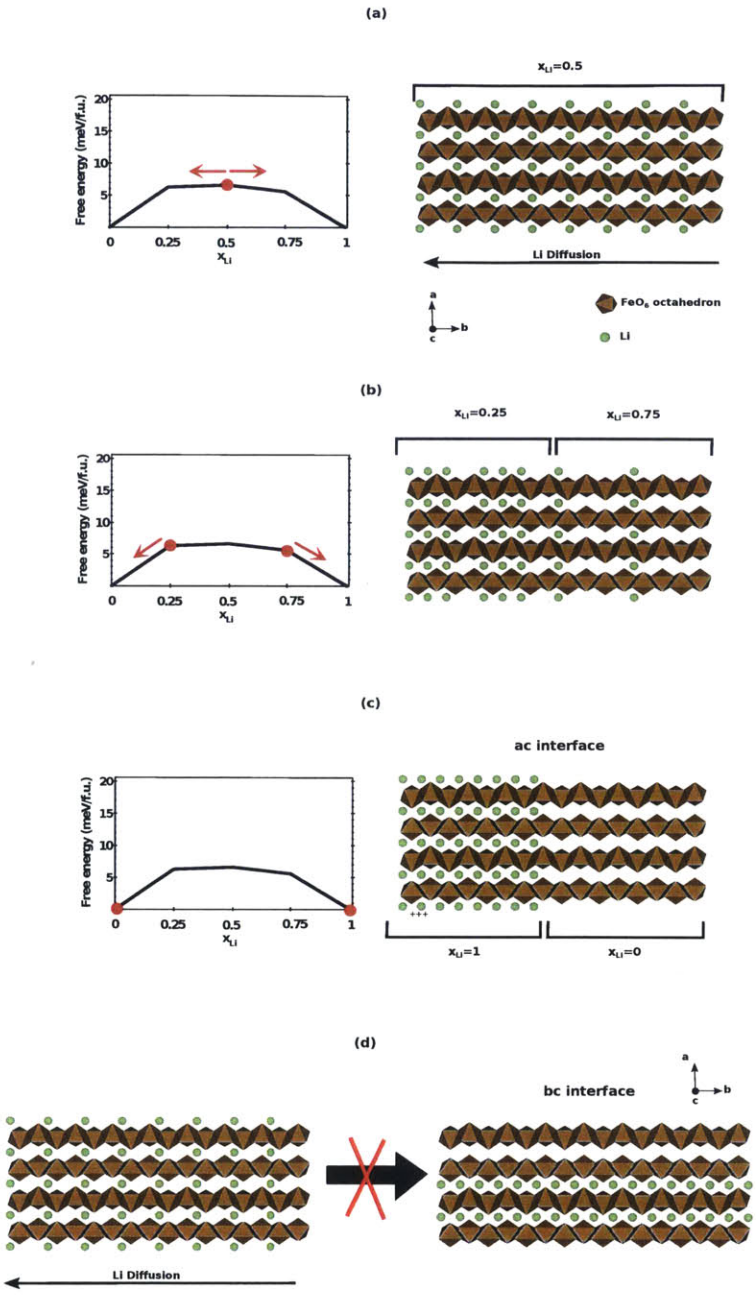

Figure 5-4: Orientation of the most likely interface after spinodal decomposition. **(a)-(c)** Spinodal decomposition from a homogeneous solid-solution dominated by *ac* orderings through 1D Li diffusion along the *b* direction preferentially leads to the formation of an *ac*

interface. **(d)** Spinodal decomposition from a homogeneous solid-solution state to a *bc* interface is unlikely, as it requires an initial increase in the local bulk free energy (through the breaking of local *ac* orderings), as well as significant diffusion in the *a* and *c* directions (several order of magnitudes lower than in the *b* direction).

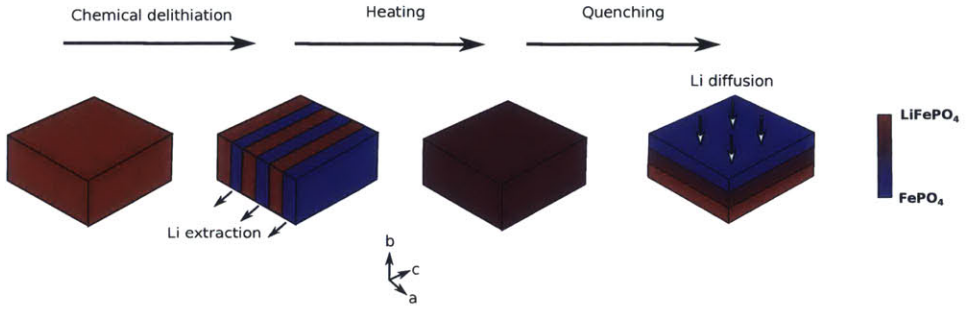

Figure 5-5: : Illustration of the quenching experiment by Chen et al.[105]

An *ac* interface is therefore most likely to be formed after spinodal decomposition from a solid solution, and, on average over the entire particle, is thermodynamically favorable over a homogeneous solid solution. However, further investigations reveal that a *diffuse ac* interface with a *large* intermediate solid solution is thermodynamically favorable over a sharp *ac* interface. A closer inspection of the coherency strain energy profile in the particle reveals that, near the interface, the coherency strain energy is significantly higher than the solid-solution free energy. This is shown in **Figure 5-6**. **Figure 5-6(a)** shows a contour map of the coherency strain energy density in a cubic particle containing an *ac* interface (average Li concentration of $\bar{x}_{Li} = 0.5$), and **Figure 5-6(b)** shows the profile of the coherency strain energy in the particle interior along the direction perpendicular to the interface. The coherency strain energy at the

vicinity of the interface is found to be on the order 25 meV/f.u., which is significantly higher than the ~6 meV/f.u. bulk free energy of the solid solution. (Note that, for an *ac* interface, the effect of the chemical interfacial energy is small (0.03 meV/f.u. for a 100 nm particle) and can be neglected.[109])

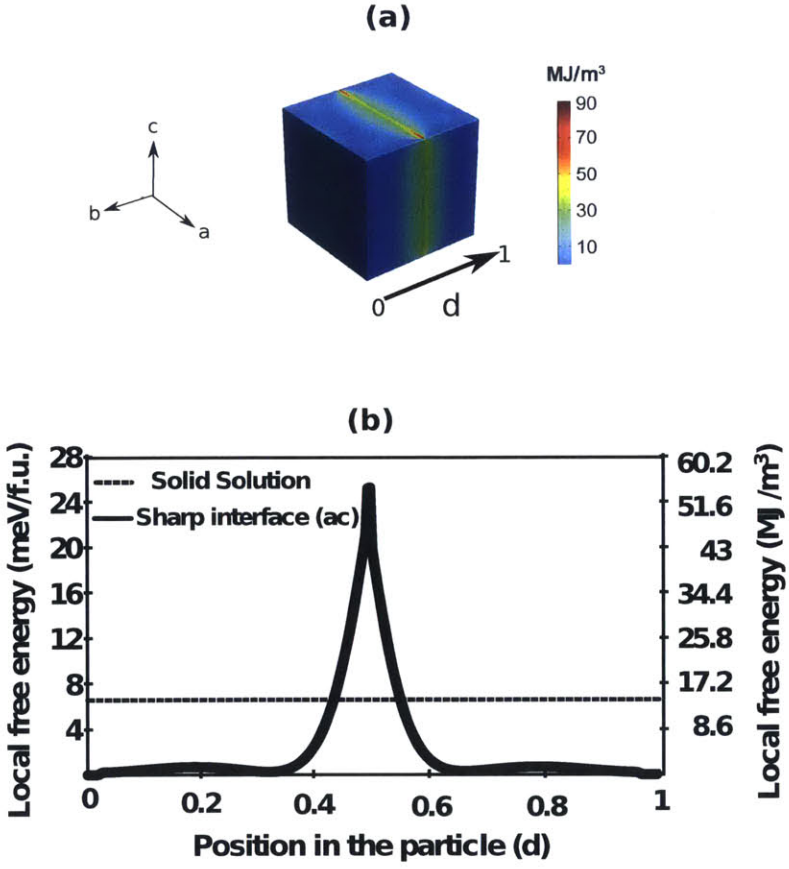

Figure 5-6: : Comparing the local free energy distribution of a homogeneous solid-solution state and of a sharp *ac* interface In both cases, the Li concentration is set to $x_{Li} = 0.5$ at the particle level. **(a)** Contour plot of the coherency strain energy density profile resulting from a sharp *ac* interface **(b)** The local coherency strain energy density at different positions in the

particle is compared with the non-equilibrium solid-solution free energy (line scan along the *b* direction, at 80% of the distance between the particle center and the external *bc* surface).

Based on these energy scales, introducing an ISSR at the $LiFePO_4/FePO_4$ interface can decrease the free energy of the particle by reducing the coherency strain energy in the vicinity of the interface. This is illustrated quantitatively in **Figure 5-7**, in which the free energy resulting from the insertion of an ISSR at the $LiFePO_4/FePO_4$ interface (normalized by the particle volume) is plotted with respect to the ISSR volume fraction y_{ISSR}. A uniform concentration gradient in the ISSR is considered (from $x_{Li} = 1$ to $x_{Li} = 0$). In **Figure 5-7**(a), the analysis is made for a cubic particle, while in **Figure 5-7**(b), the analysis is made for an *ac*-platelet particle with an aspect ratio of 2 ($L_a / L_b = L_c / L_b = 2$, where L_a, L_b and L_c are the particle dimensions along the *a*, *b* and *c* directions respectively). Such *ac*-platelet morphologies, for which the particle dimension along the *b* direction is smaller than along the *a* and *c* dimensions, are common in the $LiFePO_4$ literature.[45,105,111,112]

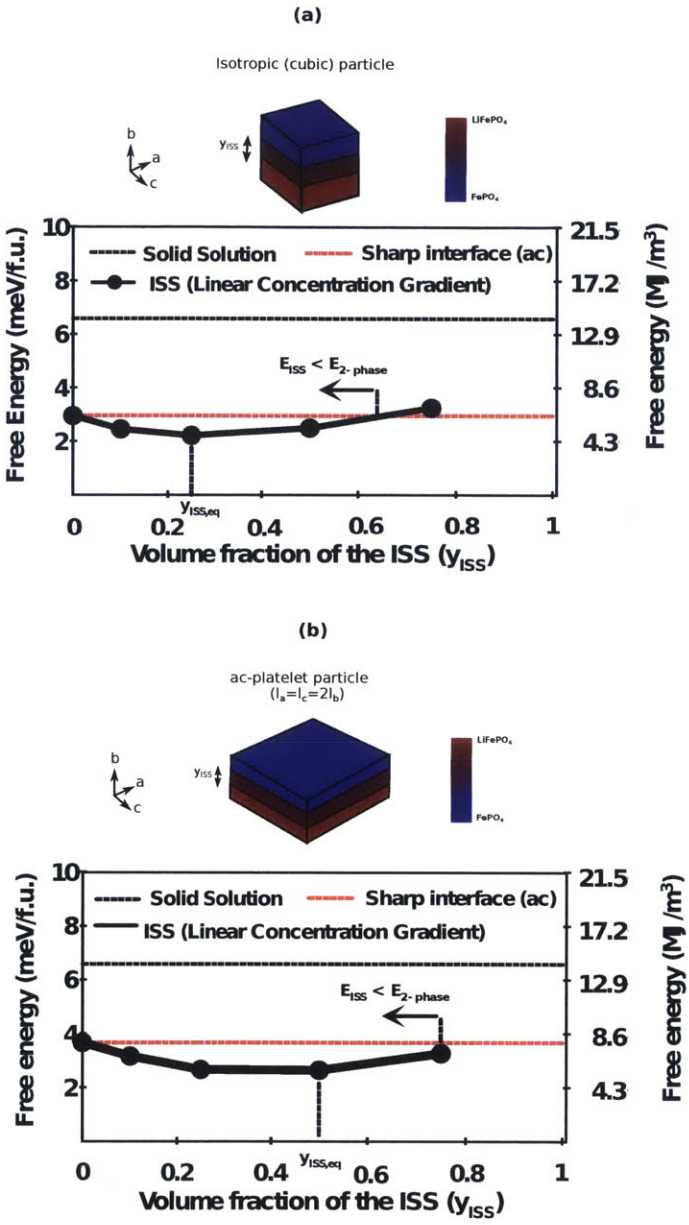

Figure 5-7: Thermodynamic stability of intermediate solid-solution states after spinodal decomposition to an *ac* interface. The energy penalty for a sharp interface and for a diffuse ISSR interface (averaged over the entire particle) are compared, as a function of the volume

fraction of the ISSR (y_{ISSR}), for **(a)** a cubic particle and **(b)** an *ac*-platelet particle (aspect ratios $L_b/L_a = L_b/L_c = 0.5$).

For a cubic particle (**Figure 5-7**(a)), it is therefore found that ISSR volume fractions as high as 50% are thermodynamically favorable over a sharp interface, with an equilibrium volume fraction ($y_{ISSR,eq}$) of 25%. For *ac*-platelet particles with an aspect ratio of two (**Figure 5-7**(b)), the volume fraction of thermodynamically favorable intermediate solid-solution states is larger than in the cubic particle, due to the larger coherency-strain energy at the interface.[109,113] For such particles, an ISSR volume fraction of up to ~75% of the particle volume is favorable over a sharp *ac* interface, with an equilibrium volume fraction of $y_{ISSR,eq} \approx 50\%$.

Note that particle morphology has a direct impact on the coherency strain energy penalty resulting from the presence of an interface. It is a known fact that the coherency strain energy penalty increases as the dimensions of the particle parallel to the interface increase relative to the dimensions perpendicular to the interface. The volume-averaged coherency strain energy density associated with an *ac* interface increases as the L_b / L_a ratio is decreased, because the dimension perpendicular to the interface (L_b) is reduced with respect to the dimensions parallel to the interface (L_a and L_c). The opposite applies for the *bc* interface, for which the dimension perpendicular to the interface (L_a and L_c, respectively) decreases with respect to one of the dimensions parallel to the interface (L_b) . Based on these considerations, is therefore expected that ac-platelet particles have a larger intermediate solid solution volume fraction y_{ISSR} than cubic particles.

It is important to note that, at a given particle morphology, coherency strain energy scales as the volume of the particle. Because the thermodynamic stability of intermediate solid solutions

originates from a reduction in coherency strain energy, the *equilibrium volume fraction of the ISSR is independent of the particle size* for a given particle morphology. For example, with $y_{ISSR,eq}$ being ~25% for a cubic particle, a 50 nm cubic particle is predicted to have a 12.5-nm-thick ISSR at thermodynamic equilibrium while a 100 nm cubic particle is predicted to have a 25-nm-thick ISSR at thermodynamic equilibrium. The ISSR volume fraction and thickness increase for platelet particles with larger (010) faces, which are common in the $LiFePO_4$ literature.

Our results therefore indicate that, while spinodal decomposition from a homogeneous solid solution can rapidly occur at the particle surface due to fast Li diffusion, it is more likely to lead to a diffuse *ac* interface with an intermediate solid-solution region occupying a large fraction of the particle volume (~25-50% for the particle morphologies illustrated in **Figure 5-7**). Moreover, this volume fraction is independent of the particle size at a given particle morphology. This result explains not only the persistence of intermediate solid-solution states at an *ac* interface after quenching of homogeneous solid solutions, but also the observation of intermediate lattice parameters during *in situ* XRD (dis)charging experiments at low-to-moderate C-rates.

5.4 Discussion

An important consequence of our study is that there exists a thermodynamic origin to the persistence of large intermediate solid solutions region during (de)lithiation. Even in the limit of zero-rates, particle-by-particle lithiation[48] is predicted to occur through the non-equilibrium solid-solution pathway, followed by spinodal decomposition to a two-phase state with a large intermediate solid-solution region. In agreement with this finding, *in situ* TEM experiments have observed intermediate solid-solution states at rates as low as 5 C, and a recent in situ XRD experiment has observed intermediate solid solution states at rates as low as 0.1C (~20% of the particle volume).[53] The fact that intermediate lattice parameters are generally not observed at very low C-rates by experimental methods relying on electrode-level measurements can be ascribed to the multi-particle behavior of $LiFePO_4$.[114,115] In the low-rate limit, particles transform sequentially while at high rates, they transform in parallel. High rates allow more particles to transform simultaneously, producing sufficiently large intensity in diffraction peaks at intermediate lattice parameters.

While some *in situ* XRD experiments have identified a continuum spectrum of intermediate lattice parameters in the electrode,[52] others have measured discrete peaks that have been attributed to one or several discrete intermediate phases.[50] In agreement with the latter observation, our calculations predict that large intermediate solid solution regions made of discrete intermediate phases are also thermodynamically favorable over a sharp interface. An ISSR containing a single intermediate phase at $x_{Li} = 0.5$, for example, has an equilibrium ISSR

volume fraction of $y_{ISSR,eq} = 10\%$ (cubic particle). This percentage rises to 25% for the *ac*-platelet particle illustrated in **Figure 5-7**(b). In general, however, having multiple intermediate phases in the ISSR is energetically favorable over a single intermediate phase, as it further reduces both the coherency strain energy in the particle and the bulk free energy penalty of the ISSR (as phases closer in concentration to the equilibrium phases have a lower bulk free energy).

Intermediate lattice parameters are typically measured in nano-sized particles and not in micron-sized particles.[116] Because an ISSR reduces the high coherency strain energy resulting from a sharp interface, and because coherency strain energy scales with particle volume, the formation of an ISSR is thermodynamically favorable over a sharp *coherent* interfaces at all particle sizes. In large particles, however, formation of a semicoherent interface, where the lattice misfit is accommodated to some degree by interfacial dislocations, is even more favorable. A semicoherent interface reduces the coherency strain energy penalty (which scales as the particle volume) at the expense of a higher chemical interfacial energy (which scales as the interfacial area), through the formation of misfit dislocations. This process is favorable in large particles due to their small interfacial-area-to-volume ratios. Supporting the hypothesis that the formation of misfit dislocations is responsible for the lack of ISSR in large particles, the propagation of a semi-incoherent *ac* interface with a large density of dislocations was observed during an *in situ* lithiation experiment of micron-sized $FePO_4$ particles.[117] Rate capabilities were found to be low (1 C rate at a ~400 mV overpotential), indicating that the presence of interfacial dislocations significantly affects interfacial mobility.

Overall, the existence of a low-energy non-equilibrium solid-solution pathway in $LiFePO_4$ has multiple benefits. First, the existence of a non-equilibrium low-energy solid-solution pathway

allows particles to initiate (de)lithiation at low overpotentials, increasing rate capabilities with respect to systems undergoing nucleation and growth. Moreover, after spinodal decomposition, the presence of a thermodynamically favorable ISSR at the interface leads to a decrease in coherency strain energy. This in turn reduces mechanical damage upon cycling and improves cyclability. Finally, the presence of an ISSR decreases the driving force to form a semicoherent interface, thus enhancing cyclability and rate capabilities.

It is important to note that our model operated under the assumption that (de)lithiation is always initiated by the low-energy non-equilibrium solid-solution pathway, which is dominated by low-energy *ac* orderings and accessible at low overpotentials. However, when higher overpotentials are applied, more lithiation pathways may become available. Nucleation and growth, for example, can occur in the large overpotential limit. This is the case during chemical delithiation, where large applied overpotentials (~1.5V[102]) can lead to nucleation and subsequent formation of the elastically favorable sharp *bc* interface. Given the low coherency strain energy at a sharp *bc* interface, the formation of an intermediate solid-solution region is largely dominated by the chemical interfacial energy. Using the well-known relation $\delta = \sqrt{\kappa / \overline{f_{ss}}}$ [108] (where δ is the interfacial width, $\overline{f_{ss}}$ is the average solid-solution free energy in the $x_{Li} = [0,1]$ range and κ is the gradient energy coefficient of the *bc* interface[109]), the size of the intermediate solid-solution region is found to be ~10 nm regardless of the particle size. This prediction is consistent with *ex situ* observations of chemically delithiated particles[45,112] and further confirms that the formation of a *bc* interface is not the dominant mechanism during electrochemical delithiation of nanoparticles. The ~10nm ISSR associated with the formation of a *bc* interface is indeed inconsistent with *in situ* XRD measurements on ~186nm particles, where the solid solution region was found to be on the order of the particle size.[52]

High-energy solid-solution pathways, different from the low energy *ac* orderings reported in this chapter, can also be accessed if the applied overpotential is large enough. The experimentally observed "*bc* staging" ordering, [118-121] which consists of a solid solution of alternately lithiated *bc* planes, is one such example. Staging configurations were observed in *ex situ* conditions in the form of a small ~2 nm ISSR[119] or uniformly throughout nanoparticles or micron-sized nanowires.[120] DFT calculations demonstrate that the energy required to access the *bc* staging pathway is significantly higher than the energy required to access the *ac* ordering pathway (70 meV/f.u [in agreement with the values found by Sun et al. [121]], instead of 6 meV/f.u at $x_{Li} = 0.5$). The overpotential to access the *bc*-staging pathway, which can be calculated from $dE_{formation}/dx_{Li}$ at dilute staging concentrations, is also significantly higher (~215 mV instead of ~25 mV, as shown in **Figure 5-2**(b)). The *bc*-staging pathway therefore cannot account for the high-rate capability of $LiFePO_4$, which is defined as the ability to achieve high currents at low overpotentials, but could become competitive with the low energy *ac* solid-solution pathway at large overpotentials. Once a uniform *bc* staging configuration is formed in a particle, it is likely to remain metastable, as relaxation from a *bc* staging requires significant Li diffusion in the slow-diffusing *a* direction. This may explain observations of uniform *bc* staging throughout nanoparticles and micron-sized nanowires. [120]

Figure 5-8 summarizes the above considerations by qualitatively illustrating the range of possible lithiation mechanisms in $LiFePO_4$ particles as a function of the particle size and applied overpotential. At low overpotentials, both small and large particles initiate lithiation via the non-equilibrium solid solution pathway, dominated by low energy *ac* orderings. Spinodal decomposition in small particles preferentially leads to the formation of a diffuse *ac* interface, while it leads to the formation of a semicoherent interface in large particles. At high

overpotentials, small particles can access higher energy orderings in the solid solution (such as the *bc* staging configuration). The higher rates induced by these high overpotentials also lead to a higher retention of the solid solution. In large particles, higher overpotentials open up the nucleation and growth pathway (due to the large number of nucleation sites), in addition to the spinodal decomposition pathway. Both mechanisms, however, lead to low rates due to poor Li diffusivity in large particles, through the presence of channel-blocking anti-site defects[42] and the formation of semicoherent interfaces.

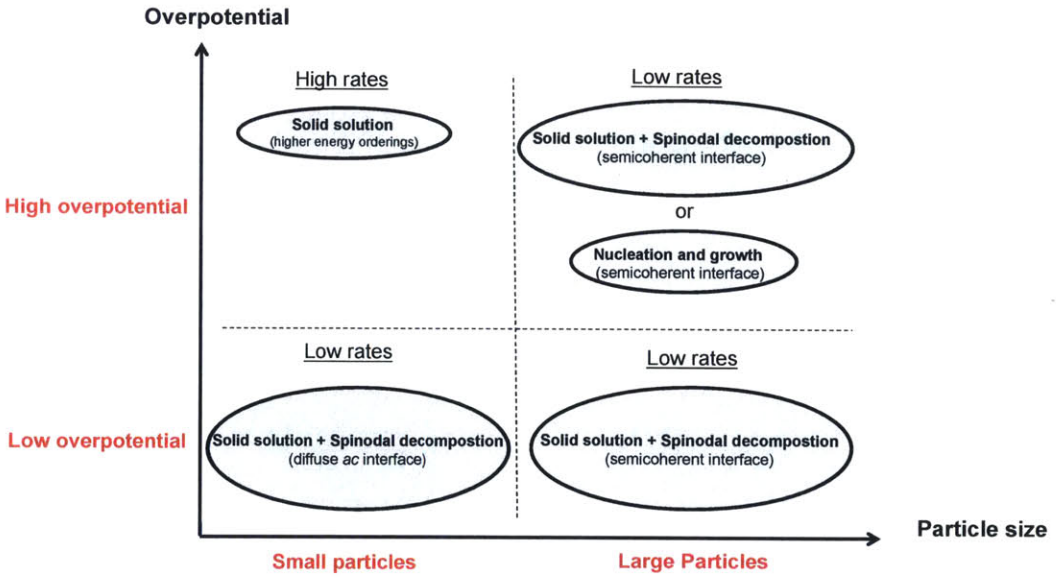

Figure 5-8: Qualitative map of the lithiation mechanism in $LiFeO_4$ single particles as a function of particle size and applied overpotential. Note that this map applies to the particles that are actively transforming in the electrode.

5.5 Conclusion

In this chapter, we resolved the apparent paradox between the high Li diffusivity in $LiFePO_4$ and the persistence of thermodynamically unstable solid-solution states during (dis)charge at low to moderate C-rates. Using a combination of first principles calculations and continuum elasticity, we demonstrated that, even under rate conditions such that relaxation to a two-phase state is kinetically possible, the thermodynamically favorable state in a single particle is not a sharp interface but rather a diffuse interface with an *intermediate solid-solution region* that occupies a significant fraction of the particle volume. Our results not only explain the persistence of solid-solution regions at low to moderate C-rates in $LiFePO_4$ electrodes, but also explain the observations of stable intermediate solid-solution states at an *ac* interface in single particles quenched from a solid solution.

Conclusions

In order to accelerate the electrification of the automotive fleet, the energy density and power density of current Li-ion batteries must be improved. The cathode, which is currently commercially dominated layered transition metal oxides, is an important performance limiting-factor in Li-ion batteries. In this thesis, we developed critical insights on two important classes of materials that respectively aim at improving the energy density and power density of Li-ion battery cathodes, namely high-capacity Li-excess cation-disordered rocksalts and high-rate $LiFePO_4$ olivine.

In Chapter 3 and 4, we used first principles calculations to establish the first voltage-based design rules for high-capacity cation-disordered rocksalts. In Chapter 3, we studied the effect of cation disorder on the average voltage of transition metal oxides, which controls the total energy density in these compounds. We demonstrated that, depending on the transition metal species, cation disorder can result in an increase or a reduction of the average Li intercalation voltage. Transition metals that have a higher disordering energy in the MO_2 limit display larger average voltages than their ordered ground-states, while transition metals that have a higher disordering energy in the $LiMO_2$ limit display a lower voltage than their ordered ground-state. Furthermore, cation disorder was shown to significantly alter the average voltage of certain lithium transition metal oxides and therefore lead to significant changes in their voltage operating windows. In particular, the disordered $Ni^{3+/4+}$ redox was found to be high (~4.4V), suggesting that it is likely to be preceded by oxygen activity in disordered compounds. Finally, we showed that compounds that disorder *in situ* during delithiation have a lower voltage in their disordered form, while compounds that disorder *in situ* during lithiation have a higher

voltage in their disordered form.

In Chapter 4, we developed a model based on first principles to understand the effect of cation disorder on the voltage slope of cation disordered rocksalts, which controls the total capacity available below the stability limit of the electrolyte. The voltage slope was shown to be controlled by three factors: the site energy distribution (Li-M interactions), the effective Li-Va interaction and Li insertion in high-voltage tetrahedral sites. Our study demonstrated that high-voltage transition metals generally have a lower voltage slope than low-voltage transition metals and that octahedral Li insertion in high-voltage compounds leads to minimum capacity above the electrolyte stability limit (with the exception of $LiNiO_2$, which has a high disordered average voltage). Tetrahedral Li insertion however, was shown to lead to ~25% inaccessible capacity in fully disordered (i.e. random) $LiMO_2$. Furthermore, our study highlighted the fact that, in practical disordered compounds, important factors contribute in reducing the voltage slope with respect to the random $LiMO_2$ limit. Short-range order mitigates the voltage slope increase by reducing the amount of local environments around Li sites, as well as by decreasing the availability of tetrahedral sites. Furthermore, the amount of octahedral capacity lost upon disorder decreases with the introduction of Li-excess, which is a necessary requirement for macroscopic Li diffusion in disordered rocksalts.

Chapter 3 and 4 therefore constitute the first comprehensive *ab initio* investigation of the effect of cation disorder on the voltage profile of lithium transition metal oxides.

In Chapter 5, we used first principles calculations to gain a deeper understanding of the fundamental lithiation mechanisms of phase-separating nano-$LiFePO_4$ olivine, an important high-power cathode material for Li-ion batteries. We resolved the apparent paradox between

the high Li diffusivity in $LiFePO_4$ and the persistence of thermodynamically unstable solid-solution states during (dis)charge at low to moderate C-rates. Using a combination of first principles calculations and continuum elasticity, we demonstrated that, even under rate conditions such that relaxation to a two-phase state is kinetically possible, the thermodynamically favorable state in a single particle is not a sharp interface but rather a diffuse interface with an *intermediate solid-solution region* that occupies a significant fraction of the particle volume. Our results not only explain the persistence of solid-solution regions at low to moderate C-rates in $LiFePO_4$ electrodes, but also explain the observations of stable intermediate solid-solution states at an *ac* interface in single particles quenched from a solid solution.

This thesis therefore provides new and critical understanding on important high-energy and high-power alternatives to traditional layered transition metal oxide cathodes for Li-ion batteries. Such insights can be leveraged as part of a broader strategy to facilitate the design and optimization of next-generation Li-ion battery cathodes.

References

1. World Resources Institute. *WRI Annual Report 2005*. (2005).

2. National Highway Traffic Safety Administration. *Corporate Average Fuel Economy*. (http://www.nhtsa.gov/fuel-economy). at <http://www.nhtsa.gov/fuel-economy>

3. Tarascon, J. M. & Armand, M. Issues and challenges facing rechargeable lithium batteries. *Nature* **414,** 359–367 (2001).

4. Persson, K., Hinuma, Y., Meng, Y. S., Van der Ven, A. & Gerbrand, C. Thermodynamic and kinetic properties of the Li-graphite system from first-principles calculations. *Physical Review B* **82,** (2010).

5. Cho, J., Kim, Y. J. & Park, B. Novel LiCoO2 Cathode Material with Al2O3 Coating for a Li Ion Cell. *Chem Mater* **12,** 3788–3791 (2000).

6. Cho, Y. & Cho, J. Significant Improvement of LiNi0.8Co0.15Al0.05O2 Cathodes at 60°C by SiO2 Dry Coating for Li-Ion Batteries. *Journal of the Electrochemical Society* **157,** A625–A629 (2010).

7. Kobayashi, H. *et al.* Investigation on lithium de-intercalation mechanism for Li1−yNi1/3Mn1/3Co1/3O2. *Journal of Power Sources* **146,** 640–644 (2005).

8. Kang, K., Meng, S., Breger, J., Grey, C. P. & Ceder, G. Electrodes with High Power and High Capacity for Rechargeable Li Batteries. *Science* 973–977

9. Goodenough, J. B. & Park, K.-S. The Li-Ion Rechargeable Battery: A Perspective. *Journal of the American Chemical Society* **135,** 1167–1176 (2013).

10. Urban, A., Lee, J. & Gerbrand, C. The Configurational Space of Rocksalt-Type Oxides for High-Capacity Lithium Battery Electrodes. *Adv. Energy Mater.* 1–9 (2014).

11. Van der Ven, A., Aydinol, M. K. & Ceder, G. First-principles investigation of phase stability in Li_xCoO_2. *Physical Review B* **58,** 2975–2987 (1998).

12. Van der Ven, A. & Ceder, G. Lithium diffusion mechanisms in layered intercalation compounds. *Journal of Power Sources* **97-98,** 529–531 (2001).

13. Jain, A., Hautier, G., Ong, S. P., Dacek, S. & Gerbrand, C. Relating voltage and thermal safety in Li-ion battery cathodes: a high-throughput computational study. *Phys. Chem. Chem. Phys.* **17,** 5942–5953 (2015).

14. Lyu, Y. *et al.* Atomic insight into electrochemical inactivity of lithium chromate (LiCrO2): Irreversible migration of chromium into lithium layers in surface regions. *Journal of Power Sources* **273,** 1218–1225 (2015).

15. Lee, J. *et al.* Unlocking the Potential of Cation-Disordered Oxides for Rechargeable Lithium Batteries. *Science* (2014).

16. Pralong, V., Gopal, V., Caignaert, V., Duffort, V. & Raveau, B. Lithium-Rich Rock-Salt-Type Vanadate as Energy Storage Cathode: Li2–xVO3. *Chem Mater* **24,** 12–14 (2012).

17. Lee, J. *et al.* A new class of high capacity cation-disordered oxides for rechargeable lithium batteries: Li–Ni–Ti–Mo oxides. *Energy Environ. Sci.* (2015).

18. Yabuuchi, N. *et al.* High-capacity electrode materials for rechargeable lithium batteries: Li 3NbO4-based system with cation-disordered rocksalt structure. *Proc Natl Acad Sci USA* **112,** 7650–7655 (2015).

19. Wang, R. *et al.* A disordered rock-salt Li-excess cathode material with high capacity and substantial oxygen redox activity: Li1.25Nb0.25Mn0.5O2. *Electrochemistry Communications* **60,** 70–73 (2015).

20. Glazier, S. L., Li, J., Zhou, J., Bond, T. & Dahn, J. R. Characterization of Disordered Li (1+x)Ti2xFe(1–3x)O2 as Positive Electrode Materials in Li-Ion Batteries Using Percolation Theory. *Chem Mater* acs.chemmater.5b03530 (2015).

21. Saubanere, M., Ben Yahia, M., Lebegue, S. & Doublet, M. L. An intuitive and efficient method for cell voltage prediction of lithium and sodium-ion batteries. *Nature Communications* **5,** 1–7 (2014).

22. Hwang, S. *et al.* Investigation of Changes in the Surface Structure of LixNi0.8Co0.15Al0.05O2 Cathode Materials Induced by the Initial Charge. *Chem Mater* **26,** 1084–1092 (2014).

23. Zheng, J. *et al.* Structural and Chemical Evolution of Li- and Mn-Rich Layered Cathode Material. *Chem Mater* **27,** 1381–1390 (2015).

24. Thackeray, M. M. *et al.* Li2MnO3-stabilized LiMO2 (M = Mn, Ni, Co) electrodes for lithium-ion batteries. *J. Mater. Chem.* **17,** 3112 (2007).

25. Armstrong, A. R. *et al.* Demonstrating Oxygen Loss and Associated Structural Reorganization in the Lithium Battery Cathode Li[Ni 0.2Li 0.2Mn 0.6]O2. *Journal of the American Chemical Society* **128,** 8694–8698 (2006).

26. Tran, N. *et al.* Mechanisms Associated with the 'Plateau' Observed at High Voltage for the Overlithiated Li 1.12(Ni 0.425Mn 0.425Co 0.15) 0.88O 2System. *Chem Mater* **20,** 4815–4825 (2008).

27. Yan, P. *et al.* Evolution of Lattice Structure and Chemical Composition of the Surface Reconstruction Layer in Li 1.2Ni 0.2Mn 0.6O 2Cathode Material for Lithium Ion Batteries. *Nano Letters* **15,** 514–522 (2015).

28. Boulineau, A. *et al.* Evolutions of Li 1.2Mn0.61Ni0.18Mg0.01O2 during the Initial Charge/Discharge Cycle Studied by Advanced Electron Microscopy. *Chem Mater* **24,**

3558–3566 (2012).

29. Hwang, S. *et al.* Investigation of Changes in the Surface Structure of LixNi 0.8Co0.15Al0.05O2 Cathode Materials Induced by the Initial Charge. *Chem Mater* **26,** 1084–1092 (2014).

30. Zaghib, K., Mauger, A., Goodenough, J. B., Gendron, F. & Julien, C. M. Electronic, Optical, and Magnetic Properties of LiFePO 4: Small Magnetic Polaron Effects. *Chem Mater* **19,** 3740–3747 (2007).

31. Padhi, A., Nanjundaswamy, K. & Goodenough, J. Phospho-olivines as positive-electrode materials for rechargeable lithium batteries. *Journal of the Electrochemical Society* **144,** 1188–1194 (1997).

32. Ellis, B. L., Lee, K. T. & Nazar, L. F. Positive Electrode Materials for Li-Ion and Li-Batteries. *Chem Mater* **22,** 691–714 (2010).

33. Nishimura, S.-I. *et al.* Experimental visualization of lithium diffusion in LixFePO4. *Nature Materials* **7,** 707–711 (2008).

34. Morgan, D., Van der Ven, A. & Ceder, G. Li conductivity in LixMPO4 (M = Mn, Fe, Co, Ni) olivine materials. *Electrochem Solid St* **7,** A30–A32 (2004).

35. Islam, M. S., Driscoll, D. J., Fisher, C. A. J. & Slater, P. R. Atomic-Scale Investigation of Defects, Dopants, and Lithium Transport in the LiFePO4 Olivine-Type Battery Material. *Chem Mater* **17,** 5085–5092 (2005).

36. Huang, H., Yin, S. C. & Nazar, L. F. Approaching Theoretical Capacity of LiFePO4 at Room Temperature at High Rates. *Electrochem Solid St* **4,** A170 (2001).

37. Yamada, A., Chung, S. C. & Hinokuma, K. Optimized LiFePO4 for Lithium Battery Cathodes. *Journal of the Electrochemical Society* **148,** A224 (2001).

38. Sides, C., Croce, F., Young, V., Martin, C. & Scrosati, B. A high-rate, nanocomposite LiFePO4/carbon cathode. *Electrochem Solid St* **8,** A484–A487 (2005).

39. Yamada, A., Yonemura, M., Takei, Y., Sonoyama, N. & Kanno, R. Fast charging LiFePO4. *Electrochem Solid St* **8,** A55–A58 (2005).

40. Kang, B. & Gerbrand, C. Battery materials for ultrafast charging and discharging. *Nature* **458,** 190–193 (2009).

41. Chung, S.-Y., Choi, S.-Y., Yamamoto, T. & Ikuhara, Y. Atomic-Scale Visualization of Antisite Defects in LiFePO4. *Physical Review Letters* **100,** (2008).

42. Malik, R., Burch, D., Bazant, M. & Gerbrand, C. Particle Size Dependence of the Ionic Diffusivity. *Nano Letters* **10,** 4123–4127 (2010).

43. Ramana, C. V., Mauger, A., Gendron, F., Julien, C. M. & Zaghib, K. Study of the Li-insertion/extraction process in LiFePO4/FePO4. *Journal of Power Sources* **187,** 555–

564 (2009).

44. Andersson, A. & Thomas, J. The source of first-cycle capacity loss in LiFePO4. *Journal of Power Sources* **97-8,** 498–502 (2001).

45. Chen, G., Song, X. & Richardson, T. Electron microscopy study of the LiFePO4 to FePO4 phase transition. *Electrochem Solid St* **9,** A295–A298 (2006).

46. Delmas, C., Maccario, M., Croguennec, L., Le Cras, F. & Weill, F. Lithium deintercalation in LiFePO4 nanoparticles via a domino-cascade model. *Nature Materials* **7,** 665–671 (2008).

47. Malik, R., Zhou, F. & Ceder, G. Kinetics of non-equilibrium lithium incorporation in LiFePO4. *Nature Materials* **10,** 587–590 (2011).

48. Dreyer, W. *et al.* The thermodynamic origin of hysteresis in insertion batteries. *Nature Materials* **9,** 448–453 (2010).

49. Bai, P., Cogswell, D. A. & Bazant, M. Z. Suppression of Phase Separation in LiFePO4 Nanoparticles During Battery Discharge. *Nano Letters* **11,** 1–7 (2011).

50. Orikasa, Y. *et al.* Direct Observation of a Metastable Crystal Phase of LixFePO4 under Electrochemical Phase Transition. *Journal of the American Chemical Society* **135,** 5497–5500 (2013).

51. Zhang, X. *et al.* Rate-Induced Solubility and Suppression of the First-Order Phase Transition in Olivine LiFePO4. *Nano Letters* A–G (2014).

52. Liu, H. *et al.* Capturing metastable structures during high-rate cycling of LiFePO4 nanoparticle electrodes. *Science* **344,** 1252817–1252817 (2014).

53. Zhang, X. *et al.* Direct view on the phase evolution in individual LiFePO4 nanoparticles during Li-ion battery cycling. *Nature Communications* **6,** 8333 (2015).

54. Sugiyama, J. *et al.* Magnetic and diffusive nature of LiFePO4 investigated by muon spin rotation and relaxation. *Physical Review B* **84,** (2011).

55. Hohenberg, P. & Kohn, W. Inhomogeneous Electron Gas. *Physical Review* **136,** 864–871 (1964).

56. Kohn, W. & Sham, L. J. Self-Consistent Equations Including Exchange and Correlation Effects. *Physical Review* **140,** 1133–1138 (1965).

57. Martin, R. M. *Electronic Structure: Basic Theory and Practical Methods*. (Cambridge University Press, 2004).

58. Perdew, J. P., Burke, K. & Ernzerhof, M. Generalized Gradient Approximation Made Simple. *Physical Review Letters* **77,** 3865–3868 (1996).

59. Anisimov, V. I., Zaanen, J. & Andersen, O. K. Band theory and Mott insulators: Hubbard U instead of Stoner I. *Physical Review B* **44,** 943–954 (1991).

60. Dudarev, S. L., Botton, G. A., Savrasov, S. Y., Humphreys, C. J. & Sutton, A. P. Electron-energy-loss spectra and the structural stability of nickel oxide: An LSDA-U study. *Physical Review B* **57,** 1505–1509 (1998).

61. Jain, A. *et al.* A high-throughput infrastructure for density functional theory calculations. *COMPUTATIONAL MATERIALS SCIENCE* **50,** 2295–2310 (2011).

62. Zhou, F., Kang, K., Maxisch, T., Gerbrand, C. & Morgan, D. The electronic structure and band gap of LiFePO4 and LiMnPO4. *Solid State Communications* **132,** 181–186 (2004).

63. Kresse, G. & Joubert, D. From ultrasoft pseudopotentials to the projector augmented-wave method. *Physical Review B* **59,** 1758–1775 (1999).

64. Sanchez, J. M., Ducastelle, F. & Gratias, D. Generalized cluster description of multicomponent systems. *Physica A: Statistical Mechanics and its Applications* **128,** 334–350 (1984).

65. Wolverton, C. & De Fontaine, D. Cluster expansions of alloy energetics in ternary intermetallics. *Physical Review B* **49,** 1–21 (1994).

66. Nelson, L. J., Hart, G. L. W., Zhou, F. & Ozoliņš, V. Compressive sensing as a paradigm for building physics models. *Physical Review B* **87,** (2013).

67. Newman, M. E. & Barkema, G. T. *Monte Carlo Methods in Statistical Physics*. (Oxford University Press, 1999).

68. Zunger, A., Wei, S.-H., Ferreira, L. G. & Bernard, J. E. Special Quasirandom Structures. *Physical Review Letters* **65,** 1–4 (1990).

69. Shin, D., van de Walle, A., Wang, Y. & Liu, Z.-K. First-principles study of ternary fcc solution phases from special quasirandom structures. *Physical Review B* **76,** 144204 (2007).

70. Brunetti, G. *et al.* Confirmation of the Domino-Cascade Model by LiFePO4/FePO4 Precession Electron Diffraction. *Chem Mater* **23,** 4515–4524 (2011).

71. Yu, H.-C., Chen, H.-Y. & Thornton, K. Extended smoothed boundary method for solving partial differential equations with general boundary conditions on complex boundaries. *Modelling Simul. Mater. Sci. Eng.* **20,** 075008 (2012).

72. Maxisch, T. & Ceder, G. Elastic properties of olivine LixFePO4 from first principles. *Physical Review B* **73,** (2006).

73. Fiorentini, V. & Methfessel, M. Extracting convergent surface energies from slab calculations. *J. Phys.: Condens. Matter* **8,** 6525–6529 (1996).

74. Sun, W. & Gerbrand, C. Efficient creation and convergence of surface slabs. *Surface Science* **617,** 53–59 (2013).

75. Urban, A., Lee, J. & Gerbrand, C. The Configurational Space of Rocksalt-Type Oxides for High-Capacity Lithium Battery Electrodes. *Adv. Energy Mater.* n/a–n/a (2014). doi:10.1002/aenm.201400478

76. Bo, S., Li, X. & Gerbrand, C. Layered-to-Rock-Salt Transformation in Desodiated NaCrO2 (submitted).

77. Ozawa, K. *et al.* Structural modifications caused by electrochemical lithium extraction for two types of layered LiVO2 (R3m). *Journal of Power Sources* **174,** 469–472 (2007).

78. BAUDRIN, E. *et al.* Structural evolution during the reaction of Li with nano-sized rutile type TiO2 at room temperature. *Electrochemistry Communications* **9,** 337–342 (2007).

79. Wang, D. *et al.* Synthesis and Li-Ion Insertion Properties of Highly Crystalline Mesoporous Rutile TiO2. *Chem Mater* **20,** 3435–3442 (2008).

80. Hewston, T. A. & Chamberland, B. L. A survey of first-row ternary oxides LiMO2 (M=Sc-Cu). *J. Phys. Chem. Solids* **48,** 97–108 (1987).

81. Obrovac, M. N., Mao, O. & Dahn, J. R. Structure and electrochemistry of LiMO2 (M=Ti, Mn, Fe, Co, Ni) prepared by mechanochemical synthesis. *Solid State Ionics* **112,** 9–19 (1998).

82. Chang, S. H., Kang, S.-G., Song, S.-W., Yoon, J.-B. & Choy, J.-H. Crystal structure and spectroscopic properties of LixNi1-yTiyO2 and their electrochemical behavior. *Solid State Ionics* 1–5 (1998).

83. Küzma, M. *et al.* Electrochemical activity of Li2FeTiO4 and Li2MnTiO4 as potential active materials for Li ion batteries: A comparison with Li2NiTiO4. *Journal of Power Sources* **189,** 81–88 (2009).

84. Yang, M. *et al.* Cation disordered rock salt phase Li2CoTiO4 as a potential cathode material for Li-ion batteries. *J. Mater. Chem.* **22,** 6200 (2012).

85. Kang, K. *et al.* Synthesis and Electrochemical Properties of Layered Li 0.9Ni 0.45Ti 0.55O2. *Chem Mater* **15,** 4503–4507 (2003).

86. Aydinol, M. K., Kohan, A. F. & Ceder, G. Ab initio calculation of the intercalation voltage of lithium-transition-metal oxide electrodes for rechargeable batteries. *Journal of Power Sources* 664–668 (1997).

87. Perdew, J. P., Burke, K. & Ernzerhof, M. Generalized Gradient Approximation Made Simple - Errata. *Physical Review Letters* **78,** (1997).

88. Van der Ven, A., Thomas, J. C., Xu, Q. & Bhattacharya, J. Linking the electronic structure of solids to their thermodynamic and kinetic properties. *Mathematics and Computers in Simulation* **80,** 1393–1410 (2010).

89. Zhang, L. *et al.* Synthesis and electrochemistry of cubic rocksalt Li–Ni–Ti–O compounds in the phase diagram of LiNiO2–LiTiO2–Li[Li1/3Ti2/3]O2. *Journal of Power Sources* **185,** 534–541 (2008).

90. Seo, D.-H., Lee, J., Urban, A., Malik, R. & Ceder, G. *The electronic origin of the oxygen redox activity in Li-excess cathode materials (in preparation).*

91. Marianetti, C. A., Morgan, D. & Ceder, G. First-principles investigation of the cooperative Jahn-Teller effect for octahedrally coordinated transition-metal ions. *Physical Review B* **63,** 224304 (2001).

92. Gaskell, D. R. *Introduction to the Thermodynamics of Materials, Fifth Edition.* (Taylor and Francis Group, 2008).

93. Koga, H. *et al.* Different oxygen redox participation for bulk and surface: A possible global explanation for the cycling mechanism of Li1.20Mn0.54Co0.13Ni0.13O2. *Journal of Power Sources* **236,** 250–258 (2013).

94. Sathiya, M. *et al.* Reversible anionic redox chemistryin high-capacity layered-oxide electrodes. *Nature Materials* **12,** 1–9 (2013).

95. Lee, J. Cation-Disordered Oxides for Rechargeable Lithium Battery Cathodes. *Massachusetts Institute of Technology (Doctoral Thesis)* 1–128 (2015).

96. Breger, J. *et al.* Effect of High Voltage on the Structure and Electrochemistry of LiNi 0.5Mn 0.5O 2: A Joint Experimental and Theoretical Study. *Chem Mater* **18,** 4768–4781 (2006).

97. Croguennec, L. & Palacín, M. R. Recent Achievements on Inorganic Electrode Materials for Lithium-Ion Batteries. *Journal of the American Chemical Society* 150225103601003 (2015). doi:10.1021/ja507828x

98. De Fontaine, D. in **47,** 33–176 (Solid State Physics, 1994).

99. Kaburagi, M. & Kanamori, J. Ground State Structure of Triangular Lattice Gas Model with to 3rd Neighbor Interactions. *Journal of the Physical Society of Japan* **44,** 718–727 (1978).

100. Abdellahi, A., Urban, A., Dacek, S. & Ceder, G. *The effect of cation disorder on the average Li intercalation voltage of transition metal oxides (submitted).* (2015).

101. Jarvis, K. A., Deng, Z., Allard, L. F., Manthiram, A. & Ferreira, P. J. Atomic Structure of a Lithium-Rich Layered Oxide Material for Lithium-Ion Batteries: Evidence of a Solid Solution. *Chem Mater* **23,** 3614–3621 (2011).

102. Dodd, J. L., Yazami, R. & Fultz, B. Phase Diagram of LixFePO4. *Electrochem Solid St* **9,** A151 (2006).

103. Niu, J. *et al.* In situ observation of random solid solution zone in LiFePO4 electrode. *Nano Letters* 1–24 (2014).

104. Li, Y. *et al.* Current-induced transition from particle-by-particle to concurrent intercalation in phase-separating battery electrodes. *Nature Materials* **13,** 1149–1156 (2014).

105. Chen, G., Song, X. & Richardson, T. J. Metastable Solid-Solution Phases in the LiFePO4/FePO4 System. *Journal of the Electrochemical Society* **154,** A627 (2007).

106. Tan, H. J., Dodd, J. L. & Fultz, B. Thermodynamic and Kinetic Stability of the Solid Solution Phase in Nanocrystalline LixFePO4. *J. Phys. Chem. C* **113,** 20527–20530 (2009).

107. Zhou, F., Maxisch, T. & Gerbrand, C. Configurational electronic entropy and the phase diagram of mixed-valence oxides: The case of LixFePO4. *Physical Review Letters* **97,** 155704 (2006).

108. Balluffi, R. W., Allen, S. M. & Carter, C. W. *Kinetics of Materials*. 645 pages (Wiley, 2005).

109. Abdellahi, A., Akyildiz, O., Malik, R., Thornton, K. & Gerbrand, C. Particle-size and morphology dependence of the preferred interface orientation in LiFePO4 nano-particles. *J. Mater. Chem. A* 15437–15447 (2014).

110. Sun, Y., Lu, X., Xiao, R., Li, H. & Huang, X. Kinetically Controlled Lithium-Staging in Delithiated LiFePO4 Driven by the Fe Center Mediated Inter-Layer Li-Li Interactions. *Chem Mater* **24,** 4693–4703 (2012).

111. Gabrisch, H., Wilcox, J. & Doeff, M. M. TEM Study of Fracturing in Spherical and Plate-like LiFePO4 Particles. *Electrochem Solid St* **11,** A25 (2008).

112. Laffont, L. *et al.* Study of the LiFePO4/FePO4 Two-Phase System by High-Resolution Electron Energy Loss Spectroscopy. *Chem Mater* **18,** 5520–5529 (2006).

113. Van der Ven, A., Garikipati, A., Kim, S. & Wagemaker, M. The Role of Coherency Strains on Phase Stability in LixFePO4: Needle Crystallites Minimize Coherency Strain and Overpotential. *Journal of the Electrochemical Society* **156,** 1–9 (2009).

114. Malik, R., Abdellahi, A. & Ceder, G. A Critical Review of the Li Insertion Mechanisms in LiFePO4 Electrodes. *Journal of the Electrochemical Society* **160,** A3179–A3197 (2013).

115. Orvananos, B. *et al.* Architecture Dependence on the Dynamics of Nano-LiFePO4. *Electrochimica Acta* **137,** 245–257 (2014).

116. Meethong, N., Huang, H.-Y. S., Carter, W. C. & Chiang, Y.-M. Size-Dependent Lithium Miscibility Gap in Nanoscale Li1-xFePO4. *Electrochem Solid St* **10,** A134 (2007).

117. Zhu, Y. *et al.* In Situ Atomic-Scale Imaging of Phase Boundary Migration in FePO 4Microparticles During Electrochemical Lithiation. *Adv. Mater.* **25,** 5461–5466 (2013).

118. Gu, L. *et al.* Direct Observation of Lithium Staging in Partially Delithiated LiFePO4 at Atomic Resolution. *Journal of the American Chemical Society* **133,** 4661–4663 (2011).

119. Suo, L. *et al.* Highly ordered staging structural interface between LiFePO4 and FePO4. *Phys. Chem. Chem. Phys.* **14,** 5363 (2012).

120. Zhu, C. *et al.* Size-Dependent Staging and Phase Transition in LiFePO4/FePO4. *Adv. Funct. Mater.* **24,** 312–318 (2013).

121. Sun, Y., Lu, X., Xiao, R., Li, H. & Huang, X. Kinetically Controlled Lithium-Staging in Delithiated LiFePO4 friven by the Fe Center Mediated Interlayer Li–Li Interactions. *Chem Mater* **24,** 4693–4703 (2012).